Electron Transport in Coupled Quantum Wells and Quantum Wires

(結合量子井戸および量子細線における電子伝導)

A Thesis Presented to the Graduate School
of the University of Tokyo
in Partial Fulfillment of the Requirements
for the Degree of Doctor of Philosophy
in Electronic Engineering

by

Yuzo Ohno

December 20, 1995

Dissertation Supervisor

Professor   Hiroyuki   Sakaki

Acknowledgment

This thesis presents a part of research work carried out at the Institute of Industrial Science (IIS), University of Tokyo, and Research Center for Advanced Science and Technology (RCAST), University of Tokyo, under the direction of Professor Hiroyuki Sakaki, while the author was a graduate student of the Department of Electronic Engineering, University of Tokyo, from 1991 to 1995.

First, the author would like to express his sincere gratitude to the dissertation supervisor, Prof. Hiroyuki Sakaki, RCAST, University of Tokyo, for a number of exciting discussions and his constant encouragement. Without his kind guidance, this work could not have been accomplished.

He is also deeply indebted to Prof. Masahiro Tsuchiya, the Department of Electronic Engineering, University of Tokyo, for fruitful discussions and helpful advice.

Special thanks are given to Prof. Kazuhiko Hirakawa and Prof. Gerhard Fasol, University of Tokyo, for valuable discussions. He would like to express his sincere gratitude to Prof. Shinji Kawaji and Dr. Tohru Okamoto for the usage of their high-magnetic field system, and their technical support. He wishes to thank Yusui Nakamura and Mark Foley for exciting discussions and their collaboration in part of the present work.

The author would like to express sincere gratitude to Prof. Joji Hamasaki, Prof. Yoichi Fujii, Prof. Toshiaki Ikoma, Prof. Yasuhiko Arakawa, Prof. Toshiro Hiramoto, and Lecturer Takuji Takahashi, of University of Tokyo, for their constant encouragements. He is also indebted to the staff of his group, and his colleagues; Mr. T. Noda, Dr. T. Matsusue (Chiba-University), Dr. H. Akiyama, Dr. Y. Nagamune, Dr. J. Motohisa (Hokkaido-University), Dr. H. Kurata (Fujitu Corp.), Dr. H. Sugawara (Univ. of Tokyo), Dr. H. Noguchi (Sony Corp.), Mr. R. Sasagawa, Mr. S. Tsujino, Mr. T. Someya, Mr. M. Narihiro, Mr. G. Yusa, Mr. D. Kishimoto, and Mr. T. Tsuda. Thanks are also given to the members of the Quantum Wave Project ($\sim$ 1994) and the Quantum Transition Project (1995 $\sim$), Fujii Laboratory, Arakawa Laboratory, Takahashi Laboratory, Hirakawa Laboratory, and Hiramoto Laboratory.

Last but not at least, the author would like to thank his parents for their constant encouragement.

December 1995,

Yuzo Ohno

ii

Contents

Chapter 1

Introduction

1.1 Historical Background

Semiconductor electron devices are necessary for the contemporary life. Most industrial electronic devices are silicon metal-oxide-semiconductor (MOS) devices, but semiconductor heterostructures mainly consisting of III-V compound materials have also attracted considerable attention. Since the middle of the 1970's the number of researchers in the field of compound semiconductor has increased. Esaki and Tsu proposed a one dimensional periodic potential with a scale of ~10 nm, a so called "superlattice" (SL) in 1970. [1] They predicted that in such artificially modulated semiconductor structures one can observe various quantum mechanical effects which have been well-known but not observed in bulk materials.

In order to fabricate high-quality semiconductor microstructures, much effort has been devoted to develop epitaxial growth techniques in the last quarter of a century. Molecular beam epitaxy (MBE) is one of the most reliable methods to grow smooth and thin films with an accuracy of the order of one atomic layer. [2] A pioneering group observed negative differential resistance (NDR) due to the resonant tunneling (RT) effect in a GaAs / AlGaAs double barrier (DB) structure prepared by MBE. [3] This has had a great impact on electronics engineering as well as on the experimental study of quantum mechanics. Many applications of (resonant) tunneling in DB or SL structures have been proposed and examined as high-speed devices up to $\sim$ THz [4–6], novel functional devices [7], and as a detector or a source of light in the far-infrared (FIR) region. [8]

Electronic properties of two-dimensional systems have also deserved much attention. The reduced degree of freedom for electron motion results in a modification of the density of states N_{2D}, which is effective for optical lasers. [9] In-plane transport properties of a 2DEG have been extensively studied, too. The fact that the mobility of a 2DEG is greatly improved by modulation doping techniques [10] as well as the reduction of

-1
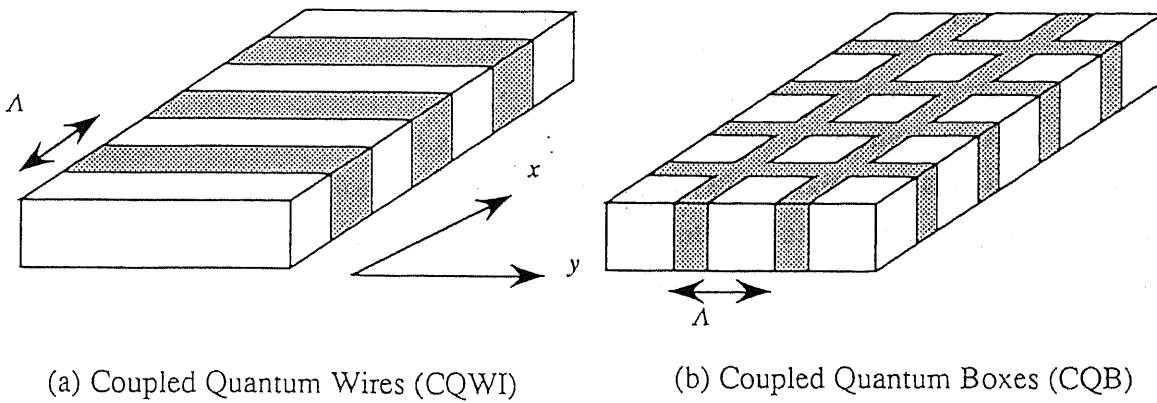
(a) Coupled Quantum Wires (CQWI)   (b) Coupled Quantum Boxes (CQB)

Figure 1.1: Examples of various forms of planar superlattices (PSL's): (a) coupled quantum wires (CQWI) and (b) coupled quantum boxes (CQB) structures.

residual impurities has made it possible to realize high-performance field effect transistors (FET's). [11] Besides, a number of fascinating phenomena such as integer and fractional quantized Hall effects (QHE) [12,13] have been observed in the high-mobility 2DEG. In particular, the latter caused lively discussions in the field of physics of many-body systems. [14]

By the way, in the 1980's, nano-processing technologies such as electron-beam (EB) lithography have been much developed to reduce the size of devices down to ~ 0.1 μm for large-scale integration of circuits. The Quantum size effect caused by lateral confinement of carriers may become a serious problem in practical applications. On the other hand, unique properties of quantum wires (QWI's) or quantum box (QB) structures, where further confinement of carriers reduces the degrees of freedom to one- (1D) or zero-dimension (0D), have been theoretically studied and demonstrated. It has been predicted that high-quality QWI or QB structures could provide high-performance devices like a remarkably high-mobility FET [15] or a laser with very low threshold current. [16] From the point of view of industry as well as physical interest, many attempts have been made to fabricate those promising device structures. Moreover, fascinating features of planar super lattice (PSL) structures, which consist of QWI or QB arrays as shown in Fig. 1.1, have also been examined theoretically. [17,18]

Although some characteristic features of lateral confinement have been observed experimentally [19], it is hard to expect that actual devices exhibit the high-performance which is promised in ideal QWI's or QB's at present. This is mainly because they make

rigorous demands on nano-fabrication techniques, such as small fluctuations in the size
and the uniformity, and damage-free processing.

From another point of view, such semiconductor nano-structures have become the
center of attention. Since the capacitance becomes smaller with the size of the devices,
the energy for charging one electron becomes larger than other energies such as thermal or
excitation energies, resulting in a Coulomb blockade. [20] This effect opens a possibility
to realize switching devices [21] or memory cells [22] working with a single electron,
ultimately small devices for future integrated circuits. In each case, further efforts must
be made to improve processing techniques for the fabrication of ultra-fine devices and
structures.

1.2 Electronic Properties of Double Quantum Well Structures

In a coupled quantum well (CQW) structure or SL's, various phenomena of interest are
expected to appear since the motion of carriers in the direction perpendicular to the layers
can be systematically modulated by changing such parameters as width or height of the
barriers, [23] and also can be controlled by an external electric field. [24] Recently, double
quantum wells (DQW's), which are the simplest of CQW structures, have attracted much
attention from many points of view. Recent developments of epitaxial growth, especially
of high-quality inverted heterointerfaces, allow us to study electronic properties in DQW's
which arise from the fact that an extra degree of freedom is added to those of a single
2DEG. In this section, I make a review of the studies on electronic properties in a DQW.

1.2.1 Resonant Coupling and Coherent Tunneling in Double Quantum Wells

In a DQW structure, carriers in one QW interact in many ways with those in the other
QW. Resonant coupling is one of those interwell interactions in DQW's, which can be
controlled by an external electric field as shown in Fig. 1.2, while the coupling strength
is primarily determined by the barrier thickness or height. Wave functions are drastically
changed from isolated states to symmetric and antisymmetric states when these two
quantized states reach resonance. These facts have been disclosed particularly in optical
experiments such as anti-crossing of energy levels with an external field in absorption
spectra or as quantum-beat in the dynamic response to an ultra-short excitation pulse. [25]
Thus the unique properties which come from coherent tunneling in DQW's are highly
attractive for optical applications such as modulators or tunable lasers [26].

(a) single QW   (b) double quantum well (resonance)

(c) double quantum well (off-resonance)
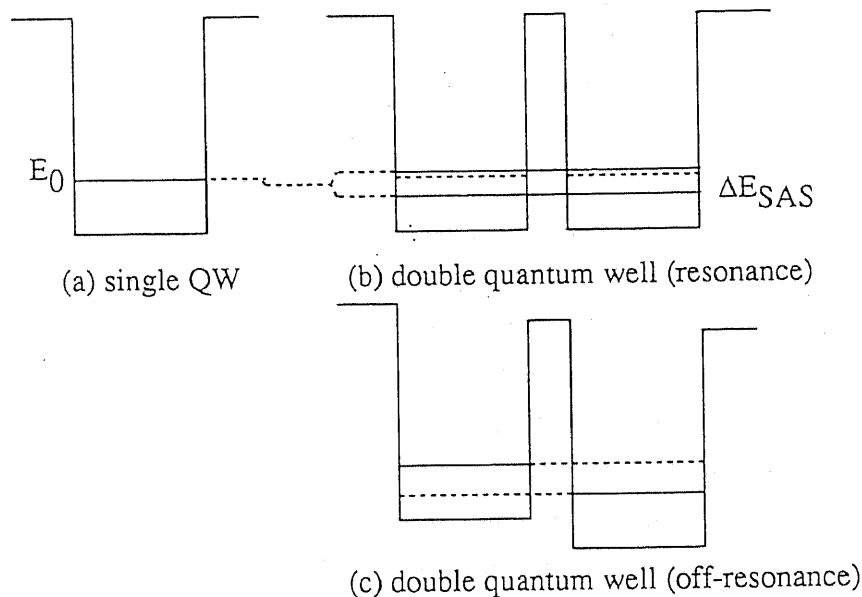
Figure 1.2: (a) An isolated quantum well (QW) potential and the quantized energy E_0. (b) The potential profile of coupled QW's (double quantum well: DQW) at resonance, and (c) that of off-resonance. At resonance, the degeneracy of the energy level E_0 of isolated QWs is lifted with a tunnel gap ΔE_{SAS}.

Coherent tunneling in DQW's can give rise to a modulation of electron transport properties parallel to the layers as well. Since a QW layer is a "slab" waveguide for electrons, DQW structures can be prototypes for coupled electron waveguides consisting of quantum well wires. [27–30] These electron waveguides may be one of the key features in potential future "quantum wave electronics". One should note, however, that the loss of coherence of electron waves due to dissipation is fatal for such devices. In order to make quantum interference effective, the mean free path l_e or phase coherence length L_ϕ, which are ~ 1 μm for high mobility samples, must be long enough.

1.2.2 Mobility Modulation by Wavefunction-Dependent Scattering

Another approach has been proposed and experimentally examined to control the transport properties in a DQW with the resonant deformation of wavefunctions. In 1982, Sakaki proposed a velocity modulation transistor (VMT), in which the channel conductivity is modulated by controlling the mobility rather than the density of carriers in the channel as in a conventional FET. [31] If the mobility can be controlled without changing the number of carriers, this principle saves the carrier transit time which arises inevitably from the gate-source capacitance and hence limits the speed of operation. The "mobility

modulation" by the deformation of wavefunctions in front- and back-side gate configurations [31] has been experimentally examined in a normal modulation-doped single heterostructure [32] and in a partly-doped wide QW. [33]. However, the observed effects were too small to control the channel conductivity: The features appear only in the analyzed data of Hall measurements.

An idea to improve the mobility modulation effect was proposed by Vinter and Tardella. They employed resonant tunneling in a double channel FET structure where ionized impurities are used as dopant in one of several coupled channels. They demonstrated theoretically the possibility of negative transconductance. [34] This concept has been examined by Palevski et al. using a DQW structure which has two closely-separated QW's with very different mobilities. [35] They observed a resistance peak at resonance, referred to as "resistance resonance", due to the enhancement of scattering only for the wavefunctions extended over both QW's. In this method, as shown in Fig. 1.3, a gigantic negative transconductance has been realized. [36, 37]

The modulation of the transport properties in DQW's with other wavefunction-dependent scattering mechanisms such as the interface roughness scattering [38] or neutral impurity scattering [39] has been also investigated. These unique characteristics should be useful to inspect the physics of resonant coupling by in-plane transport measurements as well as by vertical transport measurements.

1.2.3 Resonant Tunneling in Weakly-Coupled Double Quantum Wells

Coherent tunneling and consequent modulations of parallel in-plane transport characteristics are achieved in DQW's of relatively strong coupling. In weakly-coupled DQW's, on the other hand, the effect of transverse tunnel-coupling should be too small to be observable in parallel transport experiments. If the energy gap ΔE_{SAS} of symmetric and antisymmetric states is smaller than the collision broadening of the energy level in either QW, namely, electrons suffer at least one scattering event during one tunnel process, it is unacceptable to describe the electronic states by wavefunctions which are the solutions of the time-independent Schrödinger equation. In particular, introduction of an additional scattering mechanism which is essential for the scheme of mobility modulation should prevent the tunnel-coupling. This restricts the range of possible experiments.

These limitations are forced by the technical difficulty to form independent ohmic contacts to one of two closely separated 2DEG's. Thus most of the transport experiments in DQW's have been done in parallel mode. Recently, some attempts have been made to realize independent ohmic contacts in elaborate ways in order to measure the tunnel

(a)

(b)
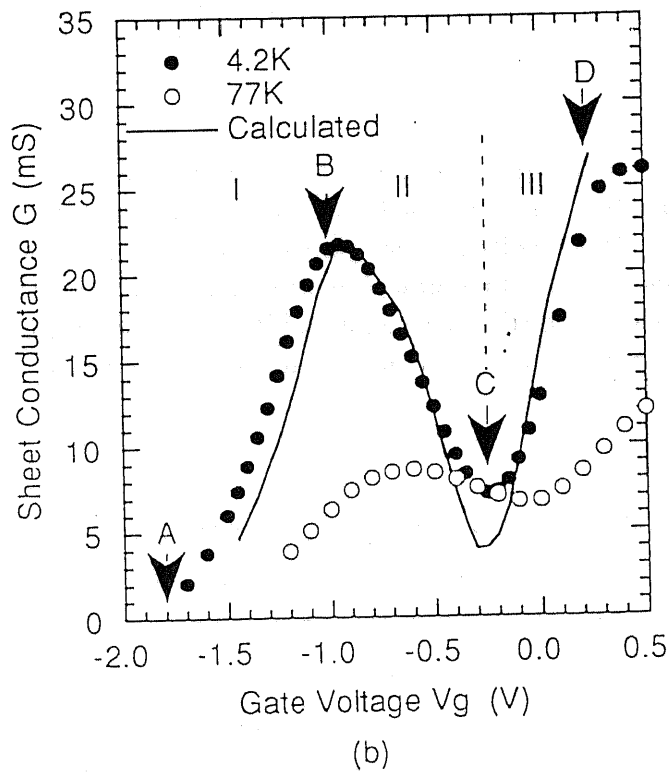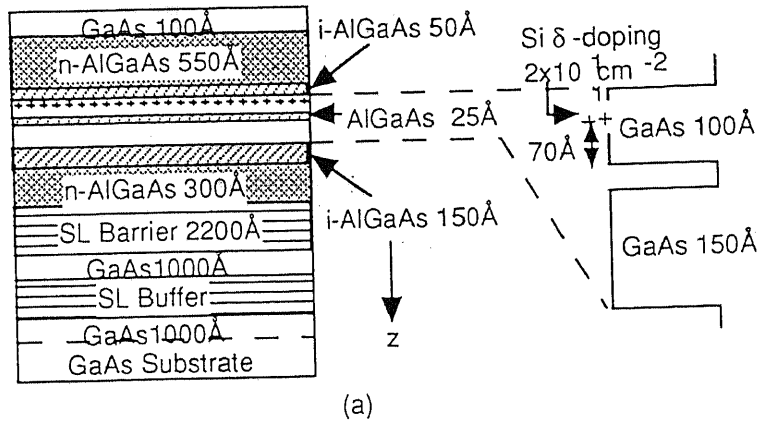
Figure 1.3: (a) The cross-sectional view of an impurity-doped double quantum well (ID-DQW) field effect transistor (FET), and (b) its channel conductance vs. gate voltage characteristics at 4.2 K. After [37].
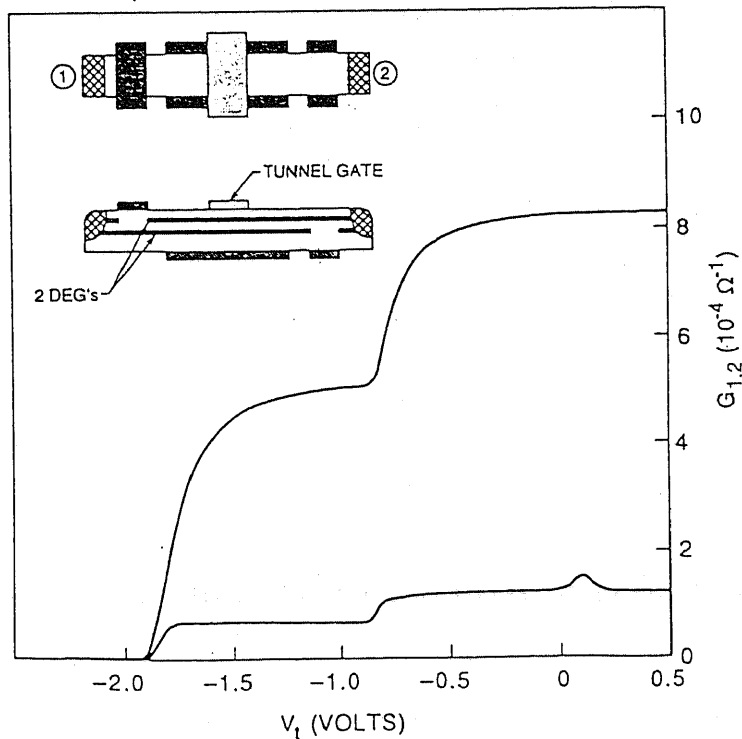
Figure 1.4: A schematic view of the mesa layout (upper inset) and a cross section in "tunnel" configuration (lower) are shown. The upper line indicates the conductance $G_{1,2}$ between two contacts in "parallel" configuration, where both contacts are connected to two 2DEGs. With a negative bias voltage V_t applied to the tunnel gate, the top QW reach depletion first, and the bottom QW in sequence, resulting in the step structure. The lower trace in "tunnel" configuration exhibits a peak at $V_t \doteq 0.1V$ due to the resonant tunneling. After [43]

conductance between two 2DEGs in close proximity, [40] as well as to study their transport properties individually. [41] Eisenstein et al. started a study of 2D-2D tunneling in a novel DQW field effect structure in which an ohmic contact primarily connected to both QWs can be switched between either of them by a selective depletion technique. [42] A typical result of this scheme is shown in Fig. 1.4. [43] The upper inset in Fig. 1.4 shows a schematic view of the mesa layout, and the lower depicts the simplified cross section in "tunnel" configuration, where the ohmic contact 1 is electrically cut off from the top 2DEG by applying negative bias voltage to a front gate, while the ohmic contact 2 is isolated from the bottom 2DEG by a back gate in a similar manner. The zero-biased conductance $G'_{1,2}$ between these two electrodes was measured as a function of tunnel gate voltage V_t in "tunnel" configuration (a lower line), exhibiting a prominent peak at $V_t = 0.1$ V. In this case, conservation of in-plane momentum allows the tunneling only when the two levels are closely aligned, resulting in a distinct and sharp tunnel conductance peak.

This method has opened a new class of experiments in DQW's. First, it allows us to investigate the mutual interactions between symmetric and very high mobility 2DEGs since introduction of an additional scattering mechanism is not necessary. In addition, the electronic properties in the vicinity of the Fermi energy can be extracted from the data, for the electrons on the Fermi surfaces can participate in a tunnel event. [44] Secondly, one can make magnetotunneling experiments in this scheme. [45–49] Most of them have been done by studying the vertical tunnel current in such semiconductor heterostructures as DB-RTD. [50] In "parallel" configuration, on the other hand, the resonance features originated from the mobility modulation will disappear, since the wavefunction-dependent scattering mechanism may not function any longer when a high magnetic field is applied and quantizes the in-plane kinetic energy of electrons.

1.2.4 Resonant Tunneling and Coulomb Interaction in Strong Magnetic Fields

When a strong magnetic field B is applied perpendicular to a single 2DEG sheet, the Hall resistance is quantized and the magnetoresistance tends to vanish when the filling factor $\nu = nh/eB$ is an integer number or an odd-denominator fraction, where n is the electron density, h the Plank constant, and e the elementary charge. [14] The former (integer quantum Hall effect: IQHE) is associated with the Landau-quantization of the energy spectrum, which can be explained by a single particle model. For the latter (fractional quantum Hall effect: FQHE), on the other hand, the mutual Coulomb interaction is essential to give rise to an energy gap at the Fermi energy due to the formation of stable many-body ground states. [14]

In DQW structures, in which such interesting properties of high mobility 2DEG's are preserved, one can expect further new finding of IQHE or FQHE states not present in single-layer systems because of the addition of extra degrees of freedom, namely, direct tunneling of a particle and inter-layer Coulomb interaction. [51–56] Indeed, new FQHE states were observed at even-denominator filling factor $\nu = 1/2$ in double-layer 2DEG systems. [57, 58] Conditions for Wigner crystallization are also believed to be more faborable in double lyers systems. [59]

It has also been found that the energy gap ΔE_{SAS} resulting from a single-particle tunneling between two QW's is destroyed by intra-layer Coulomb correlation, leading to missing the IQHE states at small odd-integer filling factors. [60–63] In Fig. 1.5(a), an energy diagram for a DQW at resonance is shown schematically. When a magnetic field B is applied perpendicular to the layers, the symmetric and antisymmetric states each form a pair of spin-split Landau levels separated by the Zeeman energy $g^*\mu_B B$, where μ_B

is the Bohr factor. As long as tunneling of electrons can take place, the system can be treated as a single QW, and IQHE should be observed at both even and odd integer filling factors ν. Note that $\nu = n_{tot}h/eB$, where n_{tot} is the total electron density in the DQW. When the Fermi energy lies between the spin-polarized symmetric- and antisymmetric states, the excitation costs an energy ΔE_{SAS}, which will be compensated by the gain in electron correlation energy. This becomes much more important in sufficiently strong magnetic fields, resulting in the collapse of ΔE_{SAS} at $\nu =$ odd integers. [60] Figure 1.5(b) summarizes such phase transition of quantized states in DQW's. [64]

Recently, Eisenstein et al. measured directly the tunnel current between two 2DEG's in DQW structures with a strong magnetic field applied normal to the 2D planes by using the selective depletion technique. [46, 47] They found the zero-field resonant tunneling to be suppressed for a wide range of B which satisfies $\nu < 1$, as well as in the IQHE regime where the path of in-plane current flow is restricted to the boundary region at the mesa. For the former, they attribute the tunnel anomalies to the intra-layer Coulomb correlation of a 2DEG throughout the lowest Landau level. [46] However, some complications exist with this interpretation. [49, 65]

These experimental studies on magnetotransport in multi-layered 2DEG systems have revealed unique properties related to many-body effects, and still further interest has been directed to these systems, because fascinating phenomena are predicted by theoretical investigations. [66]

1.3   Electron Transport in One Dimension and Fabrication of Quantum Wires

Recently, an interest on effects, such as the resonant tunneling and / or the mutual Coulomb interaction has been extended to the case of one-dimensional (1D) systems. [18, 67] Here, we make a brief review of the results of recent studies on electron transport in quantum wires (QWI's).

The description for the transport properties in 1D systems will change drastically with the size (length and width) of the channel, the mean free path (coherence length) of electrons, or the degree of disorder. One representative of the unusual features of 1D systems is the quantization of the conductance. When the channel length L is sufficiently shorter than the mean free path l_e, electrons can propagate through the 1D channel without suffering any scattering event. In this case, however, the conductance does not become infinite, but converges to a finite value, i.e. the quantized conductance G [68] can
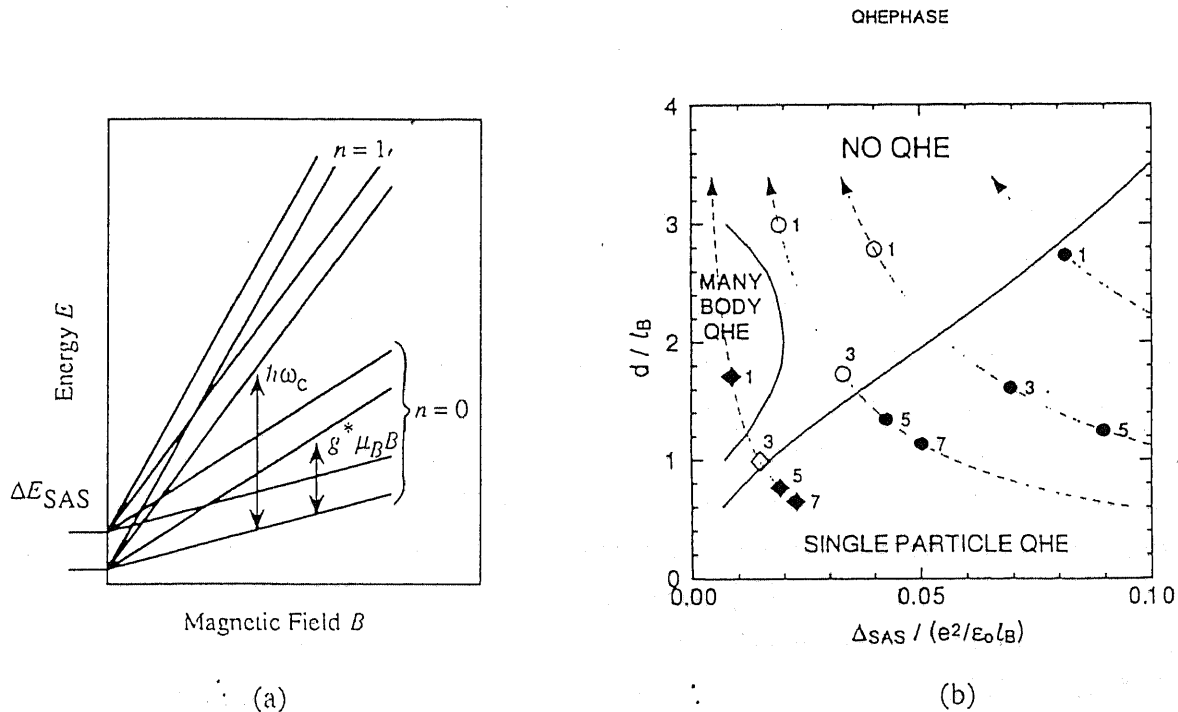
Figure 1.5: (a) Energy diagram for a double quantum well. The cyclotron ($\hbar\omega_c$), Zeeman ($g^*\mu_B B$), and symmetric-antisymmetric (ΔE_{SAS}) energies are indicated. (b) Schematic phase diagram of the quantized states at $\nu =$ odd in a double quantum well. The dashed arrows represent increasing magnetic field for a given sample fixed the layer separation d, ΔE_{SAS}, and n. d and ΔE_{SAS} are scaled by the magnetic length $l_B = (\hbar/eB)^{1/2}$ and characteristic Coulomb energy $e^2/\epsilon l_B$, respectively. Filled / open symbols denote observed / missing quantum Hall states labeled by filling factor ν. The solid lines are schematic boundaries representing the Coulomb-driven destruction of the single particle tunneling QHE, and re-emergence of a many-body QHE in the regime of $d/l_B \sim 1$ and $\Delta E_{SAS} = 0$. Taken from Ref. [64].

be expressed as

$$G = \sum_{n=1}^{N_C} \frac{e^2}{\pi \hbar},\tag{1.1}$$

where $N_C \sim k_F W/\pi$ is the number of 1D-subbands in the channel, W the width of the channel, and k_F the (2D-) Fermi wave number. This situation has been achieved in quantum point contacts (QPC's) [69, 70], in which the width of a high-mobility 2DEG channel was reduced to ~ 100 nm by the depletion beneath two Schottky gates defined on the top of the 2DEG.

This quantization of the conductance should collapse when the QWI's become long. In actual QWI's, it is technically impossible to remove the residual impurities and to control the size of QWI's perfectly. Therefore, electrons will be scattered by ionized impurity or interface roughness potential. In addition, it has been emphasized in theoretical studies that in 1D systems the electron-electron interaction can play a crucial role. [71] Taking the mutual Coulomb interaction into account, the resistivity of a "dirty" QWI is predicted to diverge in the limit of low temperatures even when the scattering matrix element is finite. [72–74] The results of these theoretical studies present a contradiction with other predictions that in quantum wire (QWI) structures in which electrons occupy only the lowest subband, the scattering due the ionized impurities is suppressed and extremely high mobility exceeding 10^8 cm^2/Vs could be achieved. [15]

To reveal the unique and complicated features of a 1D electron system, experimental studies are highly desirable. For these purposes, however, one must fabricate a QWI sample which satisfies severe requirements in the scale and the uniformity of the size of the lateral-confinement potential. So far, QWI or QB structures have been fabricated mostly by narrowing the width of a high-mobility 2DEG in modulation-doped heterostructures with Schottky gates formed by nano-processes. [75] In the latest experiments, quantized conductance has been observed in remarkably long (2~10 μm) QWI samples fabricated by a refined method. [76] An alternative approach to fabricate QWI structures in a scale of ~ 10 nm has been also progressed by utilizing advanced crystal growth techniques such as *in-situ* processes [15, 77] or selective growth on patterned substrates. [78, 79]

1.4   Aim of This Thesis

In the beginning of the 1990's, when I started research in this field, fundamental technologies for the fabrication of semiconductor microstructures had been highly advanced: one can obtain a 2DEG of very high mobility exceeding 10 000 000 cm^2/Vs at low temperatures, and draw a fine pattern on a wafer with resolution of 0.01 μm. Although a number of articles have been devoted to studies of electron transport in low-dimensional

systems, less attention was directed to coupled systems. We considered that only part of the unique properties of coupled quantum wells (CQW's) or coupled quantum wires (CQWI's) had been investigated previously, and that they should deserve more attention from the point of view of electronic engineering because of their potential for applications for high-performance and novel functional devices. We also found that no reliable method has been established to fabricate high-quality CQWI structures in which inter-QWI interaction can be systematically controlled as in a CQW structure, while high-quality CQW is available by standard MBE.

The aims of the present thesis are as follows:

- To design and fabricate novel electron devices in which such quantum mechanical effects such as resonant tunneling are utilized to realize unique functions.

- To investigate the effects of the gate-controlled resonant coupling of electron wavefunctions on the in-plane transport characteristics in novel double quantum well (DQW) structures under various situations.

- To develop growth methods for the fabrication of high-quality QWI structures for the future study of electronic properties in coupled QWI structures.

In Chapter 2, we describe the principle of mobility modulation in DQW's in which ionized impurities are intentionally doped in one of two QW's. The actual shapes of the electron wavefunctions have been experimentally investigated by studying the magnetoresistance.

In Chapter 3, the resonant coupling of electron wavefunctions in DQW's is studied in the presence of in-plane magnetic field. A simple theory is presented to explain the observed anisotropic dependence of the in-plane magnetoresistance on the mutual directions between the current and the magnetic field.

In Chapter 4, resonant tunneling between two 2DEG's in high-mobility DQW's is studied in the quantum Hall regime. Clear features of the suppression of the resonant tunneling at IQHE are shown.

In Chapter 5, we present a novel scheme to modulate the effective mass of electrons by the gate voltage. Controllability of electronic states in a DQW, which consists of a QW and a PSL separated by a thin barrier, is theoretically analyzed.

In Chapter 6, we describe the *in-situ* cleavage and overgrowth method to fabricate narrow edge quantum wire structures. The magnetoresistance oscillations, which were observed in 50 nm-wide QWI's, indicate not only the presence of the lateral confinement but also unique features of 1D electron systems.

Chapter 2

Resonant Coupling in Impurity Doped Double Quantum Wells

2.1 Introduction

As described in Section 1.2.2, the resonant coupling influences parallel in-plane transport characteristics in a double quantum well (DQW) with a wavefunction-dependent scattering mechanism. In particular, "resistance resonance" observed in a DQW of asymmetric scattering allows us to investigate the resonant coupling by a simple resistance measurement. [35] Moreover, it has been experimentally demonstrated that quite a large modulation of the channel resistance can be realized by appropriate choice of the parameters such as the coupling strength and the impurity densities. [36,37] In this chapter, we study the resonant coupling in asymmetrically impurity-doped DQW's (ID-DQW's) further in detail.

In the next section, we describe the principle of mobility modulation by gate-controlled resonant coupling. A set of results of self-consistent calculations and numerically computed mobilities are presented to illustrate the mobility modulation effect more quantitatively.

In the third section, we investigate the resonant modification of wavefunctions and transport properties in ID-DQW's by magnetoresistance measurements. Although this phenomenon is based on a simple quantum mechanical effect, "resistance resonance" reveals only the fact that the scattering is enhanced at a resonant condition. It does not provide any information on whether or not symmetric and antisymmetric wavefunctions are actually formed as seen in a text book of quantum mechanics. This is because the random potential due to ionized impurities or fluctuations of the layer thickness is likely to cause the breakdown of such a simple picture of quantum mechanical effects.

In order to clarify these questions, we carried out magnetic-field dependent Hall mea-

Figure 2.1: A model of a modulation-doped double quantum well (DQW) with a Si^+ δ-doping layer buried at the center of the top QW.

surements to inspect the resonance features. In particular, magnetoresistance of ID-DQW's is systematically studied to estimate the difference in mobilities between two subbands at various gate voltage. The resonance features predicted by the theoretical analysis are tested with respect to the degree of disorder.

2.2 Mobility Modulation by Gate-Controlled Resonant Coupling

As an approximate expression for wavefunctions and the tunnel coupling energy in DQW's, linear combinations of eigenfunctions in two isolated QW's are widely employed. [80] This is, however, insufficient to describe the electronic states in tightly coupled systems and, in particular, in modulation-doped structures. The electrostatic potential due to the space charges needs to be included and a self-consistent calculation is required to obtain more realistic wavefunctions. In this section, we describe briefly the procedure of our self-consistent calculation, the details of which can be found in Ref. [81].

2.2.1 Self-Consistent Calculation of Wavefunctions

A model of a modulation-doped GaAs / AlGaAs ID-DQW structure is schematically shown in Fig. 2.1.

The DQW consists of two 15 nm-wide GaAs QW's separated by a 2 nm-thick AlGaAs barrier. Electrons are partly supplied by the remote impurities in the AlGaAs. At the center of the top QW (near the gate electrode), a Si^+ δ-doping layer of 3×10^{11} cm^{-2} is inserted to degrade the intrinsic mobility of electrons.

We solved the Schrödinger equation

$$\{-\frac{\hbar^2}{2m^*}\frac{\partial^2}{\partial z^2} + V(z)\}\psi_i(z)\exp(ikr) = E_i\psi_i(z)\exp(ikr) \qquad (2.1)$$

and Poisson's equation

$$\epsilon\kappa\frac{d^2\phi(z)}{dz^2} = eN_D(z) - eN_A(z) - e\frac{m^*}{\pi\hbar^2}\sum_{i=1}^{n}|\psi_i(z)|^2(E_F - E_i) \qquad (2.2)$$

self-consistently, where $\hbar$ is the reduced Plank constant, e the elementary charge, E_F the Fermi energy, $\phi(z)$ the electrostatic potential, and $\psi_i(z)$ the normalized wavefunctions of the i-th subband. For simplicity, both the effective mass m^* of electrons and the dielectric constant $\kappa\epsilon$ are assumed to be constant both in GaAs and AlGaAs. $N_D(z)$ and $N_A(z)$ are the donor and the residual acceptor densities, respectively. The temperature T was set to be zero K since we consider only the transport properties in a low-temperature range where ionized impurity scattering dominates the electron mobility. All the δ-doped Si^+ donors are assumed to be ionized and counted in $N_D(z)$, even when E_F is higher than the donor levels in GaAs. The exchange-correlation potential energy $V_{ex}(z)$ was taken into account [81], but we ignored further exchange effect associated with the charge transfer from one QW to the other. [82,83]

The calculated electron densities n_{si} of the occupied ith subbands are plotted in Fig. 2.2 as functions of the gate voltage V_g. They correspond to the energy levels with respect to the Fermi energy E_F since $n_{si} = N_{2D}(E_F - E_i)$, where $N_{2D} = m^*/\pi\hbar^2$ is the two-dimensional density of states. As V_g increases from the threshold voltage, electrons populate the lower subband E_1 first. As V_g reaches -0.9 V, electrons start to populate the upper subband E_2 in sequence. Further increase of V_g induces electrons mainly in the upper subband, while n_{s1} remains almost constant. As shown in Fig. 2.2, the two levels reach resonance with the energy separation $\Delta E_{SAS} = 1.3$ meV at $V_g = -0.25$ V.

2.2.2   Wavefunction-Dependent Electron Mobilities

Using the wavefunctions and electron densities obtained from self-consistent calculations, we calculated the mobility of each subband dominated by ionized impurity scattering. [84] Within the Born approximation, a 2×2 scattering matrix was computed by numerical
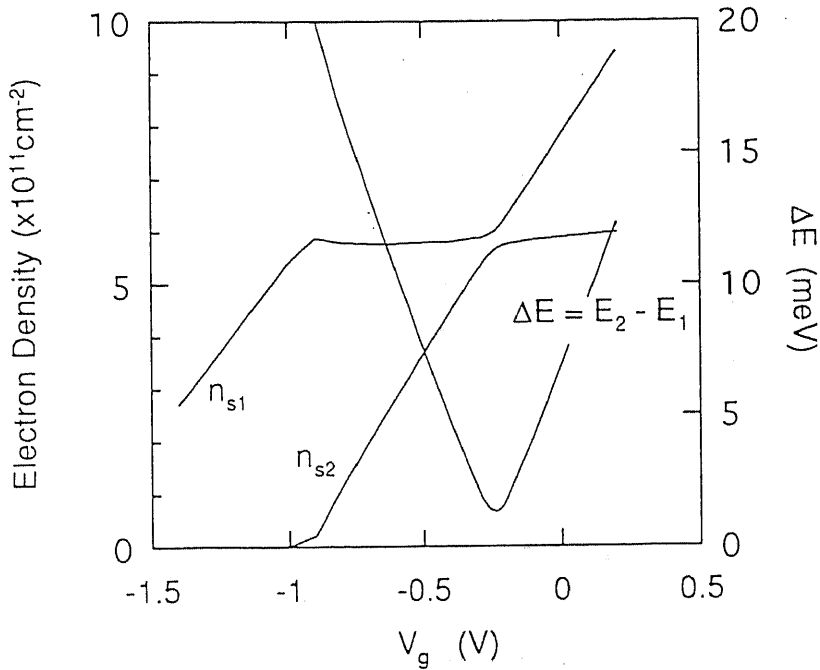
Figure 2.2: Calculated electron densities n_{si}, and the energy difference $\Delta E = E_2 - E_1$ are plotted as functions of the gate voltage V_g.

integration of spatial overlap between the wavefunctions $\psi_i(z)$ and the impurity distribution $e\{N_A(z) + N_D(z)\}$. Screening effects were taken into account for both intra- and inter-subband processes in random-phase-approximation (RPA). [85]

In Fig. 2.3, the computed mobilities μ_1, μ_2 are plotted by solid and dotted lines, respectively, as functions of V_g. Note that μ_1 reaches its maximum $250,000$ cm^2/Vs at $V_g = -0.8$ V, at which the higher subband is slightly occupied by electrons. This is probably because the induced electrons in the top QW screen the δ-doped impurity potential. μ_2 also increases with V_g, but reaches at most $10,000$ cm^{-2}. When V_g increases further, then μ_1 decreases due to the enhanced scattering with the impurities in the top QW. At resonance, μ_1 is reduced to $10,000$ cm^2/Vs, and gets equal to μ_2. When $V_g > -0.25$ V, the wavefunction of upper level E_2 primarily confined in the top QW moves into the bottom QW, resulting in rapid recovery of μ_2.
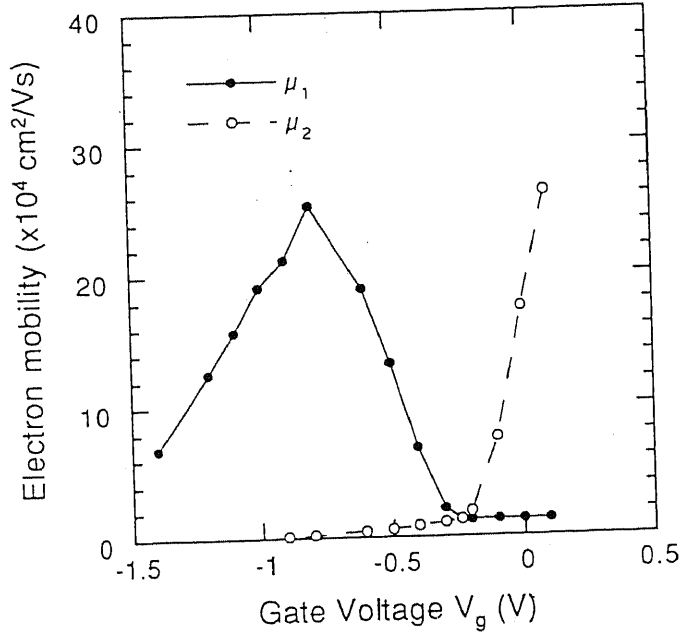
Figure 2.3: Calculated mobilities for the lower level E_1 (solid line) and the upper level E_2 (dotted line) are plotted as functions of gate voltage V_g.

2.2.3 Mobility Modulation via Gate-Controlled Resonant Coupling

Using the calculated electron density n_{si} and the mobility μ_i, the sheet channel conductivity σ can be expressed as

$$\sigma = \sum_{i=1}^{2} e n_{si} \mu_i \tag{2.3}$$

In Fig. 2.4, we plot σ as functions of V_g to illustrate the principle of the mobility modulation operation with figures of the electron wavefunctions and the potential profile.

When V_g is increased only slightly from the threshold voltage, electrons occupy only the ground state E_1. As shown in Fig. 2.4(a), the wavefunction $\psi_1(z)$ is well confined in the undoped bottom QW. As a result, σ increases with V_g, leading to a usual FET operation. When V_g is further increased to bring the energy E_2 of the excited state below E_F, σ start decreasing with V_g. As shown in Fig. 2.4(b), σ is reduced to about a tenth of that of maximum at resonance. Thus a negative transconductance operation is achieved. As V_g increases further, the resonant condition is broken. Both wavefunctions start to localize in each QW, resulting in recovery of σ. In Fig. 2.4(c), the transconductance $\partial\sigma/\partial V_g$ in "mobility modulation" mode is found to be slightly higher than that in "FET"
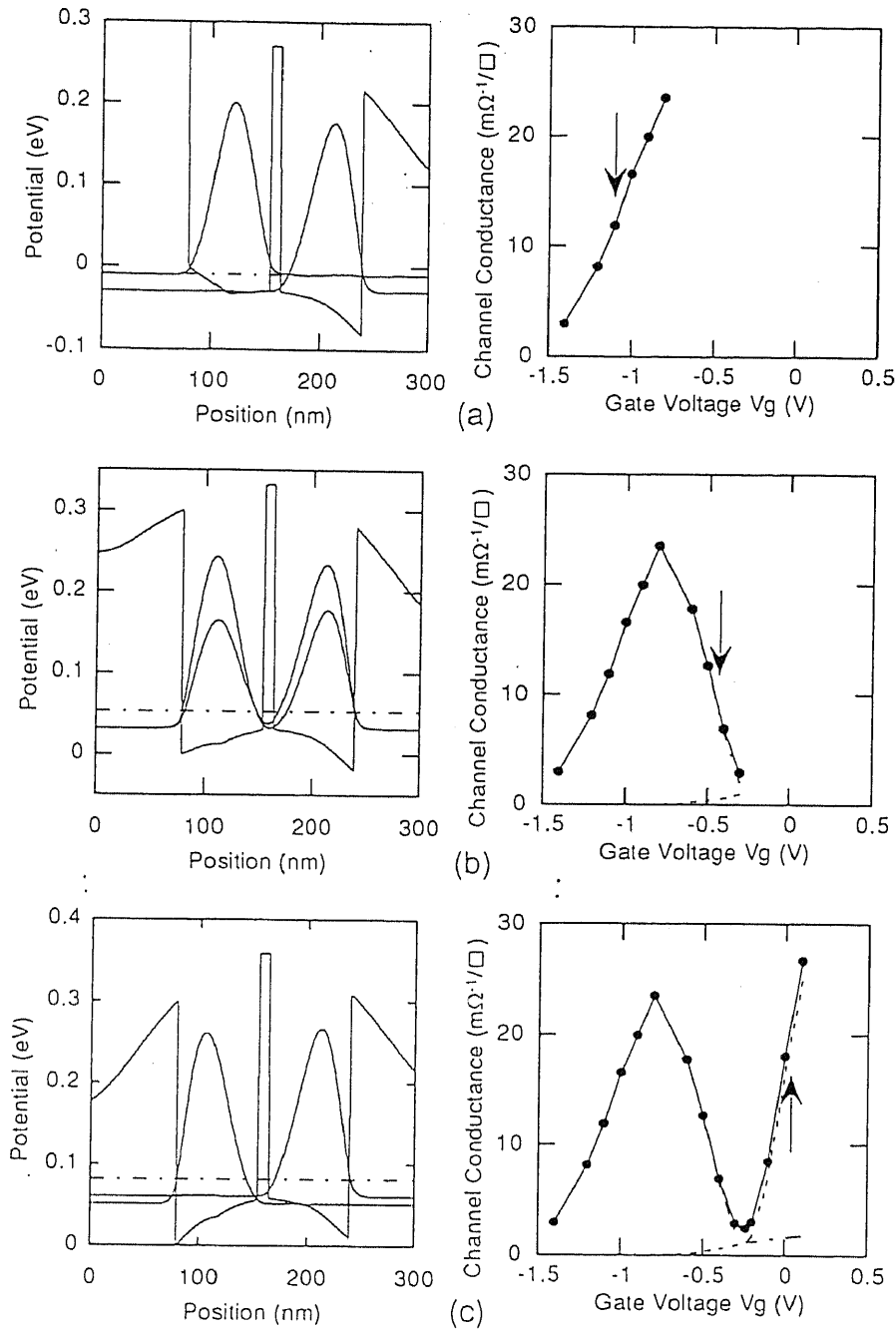
Figure 2.4: (left) Calculated wavefunctions and potential, and (right) the channel conductivity are shown at three points of the gate voltage. Each corresponds to (a) a FET mode, (b) a negative transconductance mode, and (c) a mobility-modulation mode, respectively.

mode.

2.3 Examination of Resonant Coupling by Magnetoresistance Measurement

2.3.1 Theory of Magnetoresistance in Multi-Subband Systems

As shown in the previous section, electron mobilities should change with the shape of the wavefunctions, which are controlled by the gate voltage. In particular, the mobilities of delocalized states should get equal to each other at resonance. Therefore, one can probe the actual form of wavefunctions if the mobility of each subband is known experimentally. However, when there exist two or more channels electrically connected in parallel, they can not be determined simply by a conventional Hall measurement. Here, we consider the magnetotransport properties in a multiple-subband system.

When a weak magnetic field B is applied perpendicular to the 2DEG layers, the conductivity tensor σ is expressed as

$$\sigma_{xx}(B) = \sum \sigma_{xxi} = \sum \frac{e\mu_i n_i}{1 + (\mu_i B)^2} \tag{2.4}$$

$$\sigma_{xy}(B) = \sum \sigma_{xyi} = \sum \frac{e\mu_i^2 B n_i}{1 + (\mu_i B)^2} \tag{2.5}$$

where e is the electron charge, μ_i and n_{si} are the mobility and the density of electrons for the ith subband, respectively. When the channel is isotropic, $\sigma_{yy}(B) = \sigma_{xx}(B)$, and $\sigma_{xy}(B) = \sigma_{xy}(B)$.

The resistivity $\rho_{xx}(B)$ can be derived from Eq.(2.5) as

$$\rho_{xx}(B) = \frac{\sigma_{xx}(B)}{\sigma_{xx}(B)^2 + \sigma_{xy}(B)^2} \tag{2.6}$$

It is thus possible to deduce n_{si} and μ_i of each subband from the $\rho_{xx}(B)$ and $\rho_{xy}(B)$ by Eqs.(2.5) and (2.6) [86].

In a two-subband system ($i = 1, 2$), the magnetic field dependence of ρ_{xx} directly reflects the difference of mobilities μ_1 and μ_2. When $\mu_1 B \gg 1$ and $\mu_2 B \ll 1$, $\rho_{xx}(B)$ can be approximated as [87]

$$\rho_{xx}(B) = \frac{1}{e}(n_2\mu_2 + \frac{n_1^2}{n_2\mu_2 B^2})^{-1} \tag{2.7}$$

or, the magnetoresistance $\Delta\rho_{xx}(B) \equiv \rho_{xx}(B) - \rho_{xx}(0)$ is expressed as [88]

$$\frac{\Delta\rho_{xx}(B)}{\rho_{xx}(0)} = \frac{(\mu_1 - \mu_2)^2 \sigma_1 \sigma_2 B^2}{(\sigma_1 + \sigma_2)^2 + (\mu_2\sigma_1 + \mu_1\sigma_2)^2 B^2} \tag{2.8}$$

Figure 2.5: Schematic cross sections of the sample structures.

Following Eq.(2.8), one can readily see that $\Delta\rho_{xx}(B)$ vanishes when $\mu_1 = \mu_2$, while $\Delta\rho_{xx}(B) \propto B^2$ when $\mu_1 \neq \mu_2$. One should note that this formalism is based on a semi-classical model, and valid as long as B is small enough to prevent the oscillation of $\rho_{xx}(B)$. Note also that it can not be applied to a heavily disordered system where localization of in-plane electron motion occurs due to interference effects, resulting in negative magnetoresistance. [89]

2.3.2 Magnetoresistance Measurement of Impurity-Doped Double Quantum Wells

2.3.2.A Sample Preparation and Experimental Setup

Three DQW's with asymmetric donor-impurity distribution were grown by molecular beam epitaxy (MBE). Schematic cross-sections of three samples are shown in Fig. 2.5. Except for the Si$^+$ doping profile, structural parameters such as the well width L_W or the barrier thickness L_B are identical for three samples 2A, 2B, and 2C. The DQW consists of two 15 nm-wide GaAs QW's and a 2.25 nm-thick Al$_{0.26}$Ga$_{0.74}$As barrier embedded between two QW's. Lower n-AlGaAs layer is placed 20 nm away from the backside of the DQW. Sample 2A has no undoped AlGaAs between the cap n-AlGaAs and the upper QW. In samples 2B and 2C, a Si$^+$ δ-doping layer is inserted at the center of the top QW while they have a 5 nm-thick undoped AlGaAs between the upper QW and the cap n-AlGaAs layer. The densities of Si$^+$ donors are 1×10^{10} cm^{-2} for sample 2B and 2×10^{11}

cm^{-2} for sample 2C, respectively.

The MBE growth was carried out at lower temperatures ($\sim$ 530 °C), at which migration of Si$^+$ donors in the lower n-AlGaAs layer toward the DQW channel is effectively suppressed so that high mobility in the bottom QW is achieved. [90] The growth rate was set to be slow (0.4 μm for GaAs) in order to recover the quality of the grown structures on a thick AlGaAs buffer layer.

The procedure of processing is as follows: First, a Hall bar geometry with five terminals was defined by usual photolithography. The channel with is 50 μm, and spacing between voltage probes is 200 μm. A mesa structure was then formed by chemical-etching using H$_3$PO$_4$:H$_2$O$_2$:H$_2$O $= 1 : 1 : 8$ solution for 1 minute at room temperature. The depth of the mesa is $\sim$ 1 μm. The Aluminum Schottky gate electrode covering the whole part of the channel was also defined by photolithography, and formed by evaporation of Aluminum (130 nm) in vacuum and the lift-off method. Ohmic contacts were formed by soldering InSn, and alloying at 400 °C in Ar atmosphere. The sample was set in a liquid He^4 cryostat with a 8.5 T superconducting magnet and cooled down to 1.5K by pumping. A magnetic field is applied perpendicular to the DQW channel.

2.3.2.B   Results of Magnetic-Field Dependent Hall Measurements

The channel resistivity ρ_{xx} and the Hall resistance ρ_{xy} were measured at 1.5 K by a standard ac lock-in technique at 15 Hz. A 10 nA drain-source current was fed by a signal generator with a 10 MΩ resistor connected in series. We measured channel resistivity $\rho_{xx}(0)$ at zero magnetic field as functions of gate voltage V_g, and both ρ_{xx} and ρ_{xy} at a fixed V_g as functions of B from zero to 8.5 T.

It should be noted that ρ_{xx} starts to oscillate with B when B is higher than 1 T due to Landau quantization of the in-plane kinetic energy of electrons. Here, we discuss mainly low field ρ_{xx}, while the data of high-magnetic field ρ_{xx} are used to calculate individual n_{si} by the Fourier transform of the Shubnikov-de Haas oscillations.

A solid line in Fig. 2.6 indicates $\rho_{xx}(0)$ of sample A as a function of V_g. One can see that $\rho_{xx}(0)$ decreases with V_g up to -0.8 V, and increases in turn while the total electron density $n_{total} \equiv n_{s1} + n_{s2}$ remain increasing with V_g. A resistance peak appears clearly at $V_g = -0.48$ V with a peak to valley (P / V) ratio of 1.5. Further increase of V_g leads to the decrease of $\rho_{xx}(0)$ to almost half of that at $V_g = -0.8$ V. Closed circles in Fig. 2.6 plot a magnetoresistance $\triangle\rho_{xx}(0.3\text{T})$. When $V_g < -0.8$ V, $\triangle\rho_{xx}(0.3\text{T})$ is almost zero, which indicates that one subband is occupied. In the range of V_g where ρ_{xx} increases with V_g, $\triangle\rho_{xx}$ becomes positive. This indicates the fact that two conducting channels with different mobilities exist. When ρ_{xx} gets close to its peak, $\triangle\rho_{xx}$ starts to decrease and
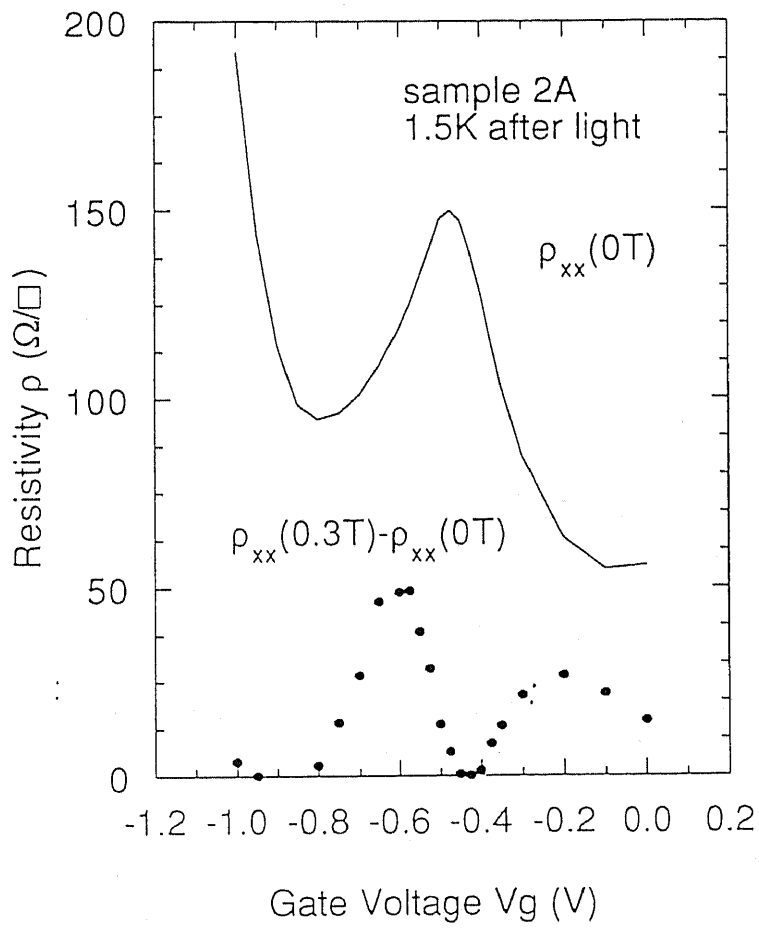
Figure 2.6: The channel resistivity $\rho_{xx}(0)$ of sample 2A at 1.5 K plotted as a function of gate voltage (solid line). The closed circles show the magnetoresistance $\Delta\rho_{xx}$ at 0.3 T.
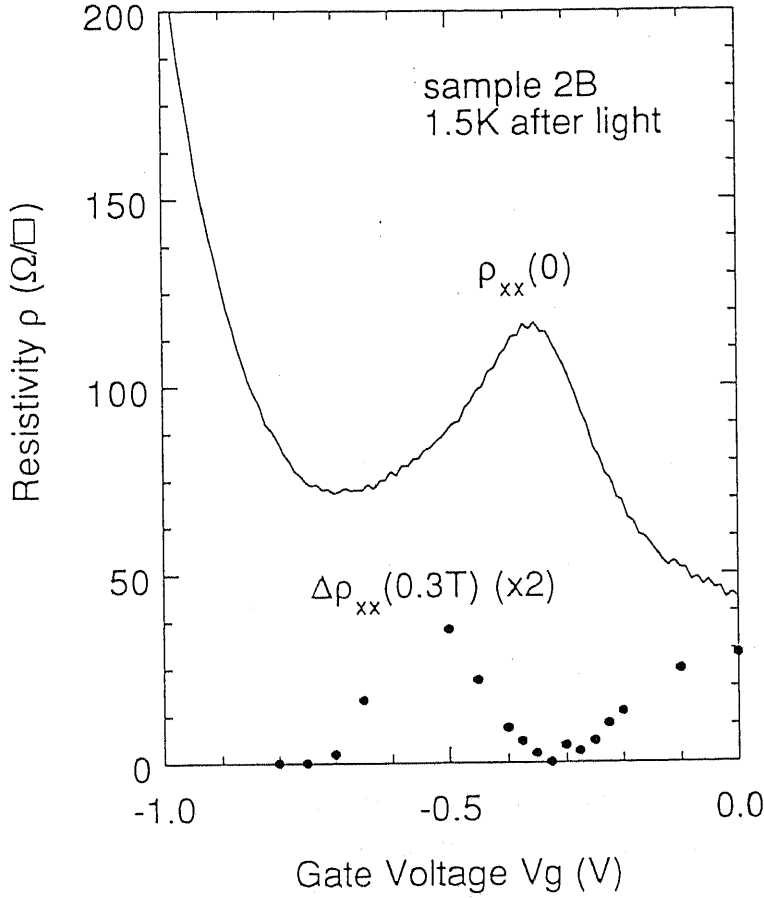
Figure 2.7: The channel resistivity $\rho_{xx}(0)$ of sample 2B at 1.5 K plotted as a function of gate voltage (solid line). The closed circles show the magnetoresistance $\Delta\rho_{xx}$ at 0.3 T.

reaches almost zero at around $V_g = -0.43$ V. From Eq.(2.8), this can be interpreted as the fact that all the electrons have the same mobility.

One should note, however, that $\Delta\rho_{xx}$ reaches zero at slightly higher V_g than -0.48 V, at the peak position for $\rho_{xx}(0)$. This can be explained as follows. At resonance, the overlap of wavefunctions and the scattering potential becomes almost the same for both symmetric and antisymmetric states. Here one should note that just at resonance there is a difference between the electron densities n_{s1} and n_{s2}, which is proportional to the tunnel gap ΔE_{SAS}. This should cause a difference in mobilities μ_1 and μ_2 since the mobility μ depends on the electron density n in the relation $\mu \sim n^\gamma$, where γ is $1 \sim 2$ at low temperatures. [91]

Figure 2.7 displays $\rho_{xx}(0)$ and $\Delta\rho_{xx}(0.3T)$ of sample 2B. There also appears a prominent peak of $\rho_{xx}(0)$ at $V_g = -0.35$ V, with P / V ratio of 1.5. The $\Delta\rho_{xx}(0.3T)$ *vs* V_g curve (closed circles) shows the same behavior as that of sample 2A. The resonance features for

sample 2A and 2B are in accordance with theoretical predictions.

Here we derive the intrinsic mobilities μ_{top} and μ_{bottom} of the δ-doped top QW and undoped bottom QW, respectively. When $\Delta\rho_{xx}$ is zero, one can readily determine n_{total} and μ_{total} in the same manner as in the case of a single channel transport from the measured Hall coefficient R_H. At the resonant point, n_{total} and μ_{total} are found to be 8×10^{11} cm^{-2} and $65,000$ cm^2/Vs, respectively. We also found $n_{s1} = 4 \times 10^{11}$ cm^{-2} and $\mu_1 = 220,000$ cm^2/Vs at $V_g = -0.7$ V, those which correspond to the saturated electron density and the intrinsic mobility in undoped QW. Assuming that the scattering rates $\tau_i^{tr} = (m^*/e)\mu_i$ in the QW's are addable, namely, $\mu_{total}^{-1} = 1/2(\mu_{top}^{-1} + \mu_{bottom}^{-1})$, [35] the intrinsic mobility μ_{top} of δ-doped QW is estimated to be $38,000$ cm^2/Vs. Following the manner described in Ref. [86], we calculated n_{si} and μ_i from the data of $\rho_{xx}(B)$ and $\rho_{xy}(B)$, and found $n_{s2} \sim 4.2 \times 10^{11}$ cm^{-2} and $\mu_2 \sim 220,000$ cm^2/Vs, and $n_{s1} \sim 6.7 \times 10^{11}$ cm^{-2} and $\mu_1 \sim 67,000$ cm^2/Vs, respectively. One may notice that μ_1 at $V_g = 0$ V ($67,000$ cm^2/Vs) is about twice as high as that of the intrinsic mobility in the δ-doped QW ($37,000$ cm^2/Vs). This increase in μ_2 should be attributed to the increase of n_{s1} by a factor of 1.6. Hence, it can be deduced that at $V_g = 0$ V the wavefunction is well confined in each QW.

On the contrary, $\Delta\rho_{xx}(B)$ of sample 2C does not vanish even at resonant bias. In Fig. 2.8, $\rho_{xx}(B)$ at various V_g are plotted as functions of B up to 2T. When $V_g > -0.7$ V, where electrons populate both QW's, one can see a parabolic increase of $\rho_{xx}(B)$. In Fig. 2.9, $\rho_{xx}(B)$ and $\Delta\rho_{xx}(B)$ are plotted as functions of V_g by a solid line and closed circles, respectively.

The magnetic-field-dependence of $\Delta\rho_{xx}$ and Hall coefficients R_H as well as the spectrum of the Fourier transform of Shubnikov-de-Haas oscillation were analyzed to determine the mobility and the electron density of each subband. It was found out that the intrinsic mobility μ_{bottom} of the undoped QW channel is $140,000$ cm^2/Vs at $V_g = -0.8$ V (at the valley of $\rho_{xx}(0)$), and decreases down to $50,000$ cm^2/Vs at the resistance peak. At this V_g, the mobility μ_2 of the lower mobility channel is found to be less than $\sim 10,000$ cm^2/Vs.

2.3.3 Discussion

To explain the observed difference in $\rho_{xx}(B)$ between these samples, we should refine the model of resonant coupling. In sample 2B, the density of Si donors $N_\delta = 1 \times 10^{10}$ cm^{-2} appears to be low enough to regard these dopants as a weak perturbation. Hence, the wavevector $\mathbf{k} = (k_x, k_y)$ in the QW plane serves as a good quantum number and electron waves can propagate coherently in the channel. Indeed, the level broadening of both subbands estimated from their mobilities are smaller than the coupling energy
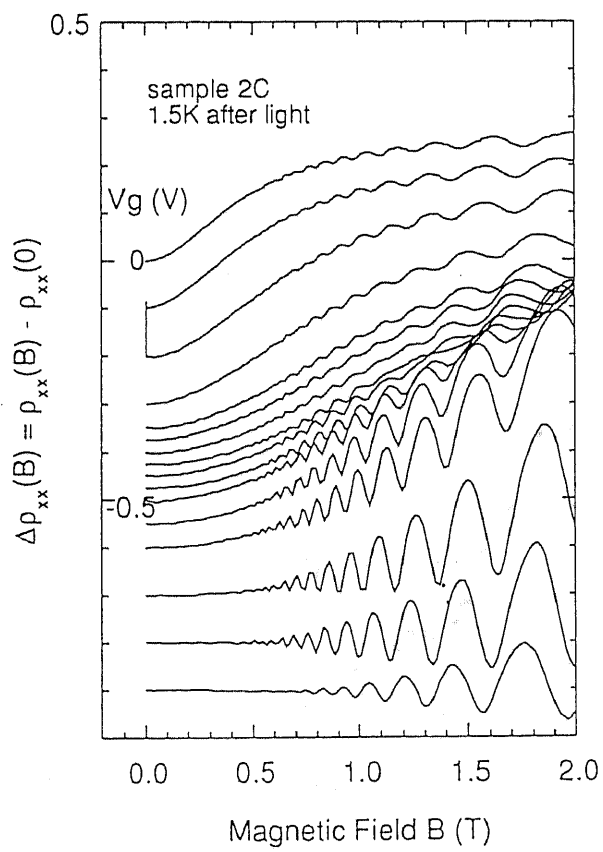
Figure 2.8: The magnetoresistances $\Delta\rho_{xx}$ of sample 2C plotted as functions of B for a different gate voltages $-0.9 < V_g < 0$ V.
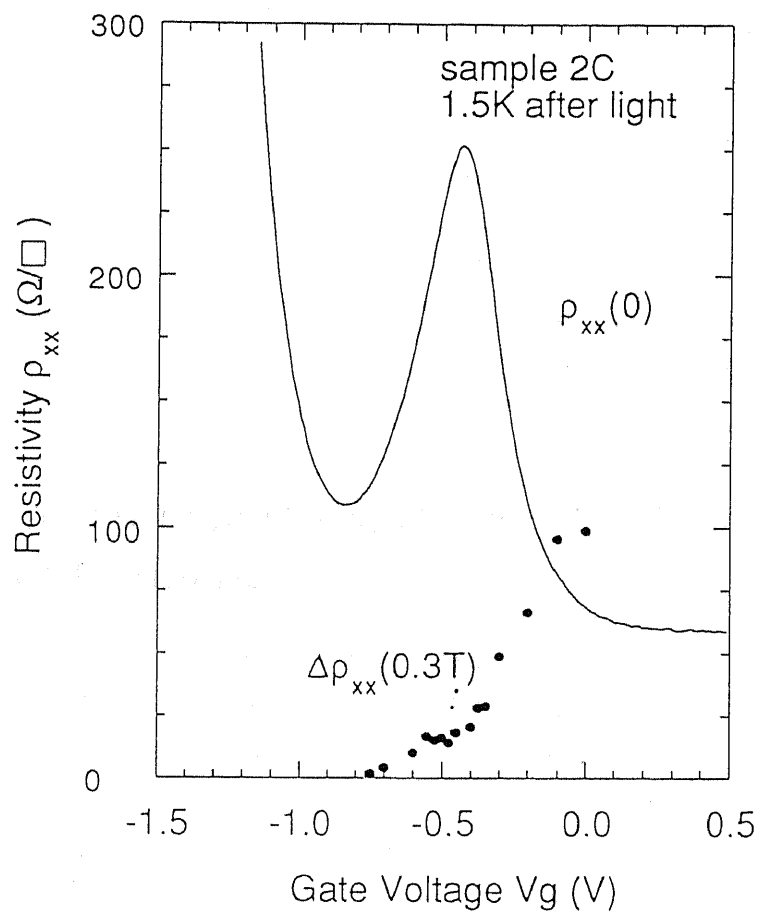
Figure 2.9: The channel resistivity $\rho_{xx}(0)$ of sample 2C at 1.5 K plotted as a function of gate voltage (solid line). The closed circles show the magnetoresistance $\Delta\rho_{xx}$ at 0.3 T.

$\Delta E_{SAS} \sim 1.7$ meV. As a result, the resonant coupling of two levels takes place almost ideally and uniformly over the channel.

In contrast, the resonant coupling effect observed in sample 2C is certainly beyond the simple model of the uniform resonance. For instance, the fact that measured μ_2 (less than $10,000$ cm^2/Vs) is far less than μ_1 ($\sim 50,000$ cm^2/Vs) even at resonance, indicates that resonance enhances the tunneling only partly and does not lead to the complete delocalization of wavefunctions. These complications are due to the high density $N_\delta = 2 \times 10^{11}$ cm^{-2} of donors that causes substantial level broadening and potential fluctuations because of the overlap of bound states. The resonant coupling under such circumstances should be described by a refined model, in which the energy uncertainty δE_2 and potential fluctuation δV in the doped well are taken into account. For instance, δE_2 given by the lower mobility μ_2 ($\sim 10,000$ cm^2/Vs) is comparable with (or bigger than) the coupling energy ΔE_{SAS}. Such a large δE_2 suppresses the coherent propagation in both QWs and, therefore, prevents the formation of uniformly coupled states but, instead results in position-dependent partial coupling.

2.4 Quantum Transport Expression for Non-Uniform Resonant Coupling

The resonance feature observed in a heavily doped sample (2C) is found to be far from a semi-classical picture. In other words, it is not valid to describe the electronic states by single-particle wavefunctons as symmetric $|S\rangle$ and antisymmetric $|AS\rangle$ states. This inapplicability of the semi-classical description has been theoretically emphasized by Vasko. [92, 93] He has developed a quantum transport theory for a DQW structure with asymmetric scattering, which can be applied to the case even when $\delta E_i > \Delta E_{SAS}$. In his theory, the electronic states are represented by linear-combinations of eigenfunctions for isolated QW's. [80] He used a 2×2 Hamiltonian as a model taking into account the tunnel coupling and the asymmetric scattering potential.

Using the expression given by Vasko, [92] the increase of the resistance $\Delta R \equiv R - R_0$ at resonance is written as [94]

$$\frac{\Delta R}{R_0} = \frac{t^2}{(1+t^2)} \frac{(r-1)^2}{4r} \tag{2.9}$$

where r is the intrinsic mobility ratio $r = \mu_{bottom}/\mu_{top}$, R_0 the resistance expected without resonant tunneling, i.e., $R_0 = [en_{total}/2(\mu_{top} + \mu_{bottom})]^{-1}$, and

$$t = 2\Delta E_{SAS} \frac{\tau_{top} \tau_{bottom}}{\hbar(\tau_{top} + \tau_{bottom})}. \tag{2.10}$$

Note that τ_i in Eq.(2.10) is not the transport scattering time $\tau_i^{\text{tr}} = (m^*/e)\mu_i$, but the quantum life time, for which a long-range scattering potential (associated with a change of a small wave number q ~ 0) is effective. Kurobe et al. have carried out experiments similar to the present work independently, and made comparison between their results and Eq.(2.9), finding that the use of τ_i^{tr} as τ_i leads to large discrepancies. [94] Taking into account the fact that in modulation-doped heterostructures $\tau^{\text{tr}}/\tau = 4 \sim 10$, [95] the origin of the difference between the experiments and the theory can be understood. From the data of Shubnikov-de-Haas oscillation in Fig. 2.8, we estimated τ_{bottom} for sample 2C and found $\tau_{\text{bottom}}^{\text{tr}}/\tau_{\text{bottom}}$ to be ~ 7. However, τ_{top} can not be obtained from Shubnikov-de Haas oscillations because electrons of much higher mobility exist at the same time. For this purpose, one needs to make further experiments such as cyclotron resonance measurements.

2.5 Summary

In this chapter, we have theoretically and experimentally studied the electron transport in impurity-doped double quantum well (ID-DQW) structures. By studying the dependence of the low-field magnetoresistance on the resonance-controlling gate voltage, it is found that coupling of two levels takes place uniformly, or resonant tunneling is achieved coherently when the energy broadening of each level is less than the tunneling energy, while such a resonance feature was not observed in a heavily doped DQW, for which an alternative theory is required.

Chapter 3

Effects of In-Plane Magnetic Fields on Electron Transport in Double Quantum Wells

3.1 Introduction

Effects of a transverse magnetic field on the tunnel transport in semiconductor heterostructures have been extensively studied. Let us consider the motion of an tunneling electron injected from a two-dimensional (2D) emitter into a quantum well (QW) collector as shown in Fig. 3.1(a). In essence, application of a magnetic field $\mathbf{B}$ (taken in the x-direction) parallel to the tunnel barrier leads to (i) quantization of the motion of electrons into interfacial Landau states, (ii) deflection of their orbits in the tunnel barrier or the collector by a Lorentz force, or (iii) relative displacement of the origin of the in-plane momentum (k) space for the electron states in the collector. These effects, under the restrictions which are forced by the conservation of in-plane momentum k and total energy E in a tunneling process, give rise to a modulation of tunnel-transport properties such as the current-voltage (I-V) characteristics.

(i) occurs when a magnetic field is so strong that the width L_C of collector QW is larger than twice the cyclotron radius l_c. In this case, two-dimensional (2D) electrons in the emitter QW are not allowed to tunnel into the bulk states in the collector. Instead, tunnel transfer to the interfacial Landau states, i.e. the edge states, takes place. [96, 97]

(ii) is the case where L_C is comparable to l_c, resulting in a chaotic behavior of electron motion in the collector QW. [98]

(iii) is most likely for the tunneling between 2D systems achieved in double barrier (DB) or double quantum well (DQW) structures, where the quantized energy in each QW is not affected by parallel-magnetic fields B, namely, B can be treated as a perturbation. In this case, the effect of B on the motion of an electron is equivalent to replacing the
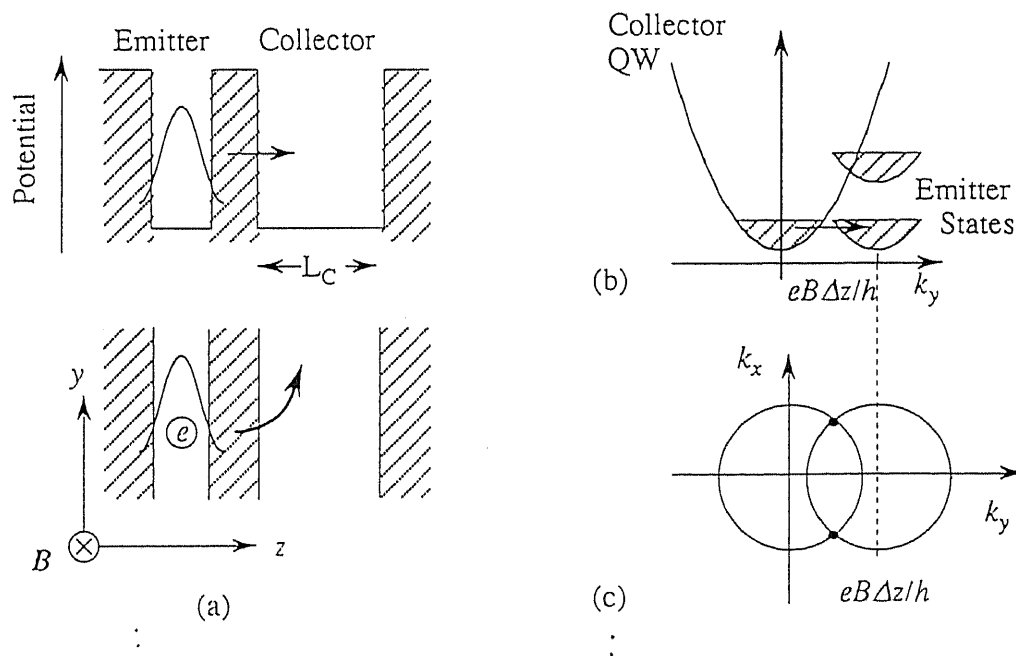
Figure 3.1: (a) A model of tunneling from a two-dimensional emitter to a collector in a magnetic field parallel to the barrier. (b) Displaced parabolic dispersion relations of the states in the emitter and the collector QWs. Hatched area indicates the states in the emitter which are filled with electrons. (c) Displaced two Fermi circles at zero-field resonance in a parallel magnetic field B. In the case of equibrium 2D-2D tunneling, the cross-section between two Fermi circles is reduced to two points when the displacement $eB\Delta z < 2\hbar k_F$

canonical momentum $\hbar k_y$ by $\hbar k_y - eB\Delta z$, where $\hbar$ is the reduced Plank constant, e the elementary charge, k_y the wavenumber of the electron in the emitter, and Δz the mean distance between the 2DEG's in the emitter and the collector QW's. In DB structures, the resonant tunneling current at a zero-field resonant bias will decrease rapidly with a transverse magnetic field. [99] As shown in Fig. 3.1(b), the overlap between emitter and collector states is much reduced when the parabolic dispersion relations of k of the emitter states are shifted along k_y with respect to those of the collector states. Using this feature, complicated dispersion relations in QW's have been investigated by magnetotunneling spectroscopy. [100]

The equibrium 2D-2D tunneling has been studied by Eisenstein et al. in a DQW structure with independent ohmic contacts which are realized by a selective depletion technique. [42]. In this case, zero-field tunneling is allowed to take place only when the two levels are exactly aligned because only the electrons in the vicinity of the Fermi surfaces can participate in a tunneling event with their in-plane momenta unchanged. [43] When a magnetic field is applied parallel to the layers, as shown in Fig. 3.1(c). There exist only two states at which two displaced Fermi circles cross each other, resulting in drastic decrease of the tunnel conductance. [44]

Note that the experiments referred above have been done in weakly-coupled systems. For the case of a tightly-coupled 2DEG system, on the other hand, only a few experiments were made before we started the present work. [101,102] In this chapter, we investigate the effects of an in-plane magnetic field on parallel electron transport in intermediately coupled DQWs. Specifically, we employ here DQW structures in which the gate-controlled resonant coupling results in the resonant change of a resistance. [35]

3.2   Decoupling of Resonance States by In-Plane Magnetic Fields

In Chaper 2, we studied the dependence of the channel resistance on a magnetic field applied perpendicular to the layers. In that case, the magnetic field is responsible for the in-plane motion of electrons. The wavefunctions in the z-direction, the symmetric and antisymmetric states at resonance, should not be modified by B in a single particle picture. The observed positive magnetoresistance arises from the fact that the Lorentz force $F \sim v_i \times B$ could not be canceled by the averaged Hall electric field across the channel when the velocities v_i, i.e. the mobilities μ_i of two subbands were not equal to each other.

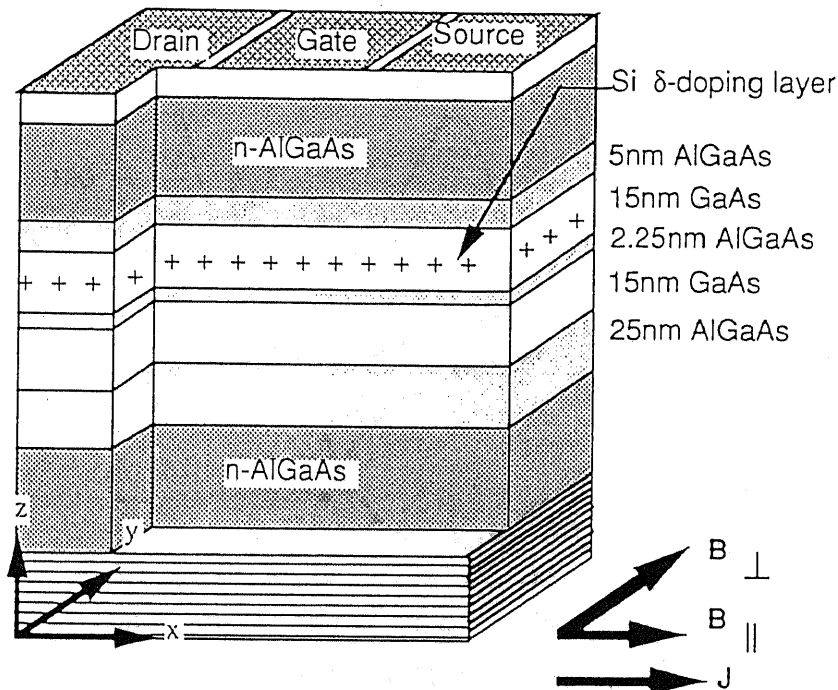In contrast, the resonant coupling in DQW structures should be influenced by a

Figure 3.2: The cross-sectional view of the sample structure is schematically shown. The concentration of Si$^+$ in the δ-doping layer is 1×10^{10} cm^{-2} for sample 3A and 2×10^{11} cm^{-2}, respectively.

magnetic field parallel to the QW layers. This change of coupling should be reflected in the resistance peak in parallel transport. However, the behavior of electrons should depend on the direction of magnetic field with respect to the current flow direction. As shown in Fig. 3.1(c), the two displaced Fermi circles are not isotropic with respect to the origin of k-space. Hence, we have experimentally studied the effects of in-plane magnetic fields for both cases where the fields are applied parallel (B ||) and perpendicular (B ⊥) to the current J in this section.

3.2.1   Sample Structures and Experimental Setup

The samples 3A and 3B studied here are the same as sample 2B and 2C used in Chapter 2, respectively. In Fig. 3.2, we show again a cross-sectional view of the sample structure. The DQW consists of two 15 nm-wide GaAs quantum wells separated by 2.25 nm-wide Al$_{0.26}$Ga$_{0.74}$As barrier. At the center of the upper quantum well, a Si$^+$ δ-doping layer (1×10^{10} cm^{-2} for sample 3A, and 2×10^{11} cm^{-2} for sample 3B, respectively) is inserted to make a difference in the mobilities of two 2DEG's.
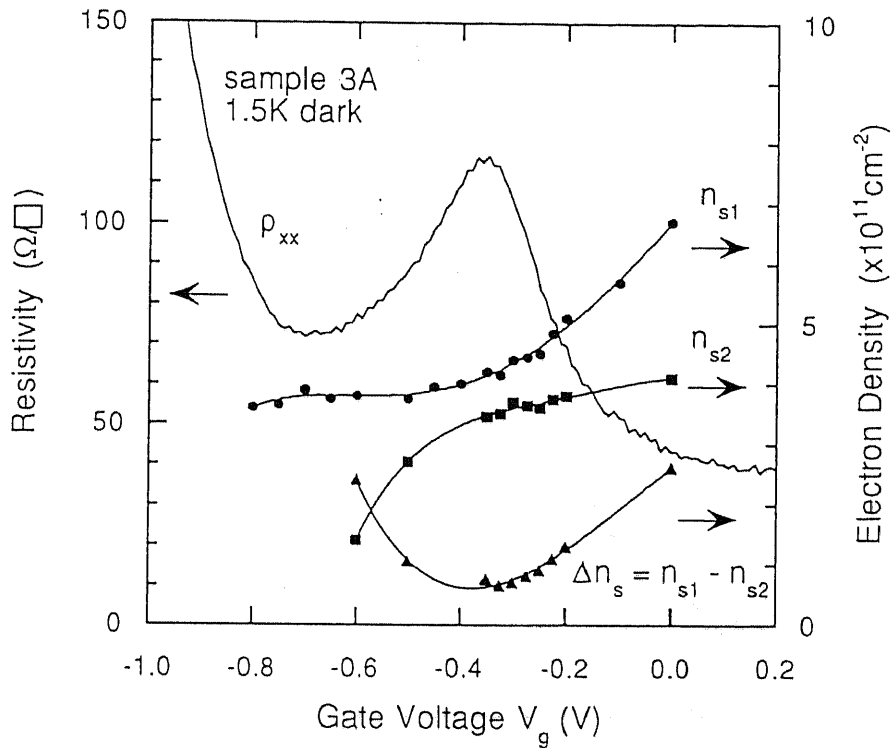
Figure 3.3: The zero-field channel resistivity ρ_{xx} vs. gate voltage V_g characteristics at 1.5 K is shown by a solid line. Closed circles and squares indicate the electron densities of individual subbands. Closed triangles are the difference between them.

A Hall bar geometry with a 200 μm long and 50 μm wide channel was defined by a conventional photolithography technique. A Schottky gate was then formed by deposition of Aluminum in vacuum, and ohmic contacts were made by alloying InSn at 400 °C to both QW's.

As described in Chapter 2, the sample 3A shows the resonance features which are predicted in a theory based on a single-particle picture. [35] Furthermore, we measured the Shubnikov-de-Haas oscillations at different gate voltages V_g with magnetic fields applied perpendicular to the layers in order to confirm the electron population in the lowest two subbands. Electron concentrations n_{s1} and n_{s2} were evaluated from the power spectrum of the Fourier transform, and plotted in Fig. 3.3, as well as the channel resistivity ρ_{xx} at zero magnetic field. From these two curves, one can readily determine the energy levels E_1 and E_2 with respect to the Fermi energy E_F. It is clearly seen that $n_{s1}(V_g)$ and $n_{s2}(V_g)$ anticrosses each other at $V_g = -0.35$ V. The minimum of the energy separation ΔE_{SAS} between these two levels is estimated to be ~ 2 meV. It is in good accordance with the theoretical value 1.7 meV, which is obtained from a self-consistent calculation.
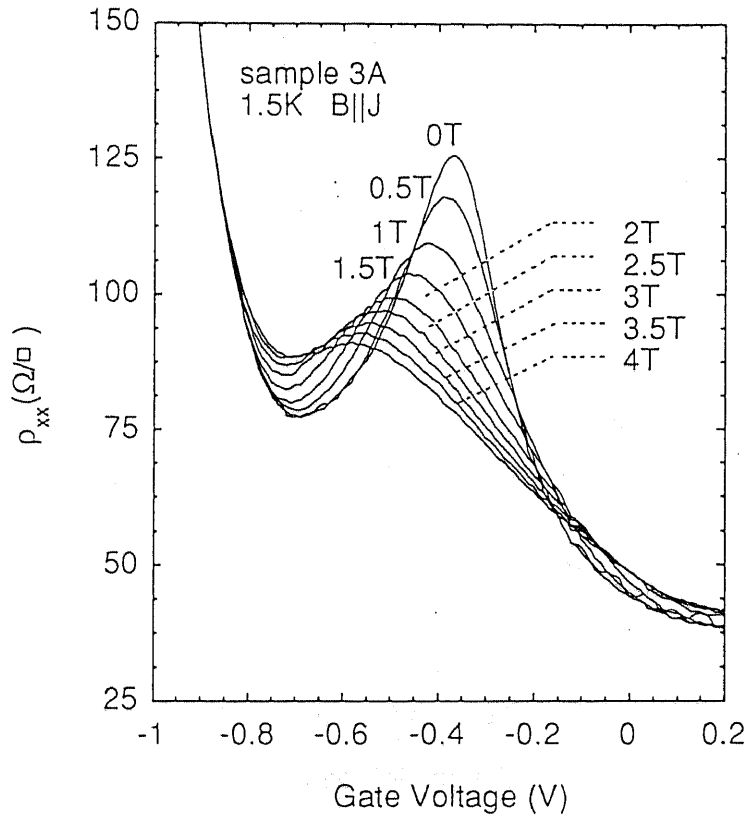
Figure 3.4: The longitudinal magnetic field $B\|$ dependence of ρ_{xx} for sample 3A plotted as functions of V_g.

Next, we describe the experimental set-up for the resistance measurements in parallel magnetic fields. The measurement was carried out at 1.5 K by ac lock-in technique with a small excitation current of 10 nA at 15 Hz, which was fed by a signal generator with a 10 MΩ resistor connected in series. The channel resistance ρ_{xx} was measured at several values of magnetic fields with the gate voltage V_g scanned from 0.5 V to −1.0 V. The Hall resistance ρ_{xy} was also measured simultaneously. To apply a magnetic field pricisely parallel to the layers, the sample was fixed where the Hall voltage across the channel vanishes. The stage, on which the sample was mounted, can turn round on only one axis: The direction of the channel with respect to the magnetic field was fixed outside before launching the rod into the liquid He^4 cryostat.

3.2.2 Experimental Results

In Fig. 3.4, the channel resistivity ρ_{xx} for $\mathbf{B}\|\mathbf{J}$ are plotted as functions of V_g. The resistance peak decreases with the increase of $\mathbf{B}_{\|}$, indicating that the coupling is weakened. The
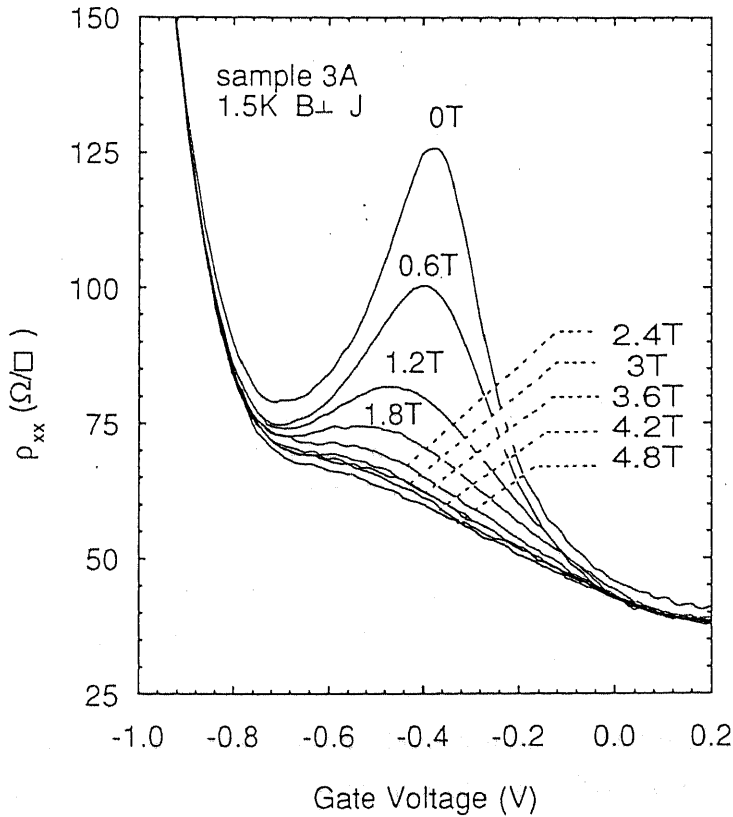
Figure 3.5: The transverse magnetic field $B\perp$ dependence of ρ_{xx} for sample 3A plotted as functions of V_g.

rate of quenching with the magnetic field is, however, rather small. Even at 4 T, the peak remains visible. Simultaneously, the position of the peak is seen to shift toward the negative V_g, with the peak width broadened. When V_g is biased at some value in the region of off-resonance, ρ_{xx} increases. This tendency is most obvious at the valley point of ρ_{xx}, where the second subband starts to be occupied by newly induced electrons.

Secondly, we studied the ρ_{xx}-V_g characteristics for $B\perp J$. The result is shown in Fig. 3.5, where the resistance peak is found to fall down much more abruptly. The quenching rate for $B\perp J$ up to ~ 1 T is greater by a factor of 3 than the case $B\|J$. Around 2.5 T, the peak structure is completely vanished. Note that two Fermi circles in k space will be circumscribed at $B = \hbar\sqrt{2\pi n_i}/e\Delta z \sim 12$ T. In the range of B where the experiments were made, two crossing points were preserved, as shown in Fig. 3.1(c). Note also that the magnetoresistance under off-resonant condition is negative, contrary to the positive magnetoresistances for $B\|J$. The shift of the peak position is also found, but is far smaller than that for $B\|J$.
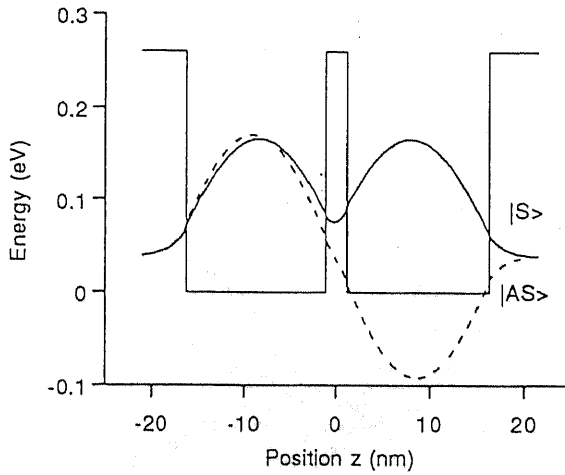
Figure 3.6: Symmetric ($|S\rangle$) and antisymmetric ($|AS\rangle$) wavefunctions in a symmetric double quantum well potential are plotted.

In the case of $\mathbf{B}\perp\mathbf{J}$, one must consider the possibility that the in-plane magnetic field induces the Hall electric field in the direction of the DQW potential. It may lead to an excess charge transfer from one well to the other, or deformation of a wave function in each QW resulting in a kind of mobility modulation. [32] In such a case, ρ_{xx} should depend on the polarity of the magnetic field or the current because of the asymmetry of the mobilities. We found this effect to be negligible, for in dc measurements no difference was observed when the polarity of the magnetic field was reversed.

3.2.3 A Perturbation Theory

First we discuss the anisotropic in-plane magnetic field dependence of the resonance-enhanced resistance. To examine the origin of the quenching of the resistance peak and its marked dependence on the magnetic field orientation, we consider the mixing of the extended eigenstates in the presence of a parallel magnetic field $\mathbf{B}$. As shown in Fig. 3.6, we take the channels in the xy plane and the origin of the z-axis at the center of the barrier between two QWs. The DQW potential $V(z)$ is assumed to be rectangular and symmetric, for simplicity. When $\mathbf{B}$ is in the x-direction, we take the vector potential $\mathbf{A}$ as $(0, -Bz, 0)$ in the Landau gauge. In this case, the motion of electrons in the x-direction can not be affected by $\mathbf{B}$. By treating the DQW system as a unit, the z component of wavefunctions $\psi_i(z)$ (i denotes the index of the level) are given by solving the following
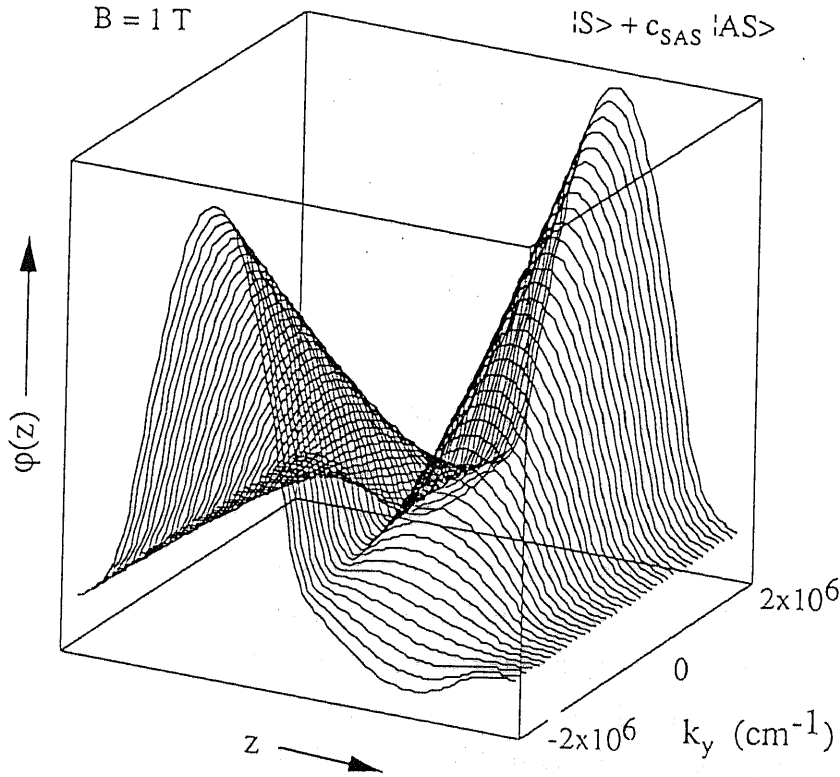
B = 1 T $|S\rangle + c_{SAS}|AS\rangle$

Figure 3.7: Calculated wavefunctions $|S\rangle + c_{SAS}|AS\rangle$ at B = 1 T are shown for -2×10^6 cm^{-1} < k_y < 2×10^6 cm^{-1}.

Schrödinger equation

$$\{-\frac{\hbar^2}{2m^*}\frac{\partial^2}{\partial z^2} + V(z) + \frac{1}{2m^*}\cdot eBz(\hbar k_y + eBz)\}\psi_i(z; k_y, B) = E_i(k_y, B)\psi_i(z; k_y, B) \quad (3.1)$$

where m^* is the effective mass of electrons and E_i the quantized level for the i-th subband. If a magnetic field is sufficiently low, the term $H' = 1/2m^*\cdot eBz(\hbar k_y + eBz)$ can be regarded as a perturbation. Then the wavefunctions $\psi_i(z)(i = 1, 2)$ can be expressed as linear combinations of symmetric ($|S\rangle$) and antisymmetric ($|AS\rangle$) states, which are the eigenfunctions of the Hamiltonian with no perturbation, $H_0 = -\hbar^2/2m^*\cdot\partial^2/\partial z^2 + V(z)$. In the present case, the mixing is mainly between $|S\rangle$ and $|AS\rangle$ since higher excited states are separated with large energy as compared with ΔE_{SAS}. The mixing coefficient c_{SAS} is then given by

$$c_{SAS} = -\langle S|\frac{1}{2m^*}\cdot eBz(eBz + \hbar k_y)|AS\rangle/\Delta E_{SAS} \quad (3.2)$$

In Fig. 3.7, the calculated wavefunction $|S\rangle + c_{SAS}|AS\rangle$ at $B = 1$ T is plotted as a function of k_y. When $k_y = 0$, the mixing does not occur because $|S\rangle$ is even and $|AS\rangle$ is odd with respect to the origin of z. Thus the wavefunctions remain delocalized. As k_y

deviates from zero, the mixing increases and leads to a situation where the probability function $|\psi_i(z; k_y, B)|^2$ starts to concentrate in one QW, while that corresponding to $-k_y$ concentrates mainly in the other well. When k_y gets as large as the Fermi wave number $k_F \sim 1.6 \times 10^6$ cm^{-1} for $n_s = 4 \times 10^{11}$ cm^{-2}, the numerically calculated c_{SAS} reaches ~ 1 even at $B = 1$ T. At that point, the envelop functions $\psi_i(z; k_y, B)$ are reduced to $|S\rangle + |AS\rangle$ and $|S\rangle - |AS\rangle$, which are degenerate states in isolated QWs as shown in Fig. 3.7, although the validity of this approximation must be examined. An alternative treatment of a strong in-plane magnetic field will be discussed in the next section.

From the above discussion, it is clear that decoupling of symmetric and antisymmetric states by the in-plane magnetic filed and the subsequent decrease of the probabilities of the impurity scattering strongly depend on k_y, that is, these effects are reflected only on the electronic states with large value of k_y. As the electric field is applied in the x direction in our case, the conductance is mainly dominated by electrons with large k_x. Hence, the influence of δ-doped impurities on the electron transport decreases only with a modest rate; this explains why the magnetic field effect was small for $\mathbf{B} \| \mathbf{J}$.

When the in-plane filed $\mathbf{B}$ is in the y direction, i.e. $\mathbf{B} \perp \mathbf{J}$, one can expect that the decoupling of electronic states into two isolated 2DEGs should take place most efficiently for electrons with large k_x. Since these electrons dominate the current transport and since electrons localized in the undoped QW are released from the δ-doped impurities, the magnetic field dependence of the magnitude of the resistance peak should be far larger in this case, which is in accordance with the experimental results.

3.2.4 Non-Uniform Resonant Coupling Case

We also carried out the in-plane magnetoresistance measurements for the sample 3B. In Figs. 3.8 and 3.9, the channel resistivity ρ_{xx} in $\mathbf{B} \| \mathbf{J}$ and $\mathbf{B} \perp \mathbf{J}$ configurations are plotted as functions of V_g, respectively. These results are quite similar to those of the sample 3A, except for the off-resonant magnetoresistance. The resonance-induced resistance peak was quenched more rapidly with increasing $\mathbf{B} \perp \mathbf{J}$, than $\mathbf{B} \| \mathbf{J}$, as shown in Figs. 3.8 and 3.9. As argued in the previous chapter, we can not apply the perturbation model to sample 3B because the random potential due to the heavily doped impurities (2×10^{11} cm^{-2}) prevents the "uniform" resonant coupling which is essential for a description of single-particle wavefunctions. From the experimental results, however, we speculate that the features of such coupled symmetric and antisymmetric states are preserved to some extent in the electronic states at the Fermi energy even when the potential is heavily disordered. For further discussion, we should refine our model, as discussed in the next section.
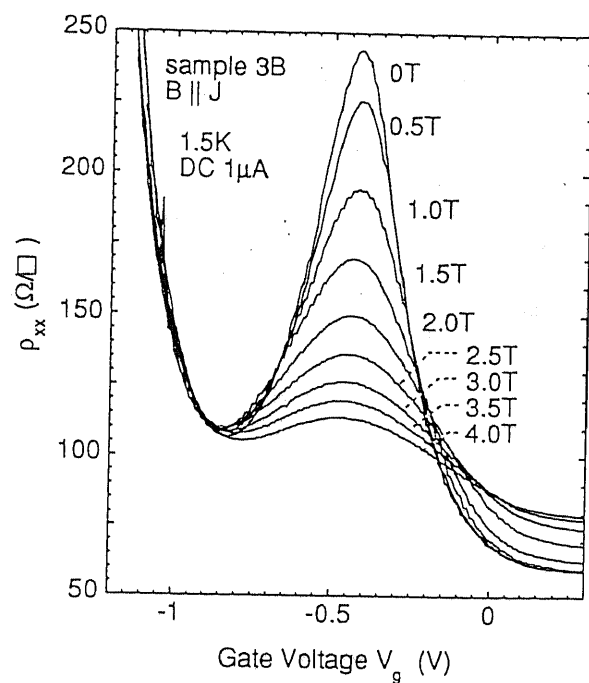
Figure 3.8: The longitudinal magnetic field $B\parallel$ dependence of ρ_{xx} for sample 3B plotted as functions of V_g.
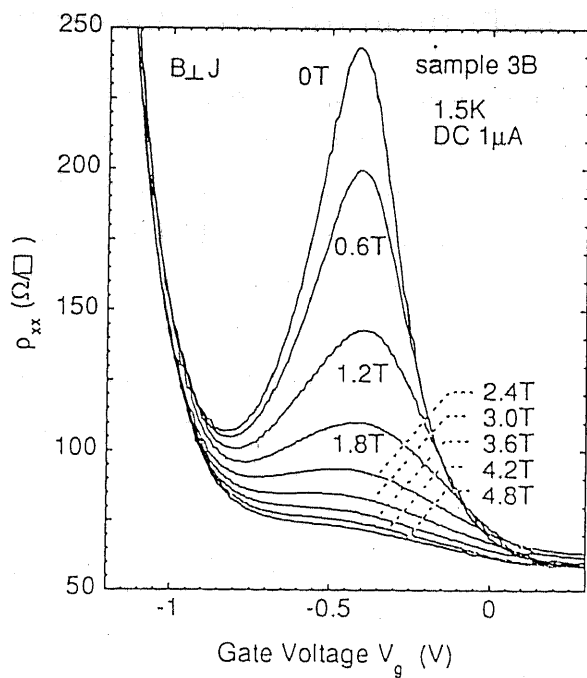

Figure 3.9: The transverse magnetic field $B\perp$ dependence of ρ_{xx} for sample 3B plotted as functions of V_g.
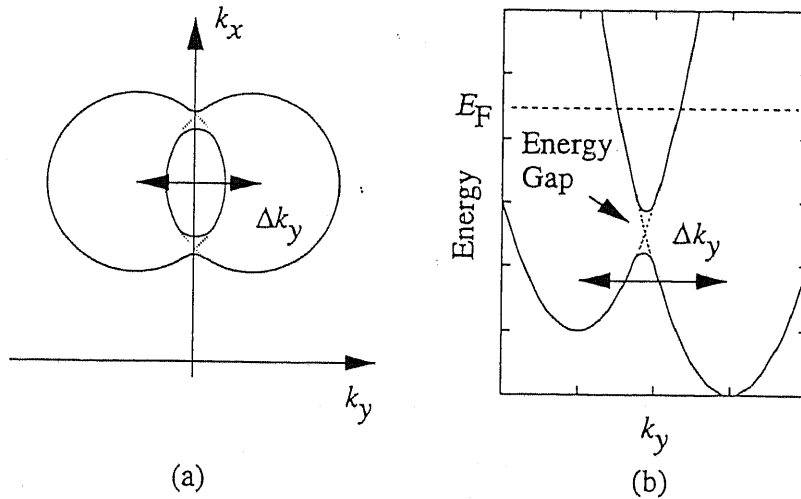
Figure 3.10: Schematic illustrations of (a) two anti-crossing Fermi circles in strongly coupled double quantum wells when the displacement $\Delta k > k_F$, and (b) the dispersion relation with a partial energy gap.[103,104]

3.3 Discussions

3.3.1 Magnetoresistance in a Strong In-Plane Magnetic Field

In Section 3.2.3, we treated an in-plane magnetic field **B** as a small perturbation, and we were concerned mainly with the deformation of wave functions. In k space, as shown in Fig. 3.1(b) and (c), **B** results in a linear shift of a dispersion relation $E(\mathbf{k})$ of one QW relative to the other along $\mathbf{k} \perp \mathbf{B}$ direction. Therefore, the cross section between two Fermi circles are reduced to only two points in the case of a weak coupling system. [44] In contrast, two dispersion curves anticross as shown in Fig. 3.10(a) when $eB\Delta z/\hbar > k_F$ and the tunnel coupling is sufficiently strong. [103] Under this condition, an energy gap appears at specific k's as shown in Fig. 3.10(b), and the group velocities as well as the density of states $N_{2D}(E)$ are dramatically distorted at the edges of the gap. [103,104]

In the present work, where $k_F \sim 1.6 \times 10^6$ cm^{-1}, the above situation occurs when $B > 6$ T. Therefore, we can rule out this effect but the group velocity should change even when $B < 6$ T. It may give rise to an additional magnetoresistance, not related to the in-plane magnetic field dependence of the resonantly-enhanced resistance peak which was discussed in the previous section.

For the observed in-plane magnetoresistance and its anisotropic dependence under off-resonance, the mixing of the lowest two levels has been also estimated from Eq.(3.2)

and found to be negligibly small. Therefore, we deduce that the non-zero in-plane magnetoresistance at $V_g \sim -0.7$ V in Figs. 3.4–3.5 (positive for $\mathbf{B}\|\mathbf{J}$, and negative for $\mathbf{B}\perp\mathbf{J}$, respectively) is a feature of a 2DEG in a single QW, too.

3.3.2   Quantum Transport Theories for the In-Plane Magnetic Field Dependence of Resonance-Induced Resistance

Almost simultaneously, a few other groups have independently made experiments similar to the present work, [94,105–107] and reported a quantitative analysis using quantum transport theory. [106] Berk et al. developed microscopic model of electron transport in DQW's employing the basis of eigenstates of uncoupled QW's and representing the coupled states by a 2×2 Hamiltonian in a similar manner as in Ref. [92]. They derived an expression of the in-plane magnetic field B dependence of the resonance resistance based on the Kubo formula as

$$R^{-1}(B) - R_0^{-1} = [R^{-1}(0) - R_0^{-1}]f(B/B_c) \tag{3.3}$$

where $R(B)$ is the channel resistance at resonance, R_0 the resistance without tunnel coupling, and

$$f(x) = \frac{2(\sqrt{1+x^2}-1)}{x^2} \times \begin{cases} 1, & \mathbf{B}\|\mathbf{J} \\ (1+x^2)^{-1/2}, & \mathbf{B}\perp\mathbf{J}. \end{cases} \tag{3.4}$$

The fitting parameter B_c is referred to the characteristic field and given by

$$B_c = \frac{cm^*}{ek_F\tau\Delta z}\sqrt{1 + \left(\frac{\Delta E_{SAS}}{\hbar}\right)^2 \frac{\tau_{bottom}^{tr} + \tau_{top}^{tr}}{2}\tau}, \tag{3.5}$$

where $2\tau^{-1} = \tau_{bottom}^{-1} + \tau_{top}^{-1}$, Δz the average spacing between two QW's, and $\tau_i^{tr} = (m^*/e)\mu_i$. Note that B_c contains an unknown parameter, the average quantum lifetime τ while the transport scattering time τ_i^{tr} can be known by Hall measurements. If one uses τ^{tr} as τ in Eq.(3.5), one expect a large discrepancy between the experiments and the theory, as shown in Chapter 2.4. By comparing the experimental results with the theory, however, one can estimate the small angle scattering time. [106]

Another approach has been examined by Kurobe et al., in which the k-dependent scattering matrix has been numerically computed. [108] Just recently, Vasko and Raichev have improved their theoretical model by taking the long-range correlation of the ionized impurity potential into account, and made comparison with the present data [109] as shown in Fig. 3.11. [110,111] The calculated results (solid lines) are in much better accordance with the experimental results, than those (dashed lines) for which only the short range potentials were considered.
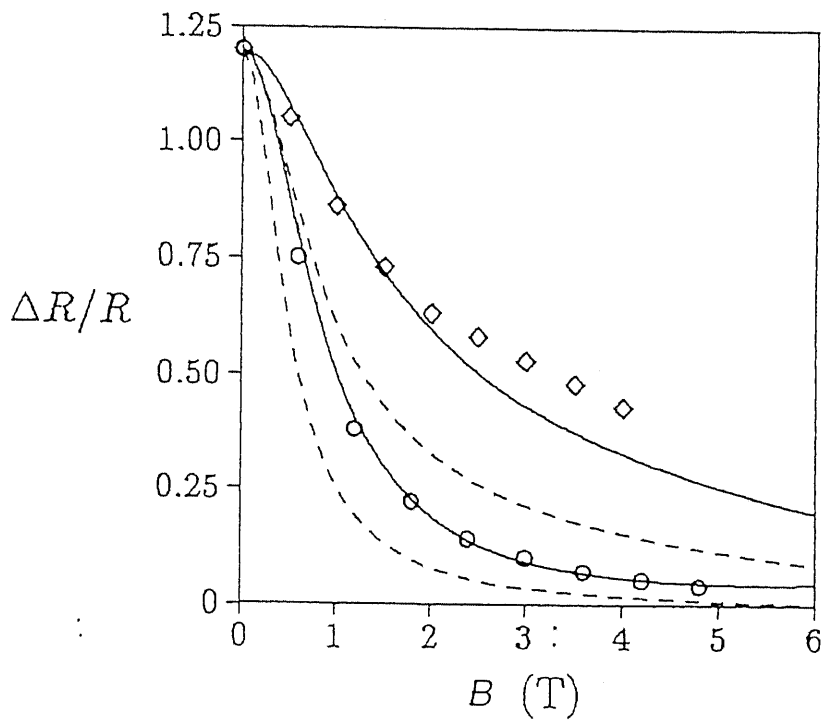
Figure 3.11: Normalized size of the resistance resonance $\Delta R/R$ as a function of an in-plane magnetic field B. Open diamonds ◇ and circles ◦ are the experimental data for $\mathbf{B} \| \mathbf{J}$ and $\mathbf{B} \perp \mathbf{J}$, respectively. Solid lines (dotted lines) are the calculated results taking the long range correlation of the scattering into account (in the case of short-range scattering potentials). Taken from [110]

3.4 Summary

In this chapter, we have investigated the influence of in-plane magnetic fields B on the resonant coupling in selectively impurity-doped double quantum well structures. A resonance-enhanced resistance peak was found to be quenched with increasing B which is much more efficient for a magnetic field directed normal to the current. This anisotropy is successfully ascribed to the magnetic field induced mixing of the extended one-particle wavefunctions.

Chapter 4

Suppression of Resonant Coupling in Double Quantum Wells in the Quantum Hall Regime

4.1 Introduction

As described in Chapter 1.2, electron transport in a double quantum well (DQW) has been of great interest because of its unique properties resulting from the additional degree of freedom. In particular, the effects of a magnetic field applied perpendicular to the sheets of two-dimensional electron gases (2DEG's) and / or the inter- and intra-layer Coulomb correlations on the single-particle tunneling have been extensively studied both theoretically [51–56, 62] and experimentally. [57, 58, 60, 61, 63, 64] Most of the transport measurements have been done in "parallel" configuration, where ohmic contacts were connected to both QW's simultaneously. In these experiments, the magnetoresistance, i.e. the Shubnikov-de-Haas oscillations, have been studied to explore the resonance features [101] or to investigate the characteristics of each quantum Hall state. [57, 60, 63, 64] On the other hand, direct measurement of the tunnel conductance between two 2DEG's has been achieved by using a selective depletion technique. [43] In this "tunnel" configuration, interactions in a weakly tunnel-coupled DQW can be sensitively studied, even in a DQW where the data of the "parallel" transport experiments indicate no more than the features equivalent to those of two independent QW's connected in parallel.

Fabrication of patterned gates on the back is, however, not so easy. One needs to remove the back side of the substrate to reducing it's thickness down to $50 \sim 100 \ \mu m$ so that the back gate can function in the range of an appropriate bias voltage. [42, 91] More recently, an alternative attempt has been made to fabricate back gates by an *in-situ* focused ion implantation process. [112, 113] In the present work, we employed still another scheme to probe resonant tunneling in weakly-coupled DQW's without using
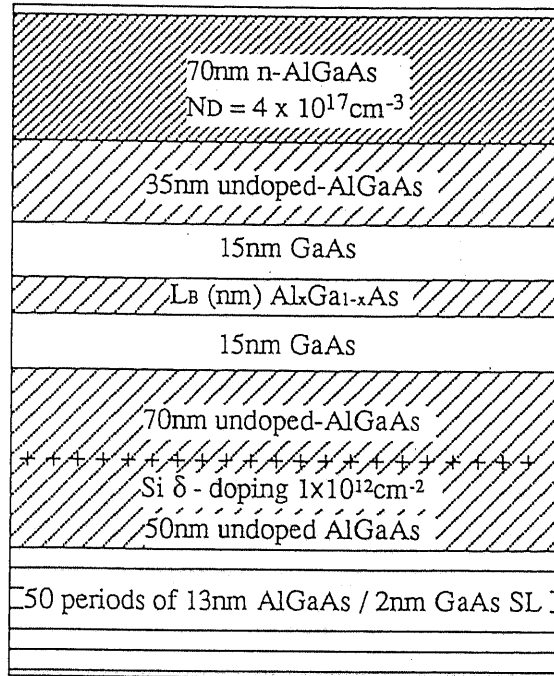
Figure 4.1: Cross-section of sample 4A−4D are schematically shown. Except for the Al content x and the thickness L_B of the central barrier, structural parameters are identical for these samples.

back gates, [102, 113, 114] and we have investigated the in-plane transport properties of tunnel-coupled two 2DEG's in the integer quantum Hall regime.

4.2 Selective Probing of Transport Properties in Double Quantum Wells

4.2.1 Experimental Setup and Methods

For the present experiments, we prepared four DQW samples 4A−4D by molecular beam epitaxy (MBE). The cross sectional view of the sample structure is shown in Fig. 4.1. Each consists of two 15 nm-wide GaAs QW's separated by an $Al_xGa_{1-x}As$ barrier of thickness L_B. Table 4.1 lists the structural parameters x and L_B, and the tunneling energy gap ΔE_{SAS} which is obtained from self-consistent calculations. A Si^+ δ-doping layer is placed 70 nm below the DQW, and a 35 nm-thick undoped AlGaAs spacer is inserted between the top of the DQW and an n-AlGaAs layer (with the doping density of 4×10^{11} cm^{-3}). The samples were grown under the optimized condition for a normal GaAs / AlGaAs single heterostructure. The substrate temperature T_{sub} was 580 ∼ 600

Table 4.1: The Al mole fraction x and the thickness L_B of the central barrier, and energy gap ΔE_{SAS} between symmetric and antisymmetric states resulting from self-consistent calculations. *: The values of ΔE_{SAS} might be smaller than the error in the calculations. One should refer these only for the order estimations.

Sample	x	L_B (nm)	ΔE_{SAS} (meV)
4A	0.28	5	0. 39
4B	0.28	10	0.018
4C	0.28	15	0.0008*
4D	1.0	7	0.0005*

°C and the growth rate f_{GaAs} for GaAs was ~ 0.8 μm/h. Because of the relatively high T_{sub}, a part of the Si dopants in the δ-doping layer below the DQW may migrate toward the growth direction. Following the other experimental study, [115] the effective thickness of the bottom undoped spacer should be ~ 60 nm.

Using these wafers, we fabricated novel field effect transistor (FET) structures with a Hall bar geometry. The top view of the layout of the device is schematically shown in Fig. 4.2. First, the Hall bar geometry was defined by a photolithographic technique and mesa-etched in $H_3PO_4:H_2O_2:H_2O = 1:1:8$ solution for 30 sec at room temperature. The channel width is 50 μm, and spacing between two potential probes is 200 μm. The etching depth is amount to be ~ 300 nm. After that; AuGe (~ 150 nm) was evaporated and patterned using the lift-of technique to form the source, drain, and three potential-probe electrodes. Alloying was done at ~ 400 °C for 1 min in Ar ambient. The formation of good ohmic contacts and the device isolation were checked at this stage. Finally, Au (~ 70 nm) was deposited to form Schottky gate electrodes, which were also patterned by the lift-off method. Besides a main gate G which covers the whole channel, we formed five probe gates g_{1-5} lying on each mesa branch to the ohmic contact as shown in Fig. 4.2. By applying a threshold bias $V_{th(top)}$ on these small gates g_{1-5}, at which only the top 2DEG is depleted, one can isolate the top 2DEG under the main gate G from all the ohmic contacts including the drain and the source, while the gate G is used to control the electron densities and energy levels in the DQW channel.

To confirm the performance of the probe gates, we measured the two-terminal resistance R_{DS} between the drain and the source at low temperatures 1.5 $\sim$ 2 K by a low-frequency (15 Hz) ac lock-in technique as a function of the probe-gate voltage V_{g2}. Figure 4.3 shows typical data, the result for the sample 4B. In this measurement, the other ohmic contacts were opened, and the other gates G and $g_{1,3-5}$ were earthed. Note that the DQW systems at zero-bias are laid under the off-resonant condition due to the asym-
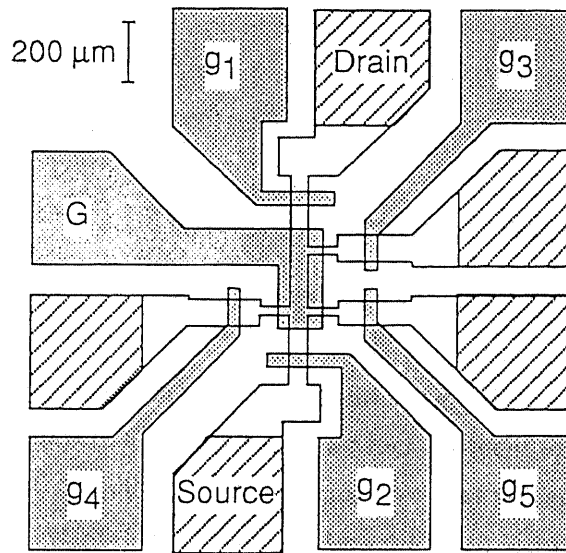
Figure 4.2: Top-view of the device layout is schematically shown. Shaded area indicates the Schottky metal, and hatched area the AuGe ohmic contact pads, respectively.
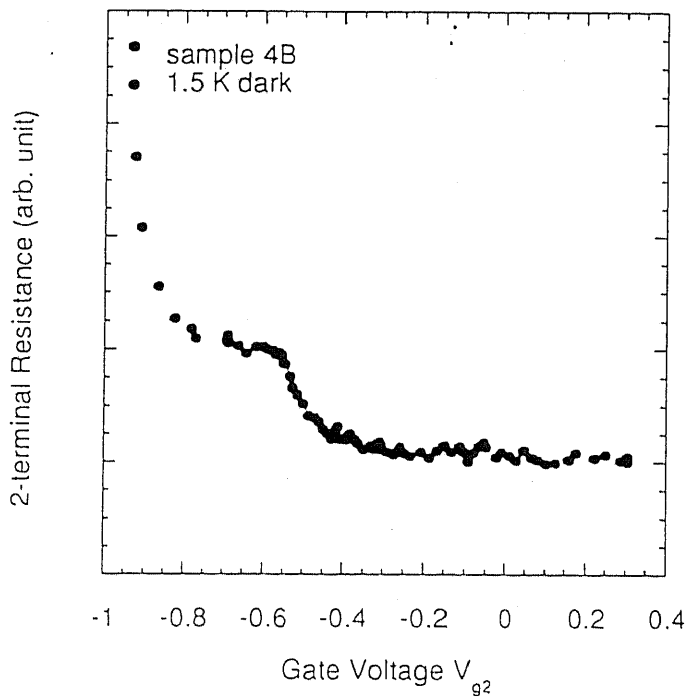

Figure 4.3: The drain-source resistance as a function of V_{g2} for the sample 4B. The other ohmic contacts were opened, and the other gates G and $g_{1,3-5}$ are earthed.

metric doping profile. As shown in Fig. 4.3, the R_{DS} *vs* V_{g2} curve has a step-structure at $V_{g2} \sim -0.6$ V, at which the top 2DEG under the gate electrode is fully depleted. The abruptness of the step-increase strongly depends on the barrier height and thickness. Indeed, the step-shaped structure was not observed in the R_{DS} *vs* V_{g1} or V_{g2} characteristics for the sample 4A, indicating that the 5 nm-thick AlGaAs barrier is not effective to separate two 2DEG's electrically even off-resonance.

4.2.2   Characterization of Tunnel-Dependent Conductivity

Next, we investigate the effects of the isolation of the top 2DEG from the ohmic contacts by conventional Hall measurements. We measured the channel resistivity ρ_{xx} at zero-magnetic field and the Hall resistance ρ_{xy} with a low magnetic field $B = 0.3$ T applied perpendicular to the 2DEG layers at 1.5 K by an ac lock-in technique supplying a 15 Hz small excitation current of 10 or 100 nA. By changing the bias voltage on five probe gates g_{1-5} from zero to $V_{th}^{(top)}$, we tested the samples in two different situations; namely, in one case, which we call "parallel-connection case" or simply "parallel" case, the top 2DEG is connected to the bottom 2DEG in parallel through ohmic contacts. In the other case, which we call "floating" case, the top 2DEG is isolated from all the ohmic contacts by depleting the top 2DEG beneath g_{1-5} on all the side arms.

Figures 4.4–4.7 show zero-field ρ_{xx} and ρ_{xy} at $B = 0.3$ T for the sample 4A-4D as functions of V_G. In these figures, the data for the "parallel" case are plotted by dotted lines, and those for the "floating" case by solid lines, respectively. For the sample 4A, as shown in Fig 4.4, there is no difference in ρ_{xx} and ρ_{xy} between the "parallel" and "floating" cases. This indicates, as described above, that for the sample 4A the two QW's are electrically connected in parallel through the thin barrier in the whole range of V_G.

In contrast, for the other samples with smaller tunneling energy gap ΔE_{SAS}, the data of the "floating" case exhibit the resonance features in their V_G dependence. Figure 4.5 displays ρ_{xx} and ρ_{xy} for the sample 4B in the same manner as Fig. 4.4. In "parallel" case, ρ_{xy} show monotonous increase as V_G is decreased from 0.5 V to -0.4 V. This is due to the depletion of the 2DEG in the top QW. When V_G is decreased further below -0.5 V, ρ_{xx} and ρ_{xy} increases very rapidly. This is due to the depletion of the 2DEG in the bottom QW. Note that ρ_{xx} slightly decreases when V_G reaches close to $V_{th}^{(top)}$ as indicated by an arrow in Fig. 4.5, which will be discussed later. In "floating" configuration, both ρ_{xx} and ρ_{xy} show pronounced dip structures centered at $V_G = -0.1$ V. The deviation of the resistances from those in "parallel" configuration is due to the isolation of the top 2DEG from the ohmic contacts. The current flows primarily in the bottom QW in "floating" configuration. However, when the two levels in the DQW get close to each other, the
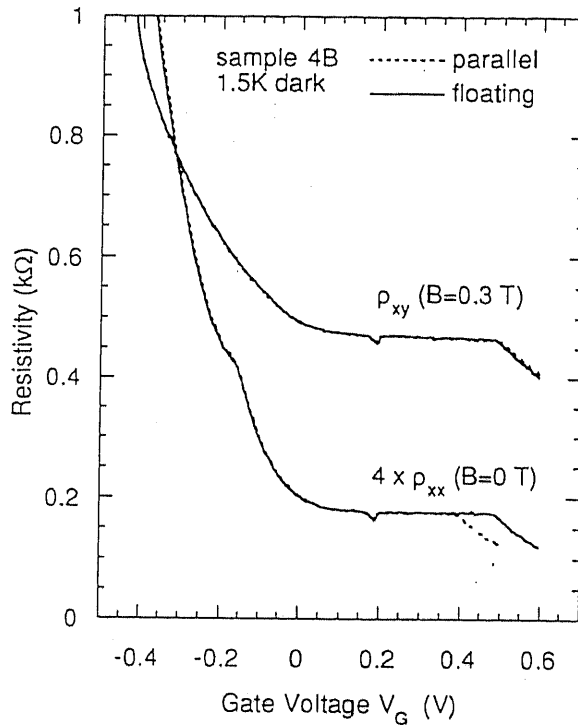
Figure 4.4: The channel resistivity ρ_{xx} and the Hall resistance ρ_{xy} at 0.3 T for sample 4A are plotted by dotted lines for the"parallel" case, and by solid lines for the "floating" case, respectively

Figure 4.5: The channel resistivity ρ_{xx} and the Hall resistance ρ_{xy} at 0.3 T for sample 4B are plotted by dotted lines for the "parallel" case, and by solid lines for the "floating" case, respectively
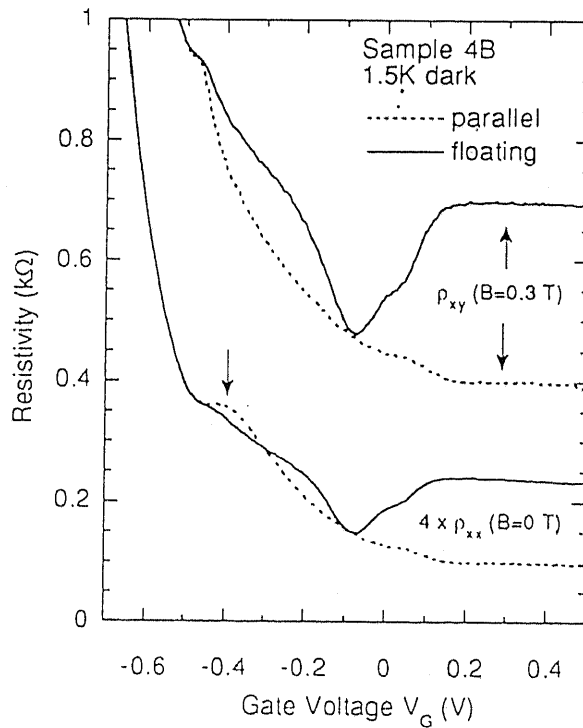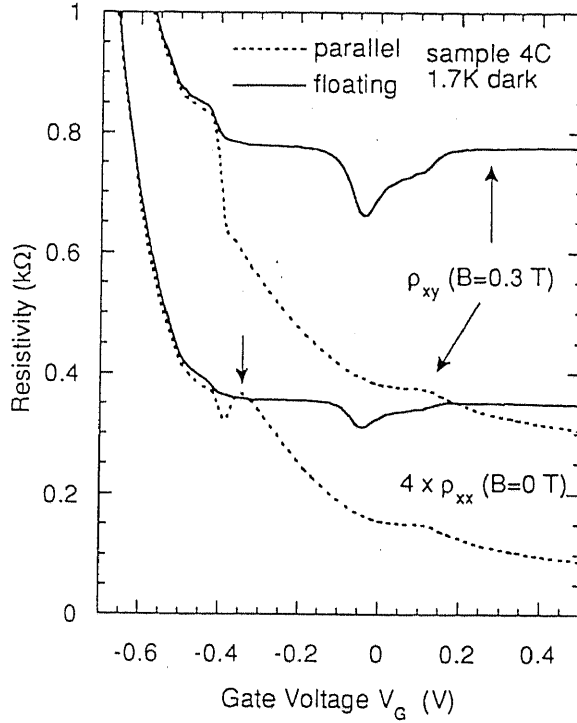
Figure 4.6: The channel resistivity ρ_{xx} and the Hall resistance ρ_{xy} at 0.3 T for sample 4C are plotted by dotted lines for the "parallel" case, and by solid lines for the "floating" case, respectively

inter-QW resonant tunneling of electrons is allowed to take place, and in consequence the tunnel resistance through the barrier is reduced. As a result, electrons in the top QW become to contribute to the channel conductance.

The width and the depth of the resistance dips, which represent the features of the tunnel conductance between two QW's, depend on such parameters as the barrier thickness and height, scattering rates in both QW's, and the area of the channel. For the sample 4B, as shown in Fig. 4.5, both ρ_{xx} and ρ_{xy} of the "floating" case become almost equal to those of the "parallel" case at $V_G \sim -0.1$ V, indicating that the tunnel resistance is negligibly small at resonance. For the other samples 4C and 4D, as shown in Figs. 4.6 and 4.7, the resistance dips are visible for the "floating" cases but become smaller with decreasing ΔE_{SAS}. The main contribution to the tunneling conductance between two QW's arises from the interlayer electron-electron scattering, which depends sensitively on the scattering rates in both QW's as well as the tunnel coupling strength. [102] In Fig. 4.8, we plot the effective electron mobility μ_{eff} and electron density n_{eff} for the samples 4A-4D. They are defined as $n_{eff} = e/B\rho_{xy}$ and $\mu_{eff} = \rho_{xy}/B\rho_{xx}$, respectively. Because of the inferior mobility of the bottom 2DEG for the sample 4A, we can not compare the data of the sample 4A with those of the others with respect to the relation between the
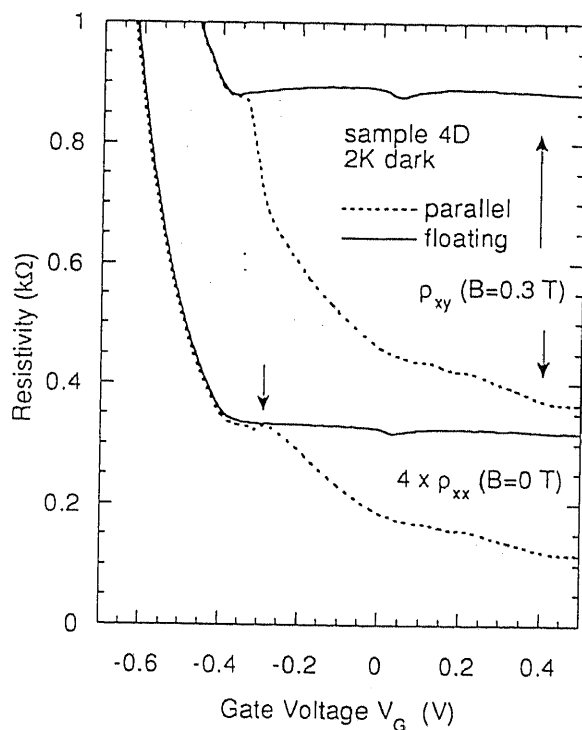
Figure 4.7: The channel resistivity ρ_{xx} and the Hall resistance ρ_{xy} at 0.3 T for sample 4D are plotted by dotted lines for the "parallel" case, and by solid lines for the "floating" case, respectively
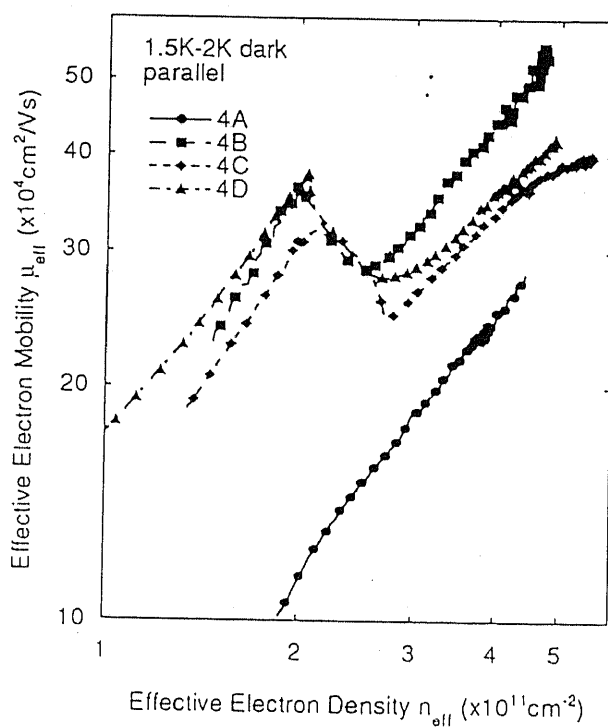

Figure 4.8: The effective electron mobility μ_{eff} is plotted as functions of the effective electron density n_{eff}.

tunnel-coupling strength and the resistance dips in the "floating" cases. For the samples 4B−4D, the electron densities and the mobilities in both QW's can be regarded as almost the same. The electron density n_{bottom} at saturation in the bottom QW is $\sim 2 \times 10^{11}$ cm^{-2} and the mobility μ_{bottom} is 300,000 $\sim$ 400,000 cm^2/Vs, which are determined by ρ_{xx} and ρ_{xy} at $V_{\text{G}} \sim V_{\text{th}}^{(\text{top})}$. At resonance, the total electron density n_{total} is twice as many as n_{bottom}, and the mobility μ_{top} of the top 2DEG is estimated to be 400,000 $\sim$ 500,000 cm^2/Vs. From these values of μ_i, we estimated the width of the broadened energy levels defined as $\delta E = \hbar\tau_{\text{tr}}^{-1} = \hbar e/m^*\mu$, and found $\delta E = 0.035 \sim 0.058$ meV, where $\hbar$ is the reduced Plank constant, and m^* the effective mass of an electron. Compared with ΔE_{SAS}, δE is found to be larger than ΔE_{SAS} by a factor of 2 for sample 4B, and ~ 100 for sample 4C and 4D. Indeed, the thermal energy $T = 0.13$ meV (1.5 K), at which the measurements were performed, is much higher than those energies. From these facts, we deduce that the observed resonance features are not due to the coherent tunneling but the sequential (incoherent) tunneling. For sample 4A, in contrast, $\delta E < \Delta E_{\text{SAS}}$ though μ_i are worse, resulting in a possible coherent tunneling which may lead to quite a large tunnel conductance. We do not go further on quantitative discussions of the tunneling conductance, for which a calculation based on the Kubo-formula is required. [48, 102]

4.2.3 Exchange Effect and Path of Charge Transfer

It is noticed that in Fig. 4.5− 4.7 that the channel resistivity ρ_{xx} in "parallel" configuration does not decrease monotonously when V_{G} is increased: As the top QW get close to depletion with decreasing V_{G}, ρ_{xx} once decreases or stops increasing, and increases again when V_{G} is decreased further (indicated by arrows). It has been also reported by another group that such a resistance peak appears near the threshold gate voltage for the top QW ($V_{\text{th}}^{(\text{top})}$) in a DQW similar to our sample 4D. [83] This is considered to be attributed to the charge transfer from the top QW to the other which is caused by the exchange-driven instability. [82, 83]

Finally, we consider the path of the charge transfer into or out of the top QW in "floating" configuration, in which the present device can be regarded as a kind of floating-gate devices in principle. [116] In a series of the present experiments, we first applied $V_{\text{th}}^{(\text{top})}$ on the probe gates, set V_{G} at a starting positive bias, and then started a scan. One scan of V_{G} (typically from +0.5 V to −1.0 V) took about 5 ∼ 7 min. In this operation, we did not see any substantial shift of the threshold voltage after a scan of V_{G}. Therefore, the time scale in the present experiments seems to be sufficiently long compared with the time constant of the system in the "floating" configuration, so that the number of electrons in the isolated top QW can follow V_{G}. In sample 4B, in which the tunnel coupling is not so

weak, the tunneling may contribute to the charge transfer between QW's. In the case of weak coupling limit as in sample 4C and 4D, we speculate that the electrons in the top QW will be carried in a leak current through the depleted probe gate (g_1 and g_2) regions.

4.3 Resonant Coupling in the Quantum Hall Regime

In sample 4B, ρ_{xx} or ρ_{xy} *vs.* V_G characteristics for the "floating" case reflect the features of the gate-controlled tunnel-coupling between two 2DEG's, as shown in Fig. 4.5. When a strong magnetic field B is applied, however, the situation changes due to the Landau quantization of the in-plane kinetic energies of electrons. It results in the formation of discrete magnetic levels which line-up with an even energy gap $\hbar\omega_c \equiv eB/m^*$ for each 2DEG.

Now consider the lateral electron transport in an asymmetric DQW in "parallel" configuration when B brings the system into the integer quantum Hall regime. Usually, a hybrid oscillation of the magnetoresistance R_{xx} remains the features of that of the individual 2DEG. In the power spectrum of the Fourier-transformed $R_{xx}(B^{-1})$ oscillation, one can find the electron density of a particular 2DEG independently. The Hall resistance R_{xy} is rather complicated. It is often the case that an oscillatory feature appears in $R_{xy}(B)$. The plateau of the quantized R_{xy} must not become $h/(\nu_{\text{top}} + \nu_{\text{bottom}})e^2$, $\nu_{\text{top}}, \nu_{\text{bottom}} = 1, 2, \cdots$, where h is the Plank constant, and ν_{top} (ν_{bottom}) the filling factor for the top (bottom) 2DEG, respectively.

At resonance, however, the Landau levels in both QW's should remain aligned since $n_{\text{top}} = n_{\text{bottom}}$. In "parallel" transport measurements, therefore, R_{xy} should be simply given by a half of that of a single 2DEG. For R_{xx}, the magnitude of the Shubnikov-de-Haas oscillation is unknown but the oscillatory features remain the same as those of a single 2DEG as long as the mobilities are not so different.

In this section, we investigate the effects of the isolation of the top 2DEG on the tunnel-coupled magnetotransport properties in a balanced DQW, i.e. at "zero-field" resonance.

4.3.1 Twofold Hall Resistance at Plateaus in the "Floating" Configuration

We made magnetotransport measurements employing sample 4B and setting V_G at the resonance bias -0.1 V. In Fig. 4.9, the Hall resistance R_{xy} of the "parallel" case is plotted by a dotted line, and that of the "floating" case by a solid line, respectively. Also in Fig. 4.10 the magnetoresistance R_{xx} of the "parallel" case is indicated by a dotted line,
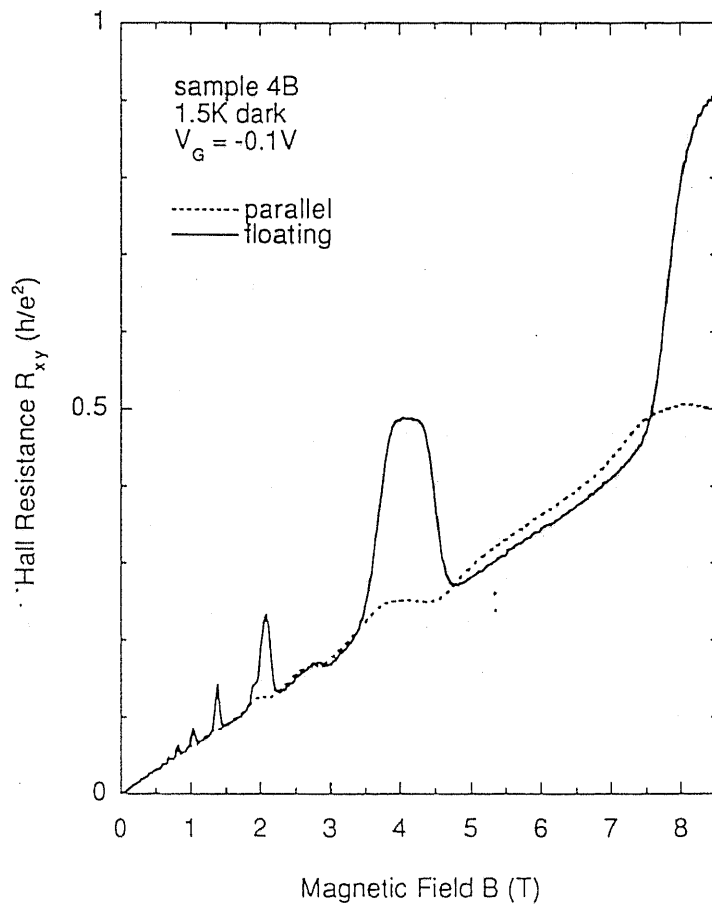
Figure 4.9: Hall resistance R_{xy} at $V_G = -0.1$ V (resonance) are plotted as functions of a magnetic field B for "floating" (a solid line) and "parallel" (a dotted line) cases.

and that of the "floating" case by a solid line. In Fig. 4.9, R_{xy} in "parallel" configuration shows clear plateaus at $h/\nu_{total}e^2$, when the filling factor ν_{total} is an even integer $2, 4, 6, \cdots$. Note that we define $\nu_{total} \equiv n_{total}h/eB$, each QW having a half of ν_{total}. In Fig. 4.10, R_{xx} of the "parallel" case becomes vanishingly small at $\nu_{total} = 2, 4, 8, \cdots$. Since ΔE_{SAS} is much smaller than δE, no Hall plateau was observed when ν_{total} is odd integers. From these data, we confirm that the two levels in the DQW structure are on resonance at $V_G = -0.1$ V, where R_{xx} (R_{xy}) for both "parallel" and "floating" cases in lower magnetic fields become almost identical.

In the "floating" case, the Hall resistance R_{xy} shows an abrupt increase each time it reaches a quantized Hall plateau as shown in Fig. 4.9. The height of R_{xy} at each peak is almost twice as high as that of "parallel" configuration, i.e. almost equal to that of the bottom 2DEG alone. This behavior suggests that the inter-QW resonant tunneling of electrons is considerably suppressed in the regions of integer quantum Hall effects, [46] since the contribution of the top 2DEG to the resistivities appears to vanish.

Based on a bulk-picture of Landau levels [14], one of the simplest explanations is given as follows. Figure 4.11 schematically shows the energy spectrum and the density of states for the aligned Landau levels. The light-shaded area indicates the region of localized states, from which the extended states at the center of Landau levels are separated by the mobility edges. When the Fermi energy E_F lies in middle region of the Landau level (Fig. 4.11(a)), where R_{xy} increases with B, electrons will be in the extended states in the 2DEG plane. In this case, the resonant tunneling of electrons can take place between the two QW's, just as in the case of low magnetic fields. Thus, both 2DEG channels can contribute to the conduction, resulting in the coincidence of R_{xy} between the "parallel" and "floating" cases.

On the other hand, when E_F is in the localized states (Fig. 4.11(b)), the extended states below E_F are fully occupied and the tunnel transition of electrons perpendicular to the QW plane is prohibited. For the localized states, there is no evidence that the tunnel-transfer is prohibited. However, the density of states $N(E)$ at E_F might be strongly reduced, which leads the localization of electrons both in the in-plane direction and in the direction perpendicular to the layers, [117] and the appearance of the Hall resistance of only the bottom 2DEG in consequence.

The oscillatory feature of R_{xy} starts to appear from considerably low magnetic fields ($B \sim 0.5$ T). However, the peak of R_{xy} in lower B are not twice as high as that of the "parallel" case, indicating that the tunneling is not completely suppressed. It is also found in Fig. 4.9 that a change of R_{xy} occur only when ν_{top} and ν_{bottom} are even integers and 1, where R_{xx} for only the bottom 2DEG vanishes. This suggests that the energy
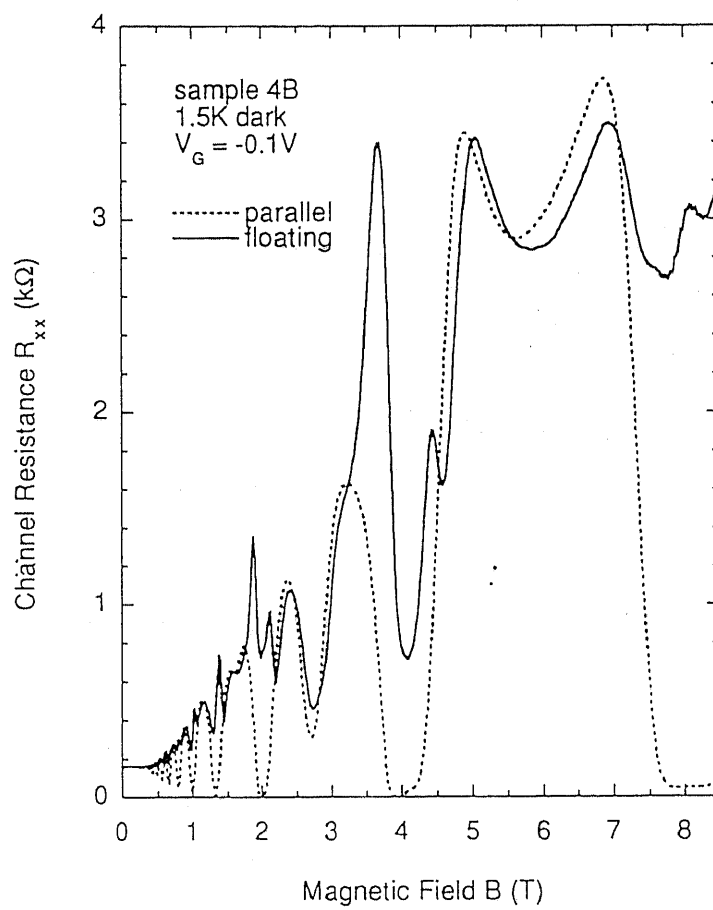
Figure 4.10: Magnetoresistance R_{xx} at $V_G = -0.1$ V (resonance) are plotted as functions of a magnetic field B for "floating" (a solid line) and "parallel" (a dotted line) cases.
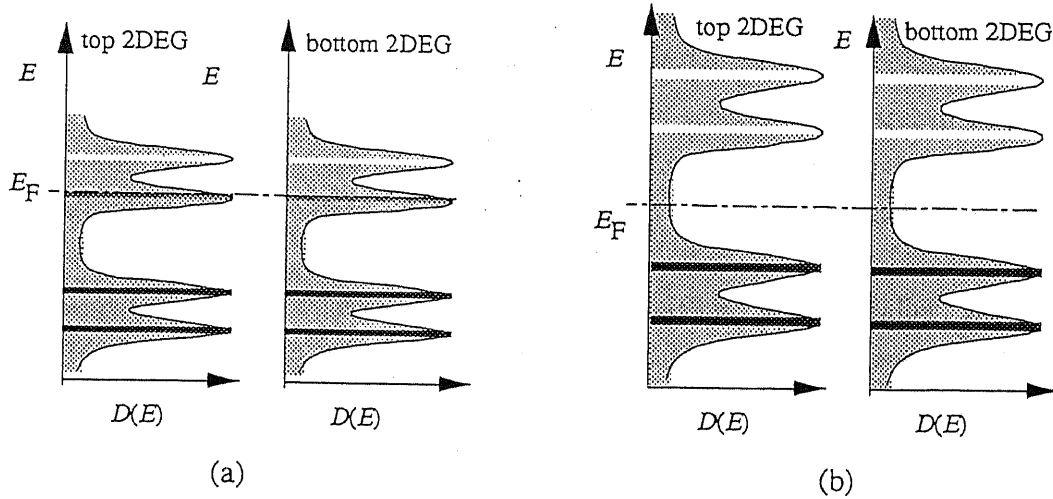
Figure 4.11: Schematic illustrations of energy spectrum for the Landau levels. (a) The Fermi energy E_F lies in the extended states, and (b) E at the localized states (integer quantum Hall regime).

gap corresponding to the Zeeman splitting is not large enough compared with the level broadening when ν_{top} or $\nu_{bottom} > 2$.

4.3.2   Non-Vanishing Magnetoresistance in "Floating" Configuration

Next, we study R_{xx} data in Fig. 4.10 in detail. The behavior of R_{xx} under the "floating" condition looks more complicated. First of all, R_{xx} does not vanish even when ν_{top} (ν_{bottom}) is 1 or an even integer, where that of the "parallel" configuration vanishes at all. Moreover, distinct R_{xx} peaks appear on both sides of R_{xx} minima. The non-zero R_{xx} in the integer quantum Hall regime strongly suggests that there exists a path across the bottom 2DEG channel through which electrons are to be scattered backward. Providing that in the medium both the top and the bottom 2DEG's are incompressible [118] and thus inter-QW tunneling is strongly suppressed, [46] the origin of the finite channel resistivity R_{xx}, i.e. the non-zero conductivity σ_{xx}, should be attributed to the tunnel-interaction between edge channels in each QW. The appearance of additional R_{xx} peaks implies that backward scattering is substantially enhanced in the transition regions where R_{xy} of the "floating" case (a solid line in Fig. 4.9) shows a sudden deviation from that of the "parallel" mode (a dotted line).

4.3.3   Results in Other Configurations

To clarify the origin of the peculiar behaviors of the magnetoresistance observed in the "floating" configuration, we have investigated the effect of each probe gate g_{1-5} by studying R_{xx} and R_{xy} in other possible configurations as schematically shown in Fig. 4.12(a) (also see Fig. 4.2). Since we mainly argue the magnetotransport properties of the quantum Hall effect, the situation of the DQW in each case was shown by an edge-channel picture as Fig. 4.12(a).

(i) and (vi) in Fig. 4.12 correspond to the "floating" and "parallel" modes, respectively. In the case of (ii), for instance, the top 2DEG is made in contact with the drain electrode by setting $V_{g_1} = 0$ V while the others are at $V_{th}^{(top)} = -0.6$ V. For each case, the magnetoresistance R_{xx} and the Hall resistance R_{xy} at resonance bias ($\nu_{top} = \nu_{bottom}$) were measured, and plotted in Fig. 4.12 (b) and (c), respectively. (Note that we used another sample 4B(2) in the following measurements, not the sample 4B studied previously. Of course they were formed on the same wafer and we confirmed that the essential characteristics related to the gate-controlled resonant tunneling were almost identical. However, the resonance gate voltage or the electron density at saturation were found to be slightly different. For sample 4B(2), zero-field resonance occurs at $V_G = -0.18$ V.)

In the case of (ii), the magnetotransport properties were quite similar to those of the completely "floating" case (i). Only the peaks of R_{xy} were slightly smeared by opening the channel between the drain and the top 2DEG beneath the tunnel gate G.

When the gate g_2 lying between the channel and the source was grounded as (iii), both R_{xx} and R_{xy} changed drastically in contrast to the case of (ii). As shown Fig. 4.12(b), the extra peaks of R_{xx}, which were observed in the cases of (i) ("floating") and (ii), were found to disappear, and the minima of R_{xx} get vanishingly small at $\nu_{bottom} = 1$ and even integers as is in the "parallel" case (vi). From these facts, we may deduce that the source gate g_2 plays a crucial role for the magnetoresistance. For R_{xy}, in contrast, each peak at integer ν_{bottom} were almost halved but the feature of it was well preserved when the top 2DEG is earthed to the source.

This conclusion is also supported by the results performed in the configuration of (iv), where all three voltage-probes were in contact with the top 2DEG in parallel to the bottom 2DEG, while the current flow was restricted to the bottom 2DEG, i.e. g_1 and g_2 were biased at -0.6 V. In this case, R_{xy} peaks were smeared out further than those in the case of (iii), but one can find a small but distinct peaks in the magnetoresistance at $B = 2.25$ T or 4.5 T.

In the case of (v), where only the voltage probes were isolated from the top 2DEG channel, the situation is almost the same as the "parallel" (vi) case since the current flows

(i) floating

(ii) drain-on

(iii) source-on

(iv)
drain·
source off
probes on

(v) drain·
source on

(vi) parallel

——— Bottom 2DEG
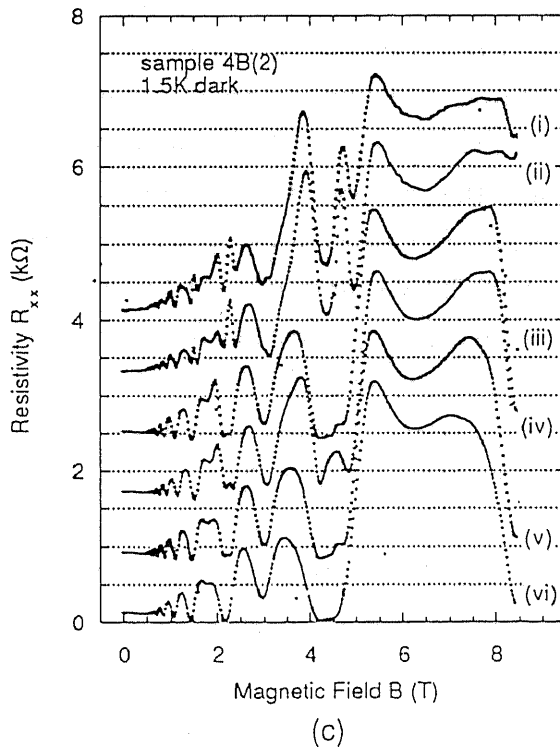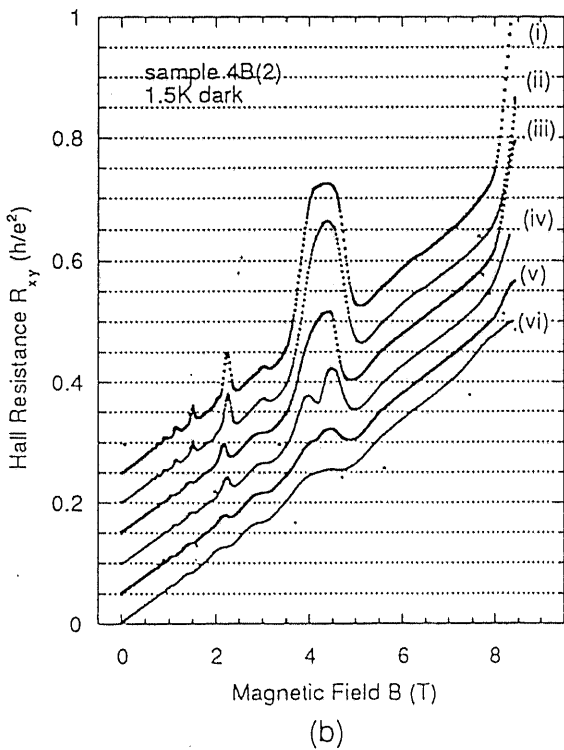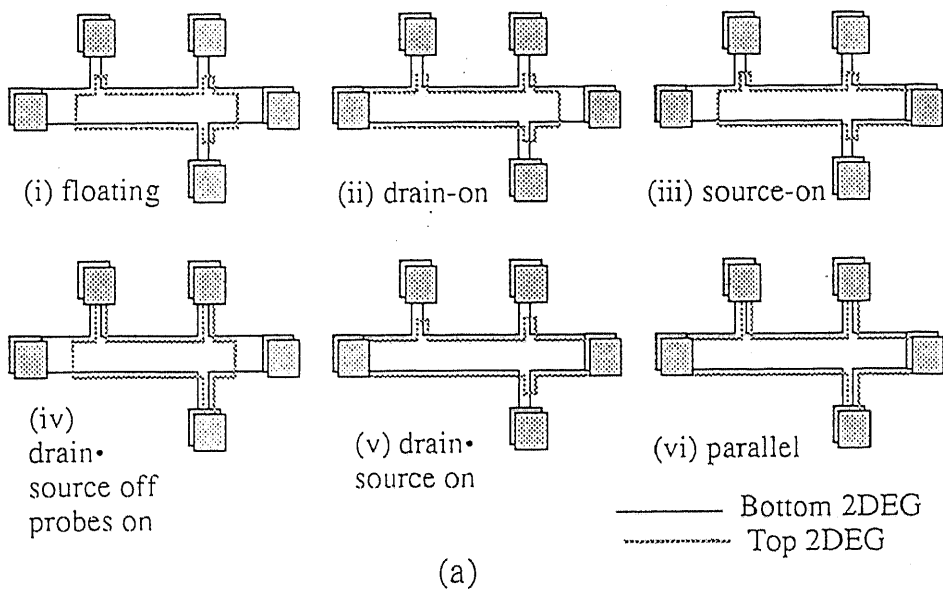············ Top 2DEG

(a)

(b)

(c)

Figure 4.12: (a) Schematic illustrations of tested configurations (i) ∼ (vi). Solid lines indicates the edge channels in the bottom QW, and hatched lines correspond to those in the top 2DEG, some of which are cut by g_1 ∼ g_5. (b) The configuration-dependence of R_{xy} and (c) R_{xx} at resonance bias.

equally in each QW as $n_{top} = n_{bottom}$ and $\mu_{top} \sim \mu_{bottom}$.

Summarizing these results shown in Fig. 4.12, depletion of the top 2DEG between the channel region and the source electrode should be essential for the cause of backward scattering in the integer quantum Hall regime, although the reason which is underlying these observations is unclear.

4.4 Discussions

4.4.1 Off-Resonant Tunneling in Floating Configuration

When V_G is changed from the resonance bias voltage, the zero-field inter-QW tunneling of electrons is suppressed because of the restriction that the energy and the in-plane momentum must be conserved. In a strong magnetic field applied perpendicular to the layers, however, electrons can indeed move from one QW to the other when the Landau levels of different indices become aligned at the Fermi energy. [50] Therefore, when the intrinsic tunnel-coupling of the DQW is as strong as in sample 4B, both R_{xx} and R_{xy} for the "floating" case are expected to be the same as those for the "parallel" case in a high magnetic field not only at the resonance gate voltage at which the DQW potential is balanced, except that the electrons at the Fermi energy are in the localized states.

For sample 4B(2), we carried out the magnetotransport measurement in both "parallel" and "floating" cases at various gate voltage V_G. In Fig. 4.13, we plot R_{xy} of the "floating" case for the gate voltage from $V_G = 0$ V to -0.35 V in each -0.025 V-step. In this range of V_G, the electron concentration n_{bottom} is unchanged: ν_{top} changes with V_G from 5.5 to 2.5 at 2.25 T where $\nu_{bottom} = 4$, for example. We also measured R_{xx} and R_{xy} for both configurations as functions of V_G at several points of fixed magnetic field. Figure 4.14 shows the data at $B =$ (a) 4.4 T, (b) 2.95 T, (c) 2.25 T, and (d) 1.99 T, respectively, as functions of V_G.

As V_G is changed from ~ -0.18 V, the width of the R_{xy} peak at $B \sim 4.4$ T becomes broad: The tail of it extends toward higher magnetic field when V_G is increased, and vice versa. This is evident from the fact that the position of the Hall plateau at $\nu_{top} = 2$ shifts with $V_G \propto n_{top}$ as $B = hn_{top}/e\nu_{top}$. Following this relation, however, the plateau for $\nu_{top} = 2$ will appear at $B \sim 6$ T when $V_G = 0$ V, and $B \sim 3$ T for $V_G = -0.35$ V, respectively. In the experimental data, the R_{xy} peak was not broadened so wide as expected. Moreover, a missing R_{xy} peak at $\nu_{bottom} = 3$ appeared at $B \sim 3$ T when V_G is changed sufficiently away from the zero-field resonance condition. This can be explained in a following manner: At ν_{bottom} or $\nu_{top} = 3$, the (Zeeman) energy gap between two spin-split Landau levels of $N = 2$ is so small that electronic states should extend to

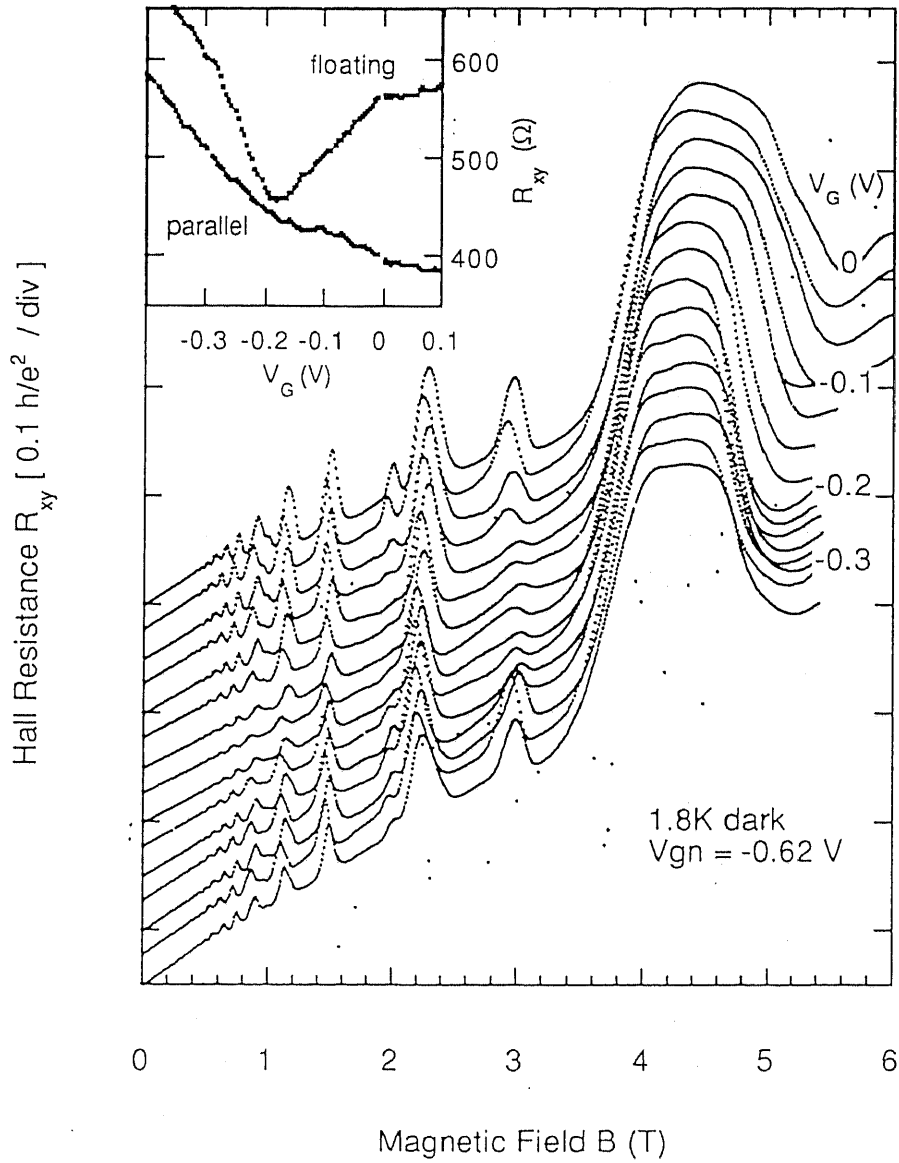Figure 4.13: The Hall resistance R_{xy} of sample 4B(2) for the gate voltages V_G from 0 V to -0.35 V in steps of -0.025 V measured in "floating" configuration are plotted as functions of a magnetic field B. The zero-field resonance occur at $V_G = -0.18$ V. Inset: The Hall resistance R_{xy} of sample 4B(2) at 0.3 T are plotted as functions of the gate voltage V_G for both "parallel" and "floating" cases.

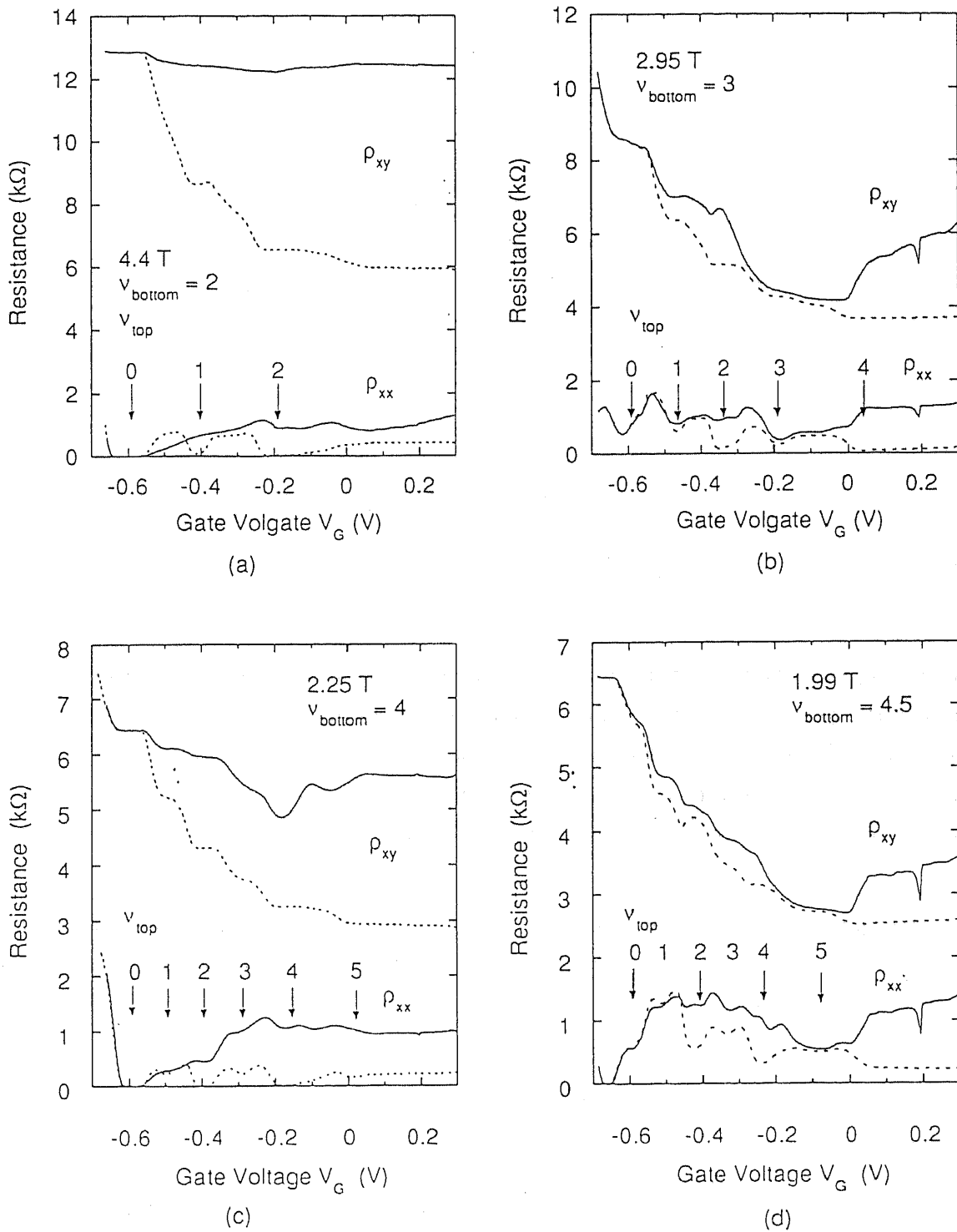Figure 4.14: The channel resistance R_{xx} and the Hall resistance R_{xy} at fixed magnetic field B are plotted as functions of the gate voltage V_G for both "parallel" (dotted lines) and "floating" (solid lines). The filling factor ν_{bottom} for the bottom QW corresponds to (a) 2 at 4.4 T, (b) 3 at 2.95 T, (c) 4 at 2.25 T, and 4.5 at 1.99 T. The ν_{top} is also denoted in each figure.

some extent, as R_{xx} of each 2DEG does not vanish. Under this situation, the inter-well tunneling between these states will be substantially allowed to take place widely in the channel, resulting a missing R_{xy} peak at zero-field resonance. As n_{top} is changed with V_G and ν_{top} becomes even integer at the same magnetic field, the tunneling will be effectively suppressed since the degree of localization is higher for $\nu_{top} =$ an even integer than 3.

The above argument is, however, not in favor of the former observation that the position of each R_{xy} peak is fixed at $B = hn_{bottom}/e\nu_{bottom}$ and is not dependent on ν_{top}. For the comprehensive understandings of these unique phenomena as well as the other peculiar ones observed in Figs. 4.13 and 4.14 but not referred here, further experiments and theoretical analysis are necessary.

4.4.2 Tilted Magnetic Field Dependence

Finally, we present a part of experimental results on magnetotransport properties in tilted magnetic fields.

As an in-plane magnetic field **B** is added, especially when **B** is directed perpendicular to the channel, the transport properties of tunnel-coupled 2DEG's are expected to be modified by **B**. As shown in Chapter 3, as well as in many articles, [44, 99] tunneling between 2DEG's should be suppressed by **B**. For the Landau magnetic levels, the additional in-plane component **B** will enhance the Zeeman energy gap due to the increase of total magnetic field.

Following these fundamental understandings, we expected that (i) tunneling between extended states would be suppressed, and (ii) missing R_{xy} peak at $\nu_{bottom} = \nu_{top} = 3$ might appear for the "floating" case when a magnetic field is tilted from the normal direction to the DQW layer.

As shown in Fig. 4.15, each peak in R_{xy} of "floating" configuration at $\nu_{bottom} =$ aneveninteger was found to be enhanced as tilted angle θ was increased. In particular, a prominent peak was observed at $\nu_{bottom} = 3$ when $\theta = 41°$, as expected. However, for $\nu_{bottom} =$ non-integer number, R_{xy} was unchanged with tilting B. This suggests that the selection rule which forces conservation of in-plane momentum $\hbar k$ becomes invalid because a high magnetic field B normal to the layers quenches the kinetic energy of electrons. One should notice that there is a contradiction between two conclusions. Establishment of a theoretical model as well as further experimental studies seem to be necessary to clarify the unique but complicated results.
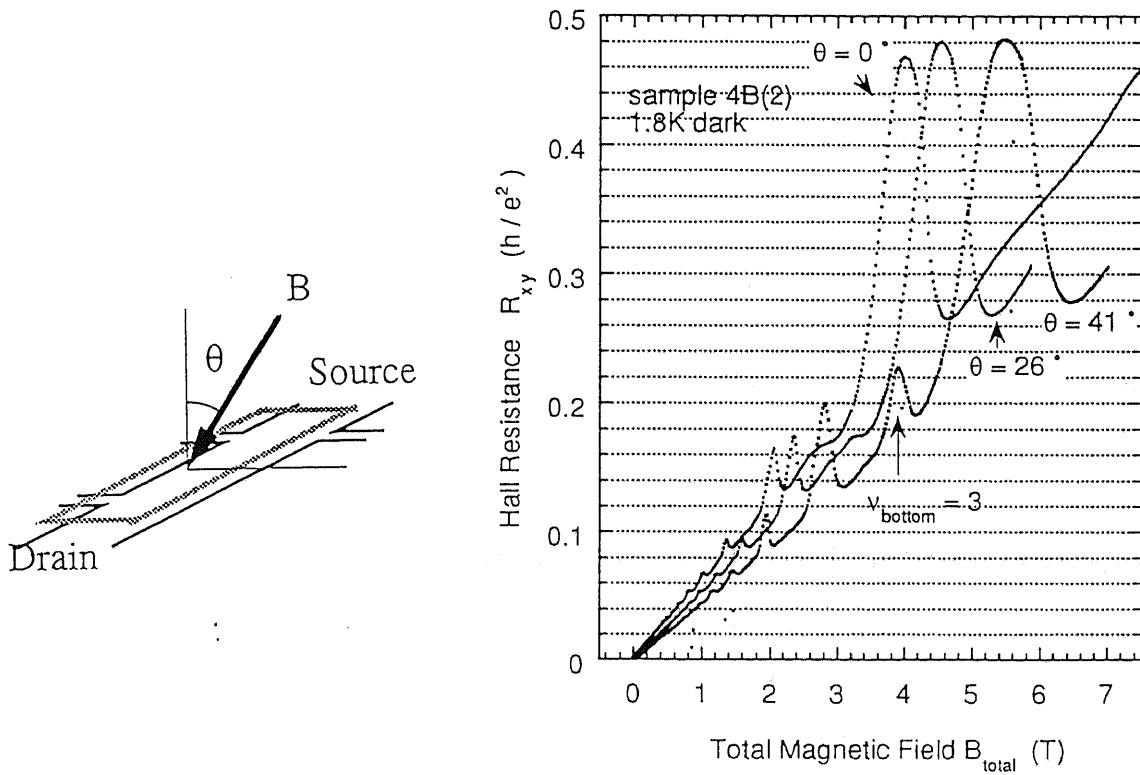
Figure 4.15: Left: Arrangement of the Hall measurements in tilted magnetic fields. Right: The Hall resistance R_{xy} for sample 4B(2) biased at zero-field resonance were measured in the "floating" configuration with the direction of the magnetic field tilted at $\theta = 0°, 26°$, and $41°$.
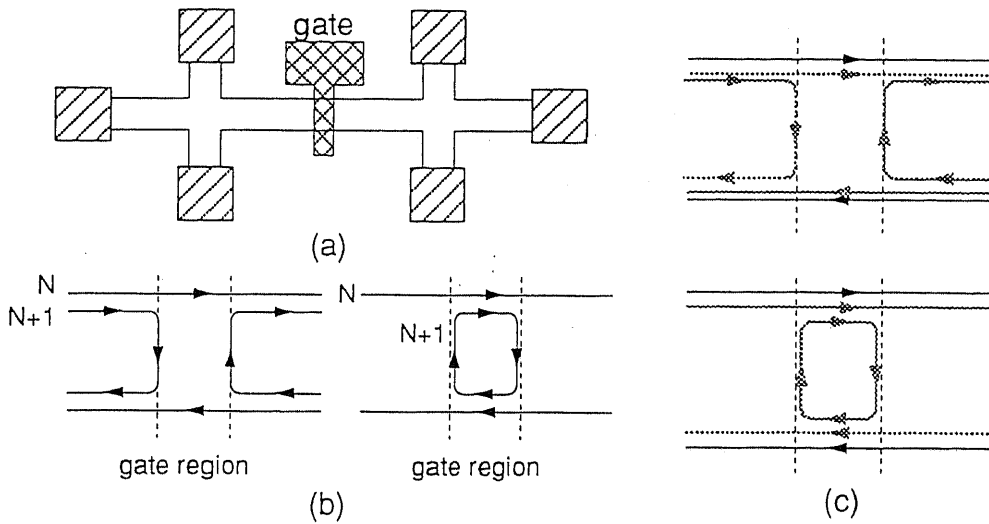
Figure 4.16: (a) Schematic of a Hall-bar geometry with a finger gate, and edge channels. After [124] (b) Schematic edge-channel pictures for the sample region with the cross gate. Left: A filling factor ν in the gate region is lower than in the outside. Right: ν is higher than in the outside, resulting in the formation of a closed loop of edge channels of larger indices N. (c) Schematic of edge-channel pictures for a double-layered system. Solid lines indicate the edge channels belonging to one QW, and hatched lines of the other. (Similar to Fig.4.12(a)).

4.4.3   Comparison with Experiments on Edge Channel Transport

After the observations of the integer quantum Hall effect (IQHE) [12] and the fractional quantum Hall effect (FQHE) [13] in two dimensional systems, the actual current distribution in the channel under a strong magnetic field has been of great interest. Recently, many people have become convinced of the validity of the "edge channel" picture for its successful explanation of FQHE [118,119] as well as IQHE [120]. It has been applied to many experiments in the quantum Hall regime [121], and has also been refined theoretically [122] and verified in special experiments. [123]

In a number of experiments concerning edge-channel transport, Hall-bar-geometry with a gate finger has been widely used. [124] Figure 4.16(a) shows a typical one, where by changing the electron concentration of the gate region locally, the Hall-bar channel will contain regions of different filling factors, short-cuts or closed loops of the edge channels with higher indices of the Landau levels, as depicted in Fig. 4.16(b). The central results obtained at these experiments are concerning the interactions between these edge channels. [124, 125] Analogous to these experiments in a single layer 2DEG, the configurations in the present work can be expressed as shown in Fig. 4.16(c), where the edge channels of the upper Landau levels are replaced by those in the different layer.

Although we could not accomplish full arguments of the present results in terms of

"edge channels", we expect that the extension of the study on edge-channel transport from the intra-layer to inter-layer interactions will provide further information as well as a variation of experiments because of the controllability of the structural parameters in the case of a DQW.

4.5 Summary

In this chapter, we have investigated the quantum Hall effect in tunnel-coupled two dimensional electron gases (2DEG's). Hall-bar-shaped field effect transistor (FET) structures were fabricated, in which current flow and voltage probes can be switched from "parallel" mode to "floating" mode by depleting only the top QW with a small gate formed on each mesa arm. In the latter case, only the bottom 2DEG is probed while the top 2DEG contribute to the in-plane conduction only through the inter-QW tunneling process. We studied magnetoresistance and Hall resistance in this configuration and found that the Hall resistance shows a sudden increase in each quantum Hall state, indicating that tunnel-coupling is suppressed (inter-layer localization) when the electrons are laterally localized (intra-layer localization).

Chapter 5

Double Quantum Wells with an In-plane Periodic Potential

5.1 Introduction

It has been predicted that several unique electronic properties will appear in superlattice (SL) structures [1], in which a periodic potential having a period comparable with the de Broglie wavelength of electrons (~ 10 nm) is artificially introduced.

For device applications, planar superlattice (PSL) structures consisting of coupled quantum wire (CQWI) or coupled quantum box (CQB) structures are preferred over multilayered SLs, since PSL's allow more distinct modulation of electronic states and also the gate-controlled modulation of carrier concentration. [17, 18] When these PSL systems are used as channels of field effect transistors, various novel functions are expected to be realized, such as a gate-controlled negative resistance [17] or a negative transconductance. [126]

Figure 5.1 shows examples of such PSL structures, and their energy dispersion relations $E(k)$, where k is an electron wave number. In PSL structures, the effective mass m^* of electrons (in the x-direction) can be varied by scanning the Fermi energy or the Fermi wavenumber k_F across the miniband. However, the variation of m^* with the gate voltage is rather gradual as one must scan the wavenumber across the wide range of the mini-Brillouin zone. In this chapter, we consider an alternative scheme to achieve the effective mass modulation specifically. We investigate theoretically a unique way to control the dispersion relation of electrons by using a novel double quantum well (DQW) structure, in which an in-plane periodic potential is introduced to one of the channels.

In the next section, it is demonstrated that the effective mass in this system can be abruptly changed by the gate-controlled resonant coupling, resulting in a switching of the channel.
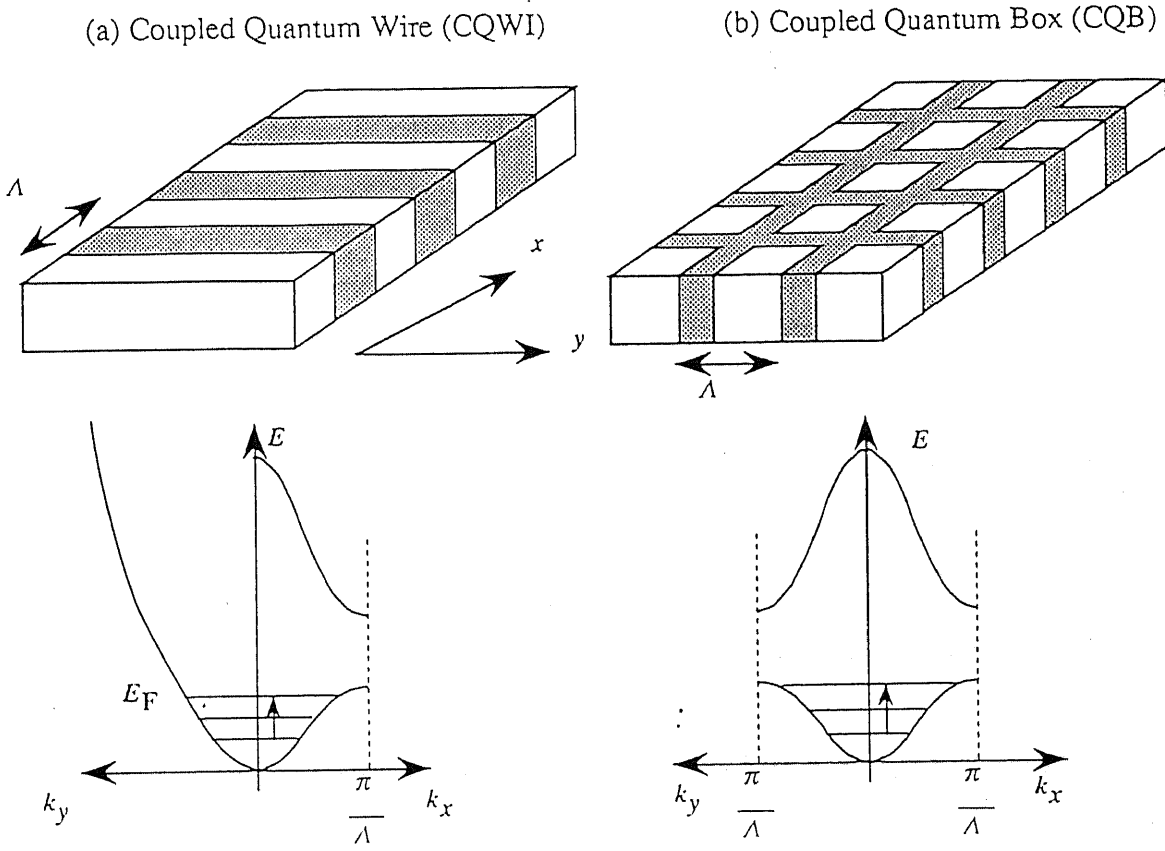
70

Figure 5.1: Schematic illustrations of planar superlattices: (a) coupled quantum wire (CQWI) and (b) coupled quantum box (CQB) structures, and energy dispersion relations in those systems.

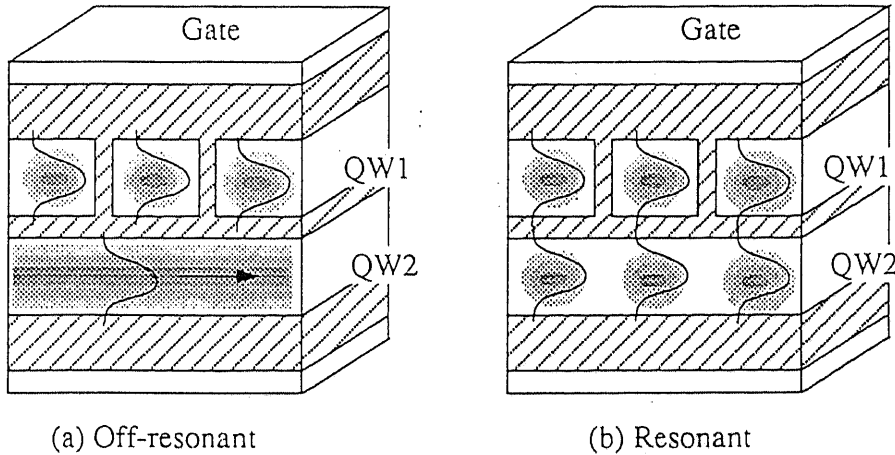(a) Off-resonant   (b) Resonant

Figure 5.2: Illustrations of the device structure and electronic states in it (a) under off-resonant and (b) resonant conditions, respectively

In the third section, we discuss a few feasible schemes to achieve the effective mass modulation and their possible applications to the velocity modulation transistor. [31]

5.2   Effective Mass Modulation by Gate-Controlled Resonant Coupling

5.2.1   Model and Principle

We consider a novel coupled two-dimensional electron system, which is schematically shown in Fig. 5.2. In that system, a periodic component of in-plane potential is introduced only in the upper quantum well (QW1), whereas the in-plane potential is flat in the lower QW (QW2). When there is no inter-well coupling in the system, electrons in the lower QW move freely in the channel, whereas electrons in the upper QW will be strongly influenced by the periodic potential (see Fig. 5.2(a)). In particular, all electrons will be localized at each potential minimum and the channel becomes insulating when the miniband is completely filled with electrons.

Although electrons in the lower QW are usually unaffected by the periodic potential of the upper QW, they can interact with the in-plane potential if the two QWs are brought into the resonance (see Fig. 5.2(b)). In such a case, the in-plane dispersion $E(k_x)$ of
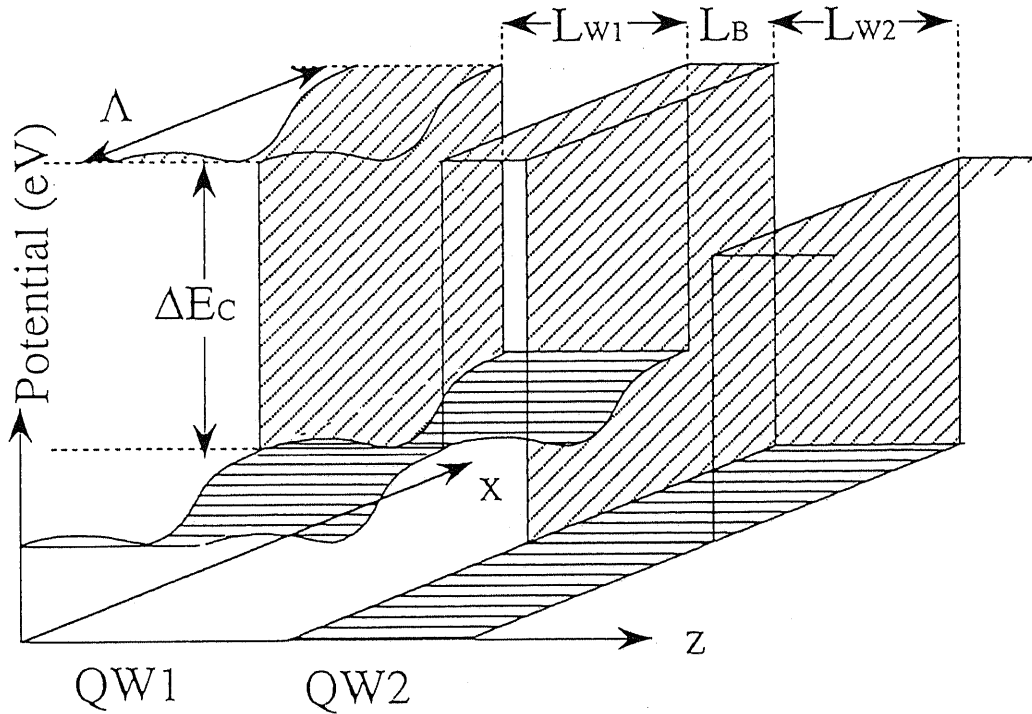
Figure 5.3: A schematic illustration of a model of the potential $V(x, z)$ used in the calculations

electrons will be resonantly modulated, and as a result the effective mass m^* will be controlled by the gate voltage V_g.

5.2.2 Calculation of Energy Dispersion

To examine the present concept, we have calculated the dispersion relations in a number of possible structures. For the calculation, we consider a GaAs / AlGaAs double quantum well (DQW). The profile of a model potential is shown in Fig. 5.3 in x-z plane. It consists of a pair of 12 nm-wide GaAs quantum wells with a 1.5 nm-thick AlGaAs barrier in between. The conduction band discontinuity between GaAs and AlGaAs is set to be 0.3 eV. The origin of the energy is set at the conduction band edge of the lower (flat) channel.

The band edge of the upper QW along the x-axis is expressed as

$$V(x) = V_0 + V_1 f(2\pi x/\Lambda) \tag{5.1}$$

which consists of a constant value V_0 and a periodic component $V_1 f(2\pi x/\Lambda)$ with the period of Λ. Note that V_0 can be changed by the gate voltage V_g. To find the dispersion relations $E_i(k_x)$ and their V_0 dependence, we solve the two-dimensional Schrödinger

equation

$$\{-\frac{\hbar^2}{2m^*}(\frac{\partial^2}{\partial x^2} + \frac{\partial^2}{\partial y^2}) + V(x,z)\}\psi_{k_x}(x,z)e^{ik_x x} = E(k_x)\psi_{k_x}(x,z)e^{ik_x x} \qquad (5.2)$$

by a finite element method.

For simplicity, we assumed that the effective mass $m^* = 0.067m_0$ in both GaAs and AlGaAs, where m_0 is the mass of a free electron.

First, we consider a case where the potential $V(x)$ within the upper QW is in the form of $V_0 + V_1 \cos 2\pi x/\Lambda$. The energies $E_i(k_x = 0)$ and $E_i(k_x = 0)$ of the bottoms of the lowest two subbands are calculated for $V_1 = 25$ meV and $\Lambda = 20$ nm, and plotted as functions of V_0 by solid lines in Fig. 5.4. As V_0 increases from zero to 20 meV, the energy of the electronic state residing mainly the upper QW increases almost linearly and crosses with the electron state coming originally from the lower QW. Figure 5.4 shows clearly this crossing at $V_0 = 5$ meV, where the energy difference $\Delta E = E_2 - E_1$ reaches its minimum ($\Delta E \sim 5$ meV), leading to the resonant coupling. Note in the present case that this coupling takes place only at a particular value of k_x ($k_x = 0$ in this case). All other states with different k_x are still uncoupled since the original dispersion relation of electrons in the upper QW and that of the lower QW are not parallel each other, as will be discussed below.

Next, we show in Fig. 5.5 the energy dispersion relations $E(k_x)$ for the three lowest minibands as functions of k_x. Solid lines are the results for $V_0 = 25$ meV, while broken and dotted lines are the dispersion relations for $V_0 = 30$ meV and 15 meV, respectively. Note in solid curves that the zone-folded parabolic branch, which corresponds to electronic state in the lower QW, cross with a flat branch, which represents a states of the upper QW at $E(k_x \sim 1.2 \times 10^6 \text{ cm}^{-1}) \sim 45$ meV, resulting in a clear minigap at the anti-crossing point. In such an energy range, both electronic states extend over both QW's and interact with the periodic potential, leading to the localization of electronic motions along the channel direction. (Note also that the energy value of anti-crossing moves upward or downward as the magnitude of V_0 increases to 30 meV or decrease to 15 meV.)

Secondary, we consider a system where the periodic potential is expressed by a step function $\theta(x)$ with 15 nm-wide GaAs QWs and 5 nm-thick AlGaAs barrier as shown in Fig. 5.6. The dispersion of electrons in the upper QW is almost flat, because of the strong lateral confinement along the x-direction. The (anti-)crossing of a zone-folded parabola and a flat dispersion takes place as shown in Fig. 5.6, leading to the appearance of clear minigaps for three values of $V_0 = 0$, -5, and -10 meV. Note that the gap is seen in the first minizone when $V_0 = -10$ meV, which was not possible when the confinement potential is weak as in the case of Fig. 5.5.
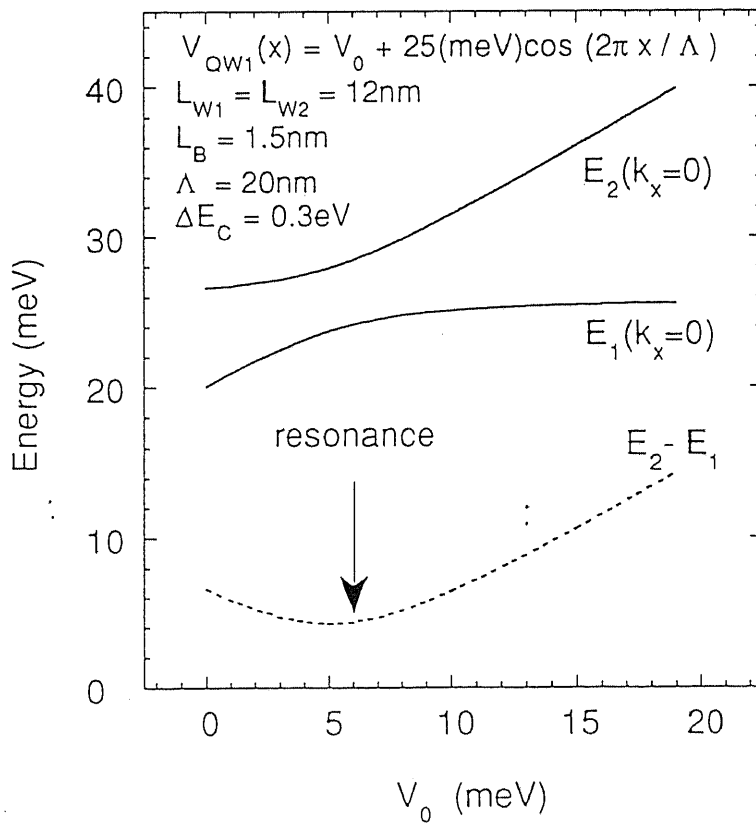
Figure 5.4: Calculated energy levels E_1 and E_2 at wavenumber $k_x = 0$ are plotted as functions of a parameter V_0 by solid lines. A dotted line indicates the energy difference $\Delta E = E_2 - E_1$. The structural parameters and the in-plane periodic potential in the top quantum well are listed in the top.

Figure 5.5: Calculated energy dispersions $E_i(k_x)$ at $V_0 = 15, 25$, and 30 meV are plotted as function of k_x. The parameters used in the calculations are the same as those listed in Fig. 5.4.

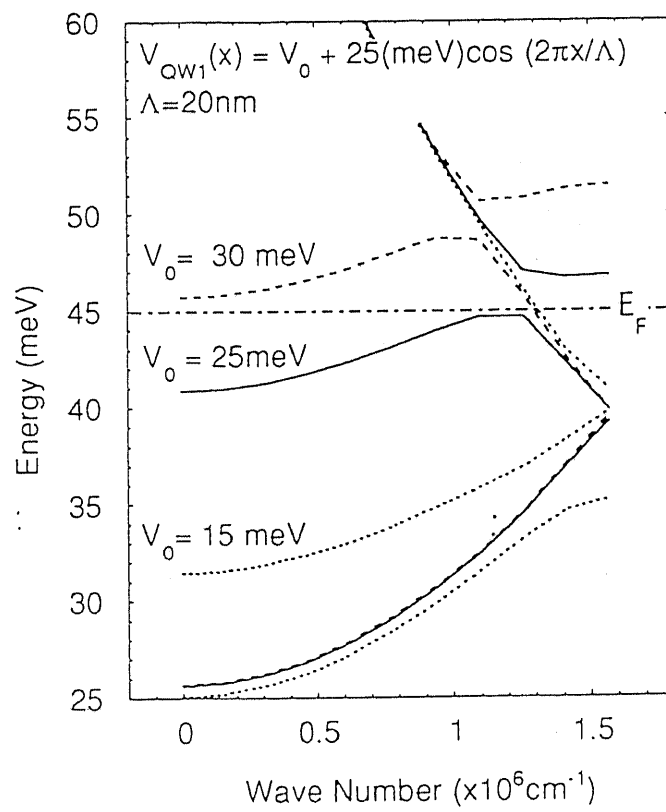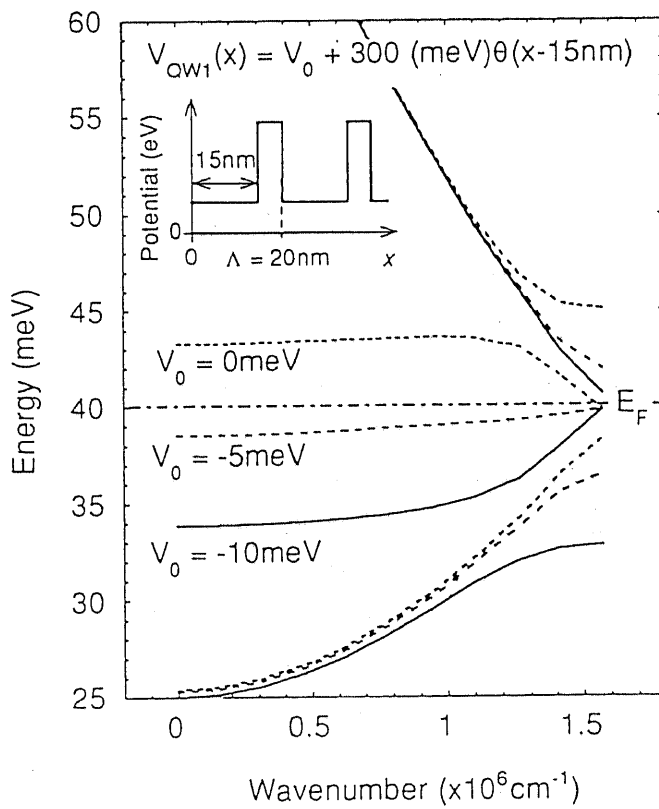Figure 5.6: Calculated energy dispersions $E_i(k_x)$ at $V_0 = -10$, -5, and 0 meV are plotted as functions of k_x. The structural parameters used in the calculations are the same as those in Figs. 5.4 and 5.5 except for the in-plane periodic potential function, which is shown by a schematic illustration in the top.

Now let us examine how one can modulate the effective mass m^* of electrons by the gate voltage V_g. Suppose that the Fermi energy E_F is initially set just above the top of the second miniband. Specifically, we assume that $E_F = 45$ meV and $V_0 = 25$ meV in Fig. 5.5, and that $E_F = 40$ meV and $V_0 = -5$ meV in Fig. 5.6, respectively. In such cases, m^* is infinity and the conductivity should be zero. If one reduces V_g, i.e. increases V_0 slightly to reduce both E_F and the electron concentration, then E_F starts to fall in the parabolic region of the band, where m^* is finite. Then the group velocity of electrons at E_F abruptly increase and the conductivity recovers. Thus a novel switching operation with negative transconductance g_m or a kind of mobility modulation effects is expected to be realized.

5.2.3 Discussion

The gate-controlled mobility modulation has been experimentally realized by resonant deformation of wavefunctions in GaAs / AlGaAs DQW structures, in which a random potential is introduced in one of two QW's. [35, 37, 39] In these cases, the ionized impurity scattering or the roughness scattering is enhanced at resonance when the wavefunctions are extended over two QW's, resulting in a sudden increase of the channel resistance and thus a novel negative transconductance. This scheme, however, cannot be used to turn off the channel conductivity completely as the resistance due to impurity scattering remains finite. The present approach of using the PSL potential, on the contrary, may allow us to cut off the current completely as long as the electric field is weak enough to keep electrons being trapped in the in-plane superlattice potential wells. When a high electric field is applied along the channel, electrons should be heated and start to distribute over a wide range of wavenumbers. In such a cases, only a fraction of electrons in the bottom QW will interact with the periodic potential, resulting in the degradation of switching performance.

5.3   Possible Nano-Fabrication Techniques

In this section, we make a brief review of the current nano-fabrication technology, and discuss possible schemes to realize these novel quantum-effect transistors.

The introduction of 10 nm-scale planar superlattice potential by the periodic modulation of material composition can be realized by a few advanced growth techniques. As shown in Fig. 5.7, the tilted superlattice structure on a mis-oriented substrate, [127] and also lateral superlattices consisting of coupled edge quantum wires on the edge surface of multi QW structures [134] would be suitable methods to fabricate these device

structures. [128] The introduction of a PSL potential by short-length gate array is also a feasible method. However, it requires the most advanced lithography: It is quite difficult to form such a small structure with a scale of ~ 10 nm.

5.4 Summary

In this chapter, we have calculated the energy dispersion of electrons in coupled quantum well (QW) structures where an in-plane periodic potential is introduced in one of the wells. It is found that the resonant coupling of two QW's occurs at a certain wavenumber and results in the gate-controlled modulation of the miniband structure. The novel use of this scheme to modulate the channel conductance is also revealed.
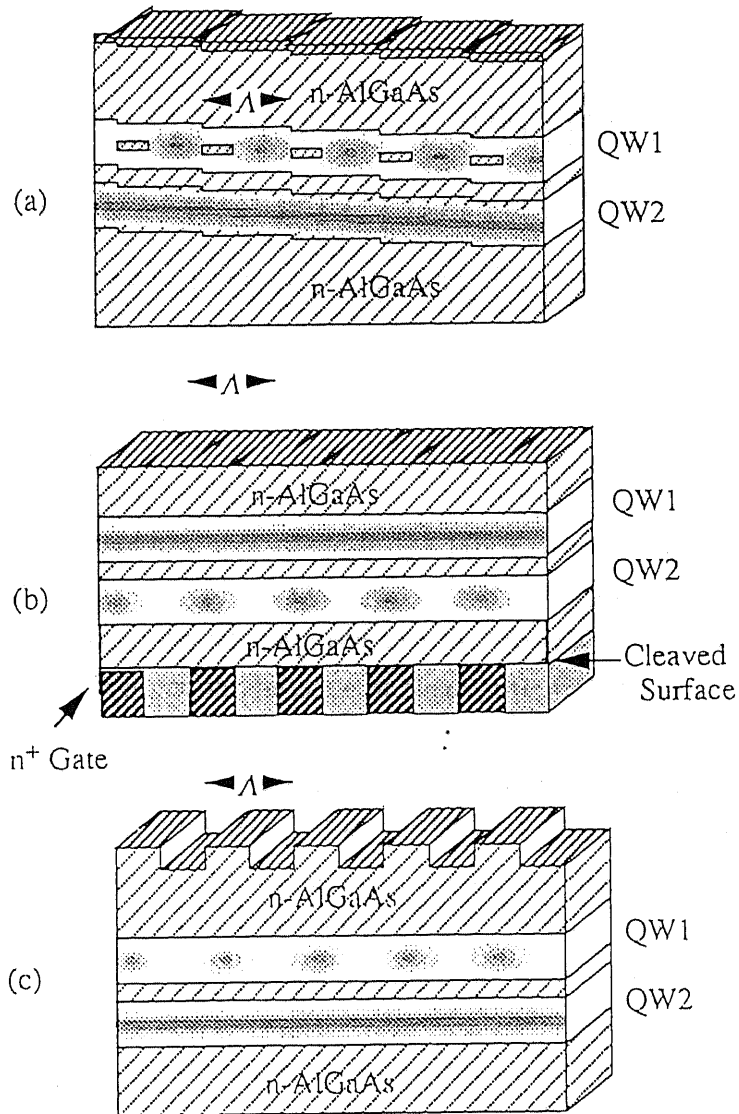
Figure 5.7: Schematic illustrations of possible structures. (a) Lateral superlattice grown on a mis-oriented substrate, (b) using an edge surface of a multiple quantum wells, and (c) lithography + etching process.

Chapter 6

Electron Transport in Multiple Quantum Wires Prepared by in-situ Cleavage and Overgrowth

6.1   Introduction

Recently, remarkable progress has been made in the fabrication of semiconductor nanostructures and also in the studies of physics in one- (1D) or zero- (0D) dimensional electron systems. In particular, great interest has been directed to the electron transport in 1D conductors or 1D - 0D - 1D junctions because of their potentials for future device applications. [15]

To reveal unique features of one-dimensional (1D) electron systems experimentally, one needs to form high quality quantum wires (QWI's) in which electrons are laterally confined to the width of about ~10nm, and are accommodated in a small number of subbands. Earlier, it was suggested that such narrow QWI structures with atomically controlled lateral confinement potential can be prepared if one uses the edge surface of quantum well (QW) structures as a template for the electron wave guide. [15] In such edge QWI structures, the two-dimensional confinement potential is achieved by combination of compositional modulation and an electrostatic force. The cleaved edge overgrowth (CEO) technique, which was proposed in 1990 [77], is one of promising methods to form such edge QWI structures. As shown in Fig. 6.1, a variety of structures such as planar superlattices (PSL's) are also achievable by a CEO technique. [129]

So far, optical properties of quasi 1D-systems have been extensively studied in T-shaped edge QWI's prepared by the CEO. [130–133] Transport experiments across the in-plane potential have also been made in PSL structures prepared by the CEO in such configurations as Fig. 6.1(c) or (d). [134–136] However, transport properties of electrons along narrow edge QWIs (Fig. 6.1(a)) were not amply studied. It is partly because the
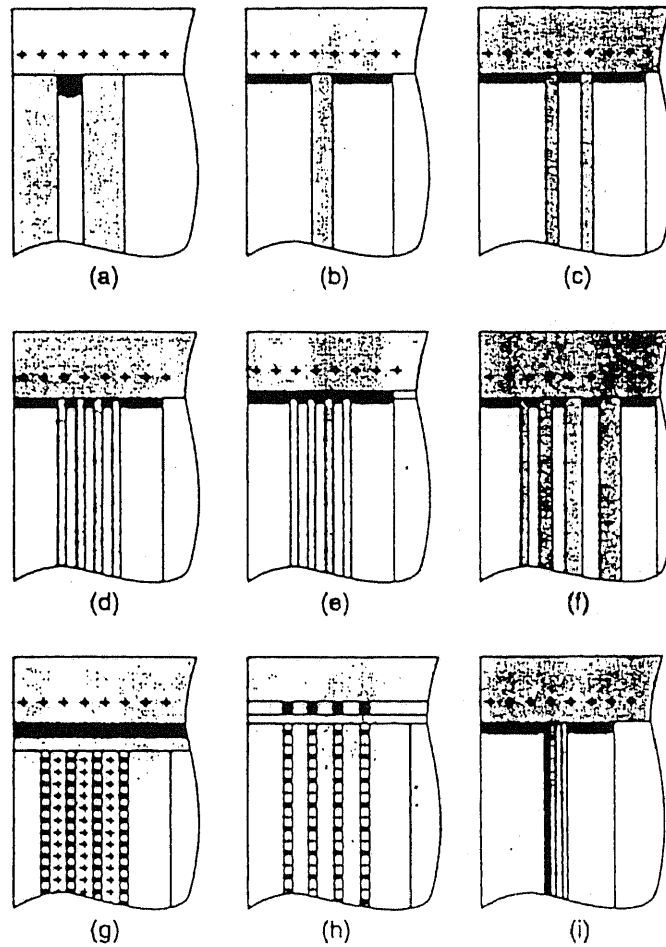
Figure 6.1: Cross-sectional view of several structures achievable by cleaved edge overgrowth. a) 1D wire, b) 2D systems with tunneling barrier, c) 2D-1D-2D double heterojunction tunneling, d) 2D system with 1D superlattice imposed, e) recessed 2D electron system with 1D superlattice imposed, f) 2D system with 1D superlattice of varying thickness, g) 2D system with electrostatically controlled 1D grating, h) modulation doping by recessed 2D multilayers, i) barrier of varying Al concentration in the 2D plane. [129]

formation of reliable ohmic contacts to 1D electrons in these structures was quite difficult. [137] In addition, when the channel width is reduced, qualities of the edge QWIs become quite sensitive to the procedure of CEO process, and critically depend on the condition of the crystal growth. However, we recognize that the CEO is the most effective method to realize high-mobility QWI's and coupled QWI structures with precisely controlled dimensions, which seem difficult to be achieved by the other nano-fabrication techniques.

An attempt to realize such edge QWIs and to investigate the quasi-1D electron transport has been made by Motohisa, who started the CEO in our MBE system and developed it when he was a graduate student. He succeeded in the fabrication of 100 nm-wide multiple edge QWI's, which was confirmed by magnetotransport experiments. [138] In his case, however, the cleavage was carried out not in the growth chamber but in another chamber next to it, i.e. not an *in-situ* processing. Therefore, contamination of the exposed surface was inevitable while the sample was transferred into the growth chamber after the cleavage.

In this context, we were motivated to improve the CEO procedure, and attempted to fabricate edge QWI's for the study of quasi-1D electron properties. Although our destination had been to fabricate coupled QWI structures for the study of interacting 1D electron systems, first we had to establish the CEO technique and to confirm the high quality of the products.

In the next section, we describe our CEO method. Note that as we went on improving the CEO method throughout the present work, the samples characterized in the present work were not fabricated under the best condition shown here. In the third section, we investigate the quasi one dimensional electron transport in multiple edge QWI's. Since it seemed quite difficult to form good ohmic contacts and we had no way to verify the formation of 1D subband in single-mode QWI's, we fabricated and characterized 50nm-wide GaAs / AlGaAs QWI structures. In this sample, at most two subbands are expected to be occupied by electrons when the equivalent sheet electron density is a few times 10^{11} cm^{-2}. In the last section, we discuss the problems in the current CEO processing.

6.2 Fundamentals of Cleaved Edge Overgrowth

6.2.1 MBE growth on GaAs (110) surface

Growth of high-quality (Al,Ga)As on (110) surfaces is most important to fabricate edge QWI structures. It is well-known, however, that facetting occurs when one grows (Al,Ga)As on (110) substrates under standard growth conditions for (001) direction. Several articles
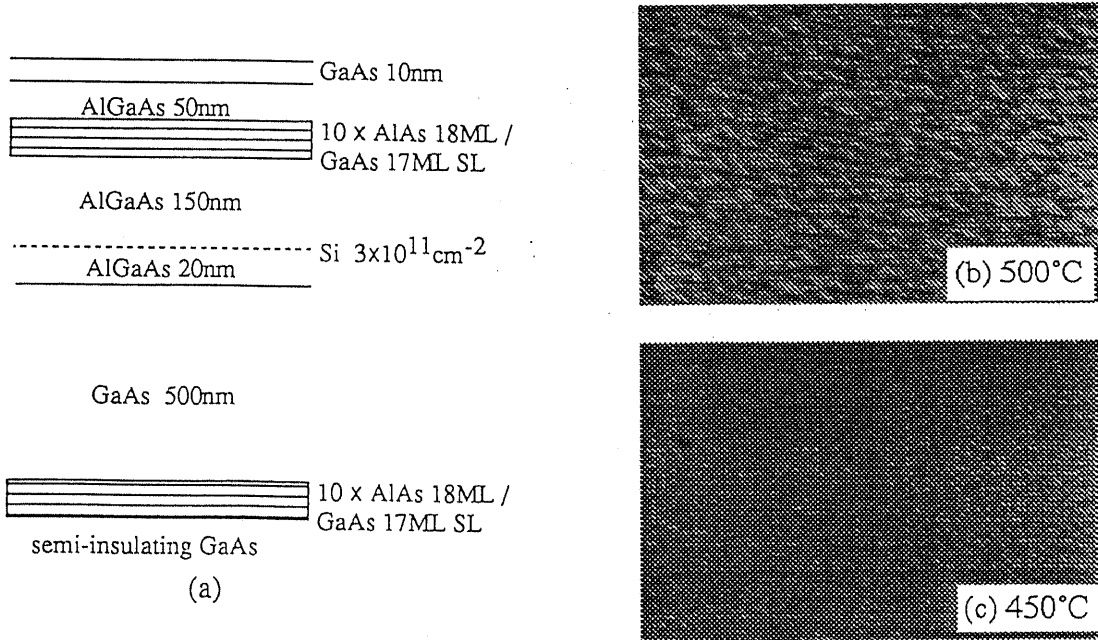
Figure 6.2: (a) The cross-section of a modulation-doped single heterostructure (MDSH) grown on a semi-insulating (110) GaAs substrate. (b) The surface morphology of sample 6A grown at 500 °C, and (c) that of sample 6B grown at 450 °C.

have reported the growth conditions under which smooth and mirror morphology can be achieved on (110) surfaces. [77, 139, 140] We also checked the quality of (Al,Ga)As grown on (110) substrates in order to settle the best condition first of all. We grew GaAs / AlGaAs modulation-doped single heterostructures (MDSH's) on semi-insulating (110) GaAs substrates at 500 °C (sample 6A) and 450°C (6B). In Fig. 6.2(a), the cross section of the sample structure is shown. The growth rate f_{GaAs} was 0.4 μm/h for GaAs, and the As_4 flux F_{As_4} was set to be $2 \sim 4 \times 10^{-5}$ Torr at the position of the substrate, while the background pressure was $1 \sim 2 \times 10^{-7}$ Torr. The V/III ratio was to be $5 \sim 10$, which is smaller than that reported in Ref. [138] by a factor of ~ 2. As compared with the standard condition for the growth in (001) direction, the As_4 pressure is about twice, and the growth rate is a half. (The substrate temperature T_{sub} is normally ~ 600 °C.) Note that T_{sub} was calibrated by assuming the desorption of a thin oxide (Ga_2O_3) film, which is formed on a semi-insulating (110) GaAs substrate during the chemical etching (in H_2SO_4:H_2O_2:H_2O= 8 : 1 : 1 solution for 1 min), to occur at 580°C. Figure 6.2(b) and (c) are the micrographs of the surfaces of sample 6A and 6B, respectively. For sample 6A, which was grown at 500 °C, facet structures are clearly seen. On the other hand, the surface morphology of sample 6B is smooth and mirror.

Next, we studied transport properties of these MDSH structures by a Van-der-Pow
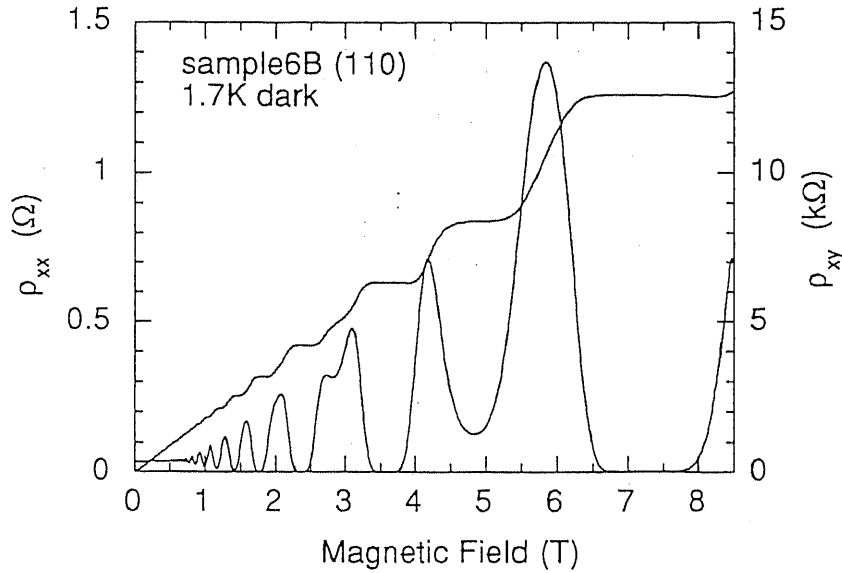
Figure 6.3: Four-probe magnetoresistance ρ_{xx} and Hall resistance ρ_{xy} of a two-dimensional electron gas in sample 6B.

method. The grown wafers were cleaved into 3×3 mm² rhomboid pieces. Ohmic contacts were formed by alloying InSn at four corners. The electron density and the mobility for sample 6B were found to be 3.5×10^{11} cm⁻² and $350,000$ cm²/Vs at 1.7K, respectively, while sample 6A shows no-conduction. In Fig. 6.3, we plot the magnetoresistance ρ_{xx} and the Hall resistance ρ_{xy} for sample 6B as functions of magnetic fields B. These transport measurements reveal the quality of sample 6B to be as high as those reported elsewhere. [77, 140] Following these results, we settled the condition for the overgrowth on the (110) cleaved surfaces as $T_{sub} = 450$ °C, $f_{GaAs} = 0.4$ μm/h, and $F_{As_4} = 2 \sim 4 \times 10^{-5}$ Torr.

Note that although the growth-condition dependence of (110) surface morphology is quite reproducible, the transport properties of 2DEG's in MDSH's depend primarily on the condition of the MBE system. These two samples were grown when the MBE system was maintained in the best condition.

6.2.2 Procedure of In-Situ Cleaved Edge Overgrowth

In Fig. 6.4, the CEO procedure is schematically shown. [77] We first grew a MQW structure used as a waveguide for edge QWI's on (001) semi-insulating GaAs substrate (350 μm-thick) under the standard condition. Details on the first growth sequence are described in the next section. After the first growth, the wafer was taken out of the MBE system

and cleaved into 5mm×11mm rectangular pieces. Each piece was mechanically thinned to the thickness of ~100 μm, followed by the backface etching in H_3PO_4:H_2O_2:H_2O = 1 : 1 : 8 solution for 5min (Fig. 6.4(a)). Then small scratches were made at edges of the piece on both sides, where the cleavage was to be made. Then the sample was soldered by indium vertically on a special molybdenum substrate holder (Fig. 6.4(b)) with a piece of (110)-oriented GaAs substrate simultaneously soldered on the flat plate in order to calibrate the growth temperature by checking the desorption of the thin oxide film. The height of the L-angle from the front of the plate was 5 mm. The sample was brought back to the MBE system, and heated up to 580 °C. During the heating process, the sample was set at the growth position in order to monitor the RHEED pattern. Just before the cleavage, the substrate temperature was lowered down to 500 °C, taking the difference (~ 50 °C) between the temperatures at the plate and the head of the L-angle into account. We opened the gate valve between the growth chamber and another chamber next to it, and introduced the transfer arm into the growth chamber. By rotating the manipulator which holds the sample, we hit the standing wafer with the head of transfer arm to cleave it (Fig. 6.4(c)). The subsequent overgrowth on the exposed (110) edge surface of QW's started within 15 seconds after the cleavage. Figure 6.5 shows micrographs of the typical cleaved surfaces of the substrate, on which about 15 μm-thick GaAs / AlGaAs MQW was already grown. The cleaved edge surfaces of the 100 μm-thick substrate were not always flat like Fig. 6.5(a): most of them were terraced, as shown in Fig. 6.5(b). It was often the case, however, that the surface of the cleaved edge at the epitaxial layer was almost flat even when that of the substrate was heavily terraced. In Figs. 6.5(a) and (b), one can distinguish the epitaxial layer region from the substrate without any chemical processing. The reason is unclear, but we speculate that the difference of the material composition is reflected on the geometry of the cleaved edges.

In order to check the quality of the epitaxial layer grown on the cleaved (110) surfaces, we grew the same MDSH structure as Fig. 6.2(a) on a thinned semi-insulating GaAs substrate (labeled as sample 6C) under the optimized growth condition. We characterized it by measuring the two-terminal magnetoresistance at 1.5 K. Figure 6.6 shows the data of the two-terminal magnetoresistance R at 1.5 K, which contain both features of ρ_{xx} and ρ_{xy}. Pronounced plateaus appear in R vs B in higher B region, and R closely matches the quantized value $h/\nu e^2$ at $\nu < 4$, which suggests that ρ_{xx} including the series ohmic resistance is vanishingly small. Shubnikov-de-Haas oscillation is found to start at $B \sim 0.7$ T, suggesting that the electron mobility is as high as a few times $100,000$ cm^2/Vs.
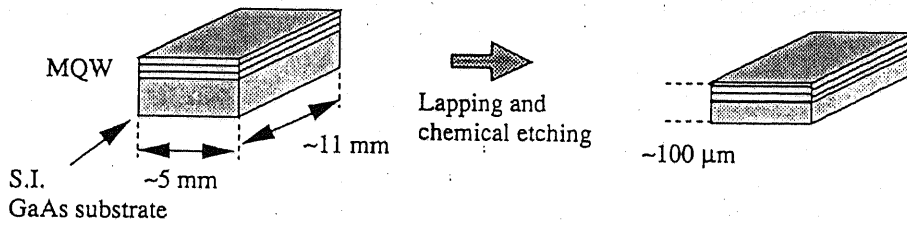
(a) Preparation of a substrate for CEO after the 1st growth of MQW structure
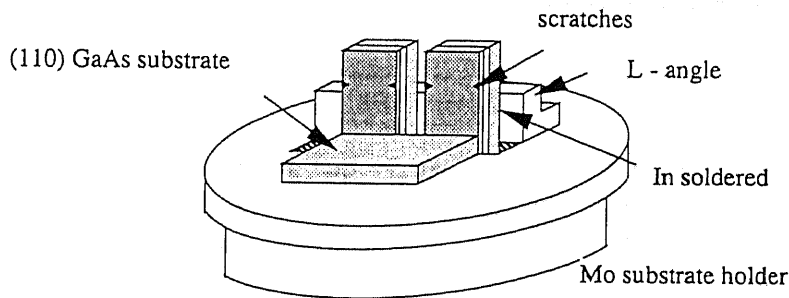
(b) Mounting the MQW sample with reference (110) substrate
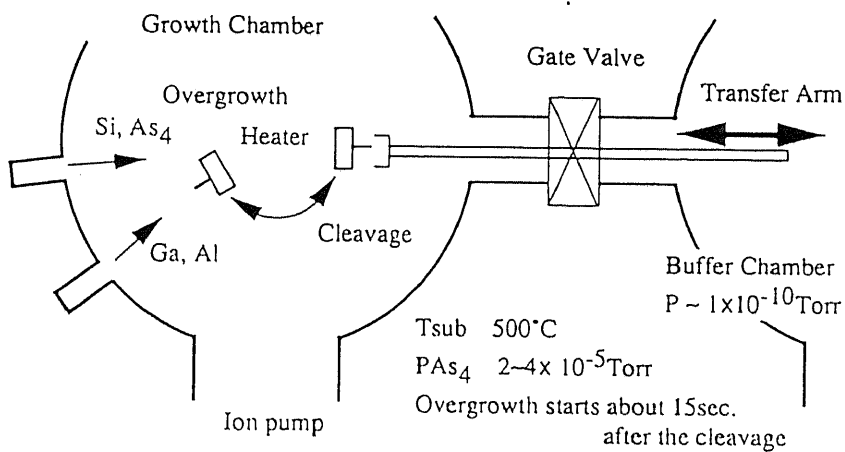
(c) *In-situ* Cleavage using a transfer rod

Figure 6.4: Illustrations of the sample preparation and the CEO procedure

(a)   (b)
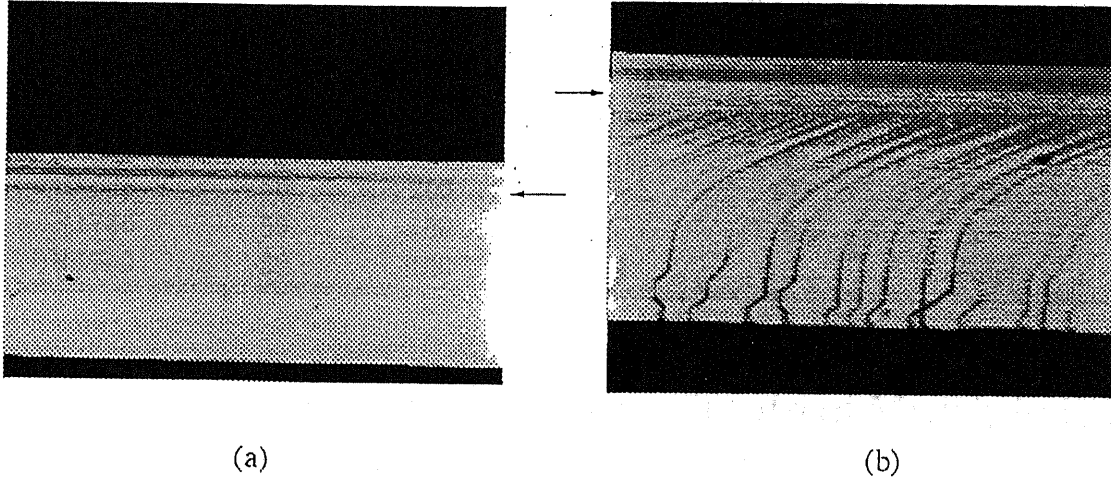
Figure 6.5: Micrographs of the top views of the (a) flat and (b) terraced cleaved edge surfaces. On the top of the substrate in (001) direction (indicated by arrows), 15 μm-thick GaAs / AlGaAs MQW was grown.
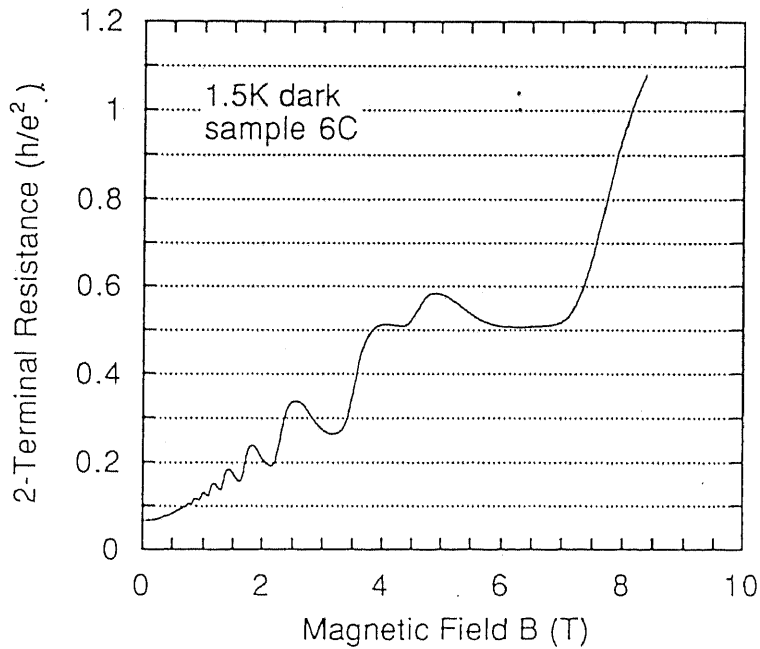

Figure 6.6: 2-terminal magnetoresistance of two dimensional electron gas in a MDSH structure (sample 6C) grown on a cleaved (110) surface.

Table 6.1: The structural parameters of the first-growth MQW's. Symbols:○: features of one-dimension (1D) were observed. △: no 1D feature was observed. ×: no conduction

Sample ID	GaAs QW width (nm)	periods	AlGaAs barrier thickness (nm)	total (μm)	magnetotransport characterization
R1569	10 μm	1		15	×
R1581	50	200	5	20	○ (6D)
R1736	50	100	5	15	△
R1740	20	100	10	15	△ (6E)

6.3 Magnetoresistance Measurements of Multiple Edge Quantum Wires

In a series of the present CEO experiments, we attempted to fabricate a few kinds of edge QWI structures as listed in Table 6.1. A very thick GaAs (R1569) was grown in order to check the formation of 2DEG at the heterointerface between the bulk GaAs and overgrown (n-)AlGaAs. [77] Using these wafers, we carried out the CEO and fabricated a number of edge QWI samples. However, we accomplished the characterization of the transport properties only for a few samples. Although most of the overgrown samples showed electrical conductivity at room temperature, they became insulating when they were cooled to $\sim$ 4.2 K. We speculate that in these samples the current is blocked by the poor conductivity of ohmic contacts, by the depletion of electrons in QWI's, or by defects formed during the first growth of thick GaAs / AlGaAs structures.

In this section, we demonstrate and analyze the magnetoresistance oscillation observed in 50 nm-wide multiple edge QWI's. This sample, which is denoted by sample 6D, showed good conduction at low temperature in dark.

6.3.1 Sample Structure and Experimental Setup

Figure 6.7 shows the schematic illustration and the cross-sectional scanning electron micrograph of the sample 6D. First, a MQW structure sandwiched by superlattice barriers was grown on (001) semi-insulating GaAs substrate by standard MBE. In the first growth, we used indium-soldering-free molybdenum substrate holder. It consists of a 100 nm GaAs buffer layer, a 3 μm-thick superlattice barrier of 3 nm GaAs / 22 nm $Al_{0.27}Ga_{0.73}As$, 200 periods of 50 nm GaAs / 5 nm $Al_{0.27}Ga_{0.73}As$ multiple quantum wells, a 5 μm-thick superlattice barrier of 3 nm GaAs / 22 nm $Al_{0.27}Ga_{0.73}As$, and lastly a 20 nm-thick GaAs cap layer. We made rough estimation of the energy spectrum in this superlattice and found
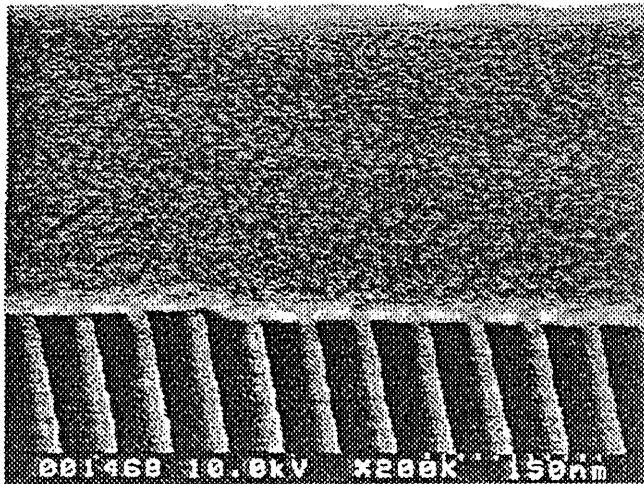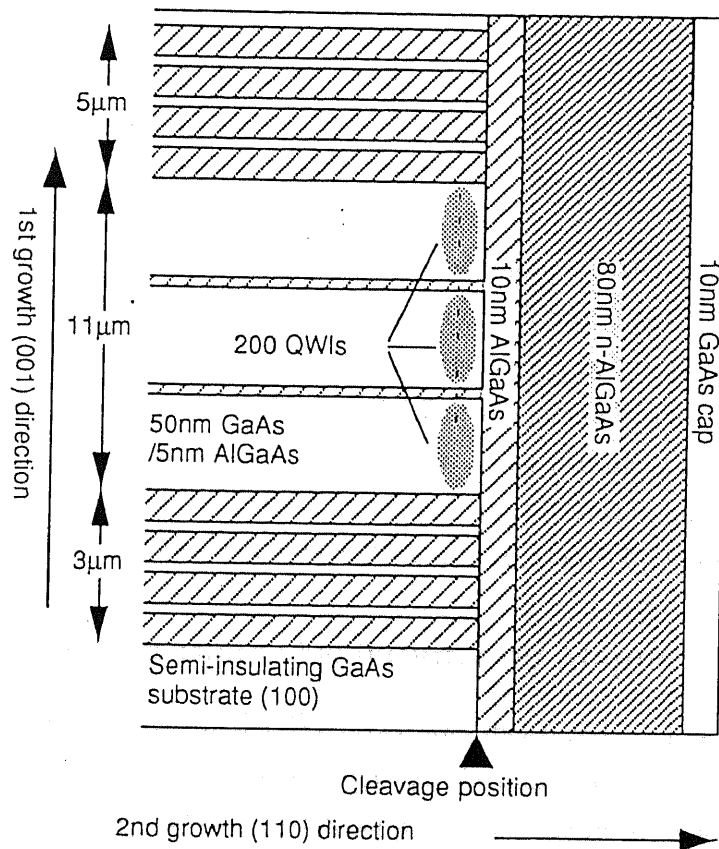
Figure 6.7: Cross sectional view of and edge quantum wire structure, and its scanning electron micrograph. (Taken from another overgrown sample on the same waveguide wafer.

that tunneling of electrons in the lowest two subbands between neighboring two QWs is negligible. (The computed miniband width is less than 0.01 meV.) The number of QWs (or edge QWIs) was chosen to be 200 in order to make the ohmic contacts to be formed easily and surely. This parallel wire structure has the total width of 10 μm (50 nm$\times$200) and reduces the resistance even when the spacing between the ohmic contacts is as long as $\sim$ 100μm.

The sequence of the overgrowth is a 10 nm of undoped AlGaAs spacer layer, an 80 nm-thick Si-doped (2×10^{18} cm^{-3}) n-AlGaAs, and a 10 nm GaAs cap layer.

On the overgrown surface, ohmic contacts were formed by alloying InSn soldered with an even spacing of typically 100$\sim$150μm, yielding 6-7 of multiple quantum wire arrays connected in series along the edge of the sample. The sample was sandwiched by two pieces of GaAs substrate as it stands, and fixed on a ceramic chiptray with graphite paste. Each ohmic contact was wired with 25 μm-ϕ gold wire by hand.

6.3.2   Shubnikov-de-Haas Oscillation and Magnetic Depopulation

The resistance of the two-terminal QWI array was measured by low frequency ac lock-in technique. Since the resistance was unexpectedly high and of the order of $\sim$MΩ, we kept the voltage across the quantum wires to be low and almost constant ($\sim$1 mV), and measured the voltage drop across a 10 kΩ resistor connected in series. No difference in the data was observed when the applying voltage was further reduced. Magnetic fields are applied perpendicularly to the (110) edge surface where the multiple quantum wire array is formed.

Figure 6.8 shows the 2-terminal resistance measured at various temperature T as functions of the magnetic field B. Note that the amplitudes of oscillations are quite large even for a very small field $B < 1$ T, indicating the high quality of the sample. These experimental results are quite reproducible for this sample as long as we follow the same cooling process. At lower temperature, a large oscillation with four resistance peaks is clearly seen for the magnetic field $B < 8$ T. As B exceeds 8T, the resistance shows a rapid increase without any structure (Fig. 6.9). All of the resistance peaks become clear and sharp with decreasing T even $T < 1$ K. These indicate that the observed magnetoresistance comes from the multiple quantum wires, not from the series ohmic contact.

The inverse of B at which the resistance minima appear can be plotted as a functions of the subband index as shown in Fig. 6.10. From this kind of plot, we can readily extract various information, such as the electron density and the lateral size of the confining potential. [141] However, we continue to discuss a few peculiar points in the observed
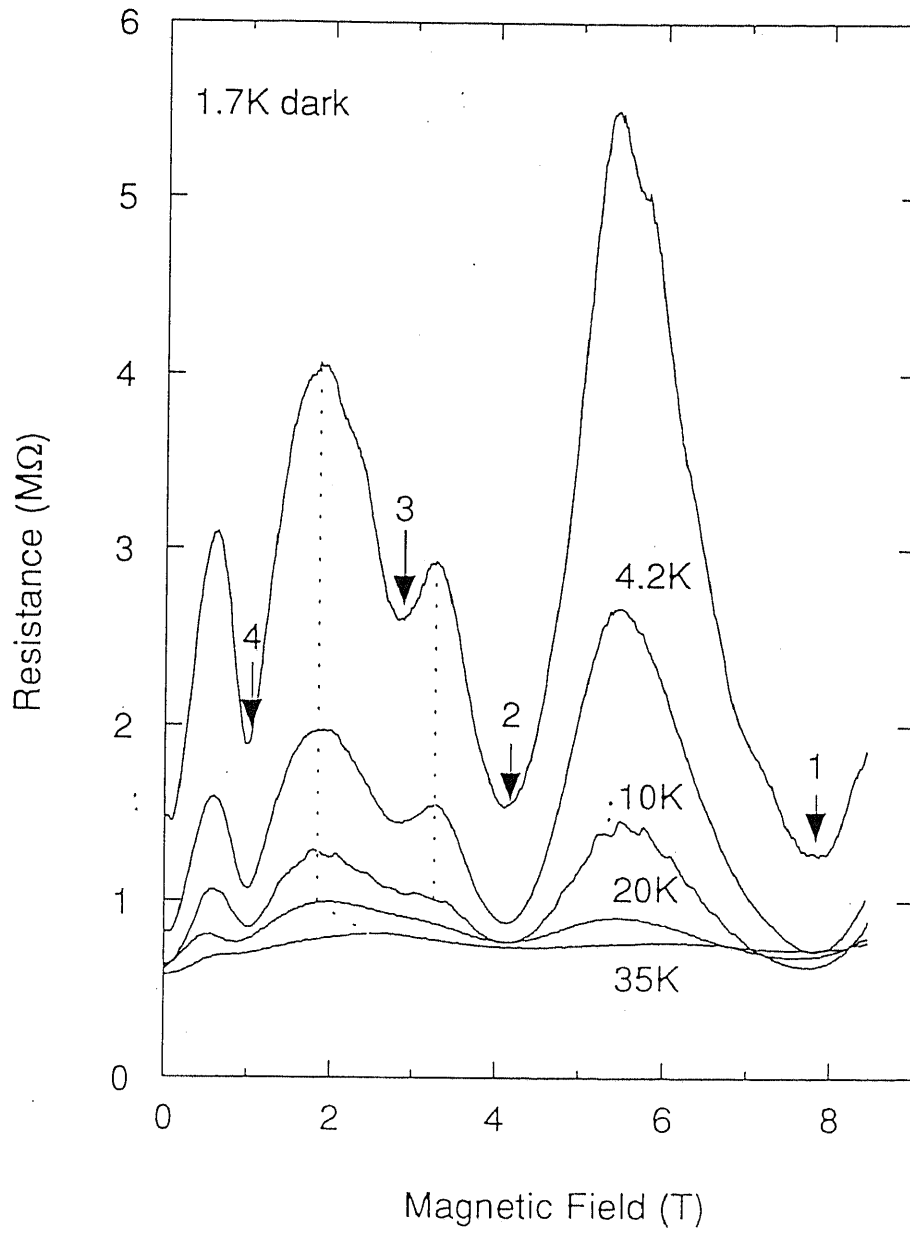
Figure 6.8: The two-terminal magnetoresistances of the 50 nm-wide edge quantum wires (sample 6D) measured at various temperatures $1.7 < T < 35$ K as functions of a magnetic field B.

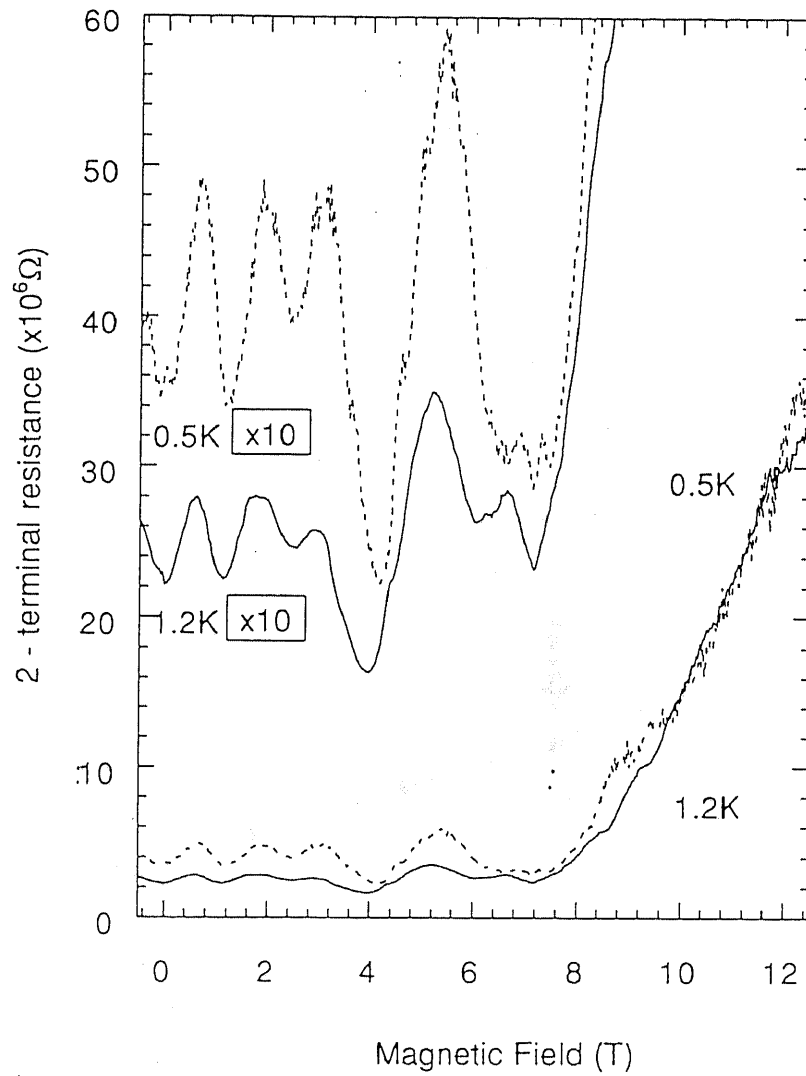Figure 6.9: The two-terminal magnetoresistances of the 50 nm-wide edge quantum wires (sample 6D) measured at 1.2 K (solid line) and 0.5 K (dotted line) as functions of a magnetic field B.
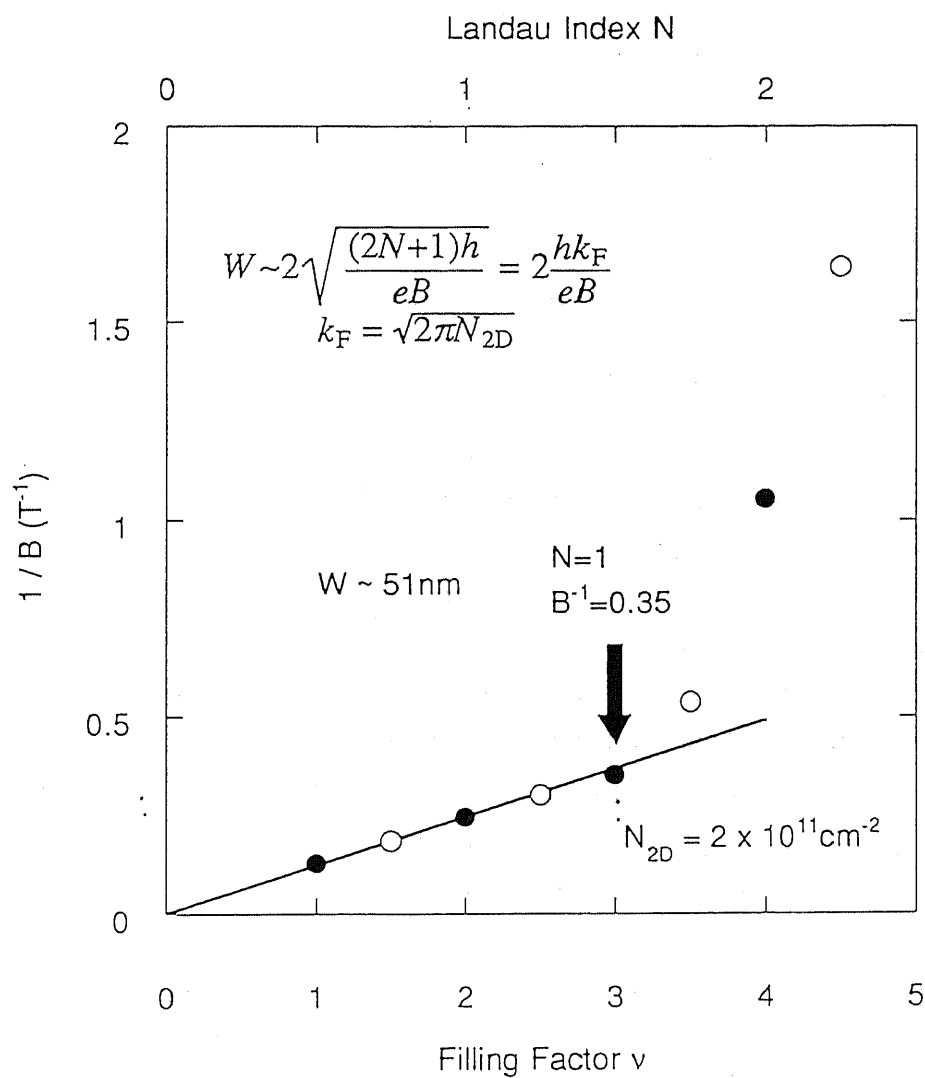
Figure 6.10: The inverse of the magnetic field B at which the magnetoresistance reaches its minimum (solid circles) and maximum (open circles) plotted as a function of the filling factor ν except the last peak at $B = 0.6$ T.

magnetoresistance oscillation.

One notices in Figs. 6.8 and 6.9 peculiar features which are different from those seen in a usual 2D or even in a 1D electron system before. Usually, the amplitudes of magnetoresistance oscillations increase with the magnetic field. In the present case, however, the third resistance peak which appears at 3.2 T is somehow smaller than the other three. In addition, the temperature dependence of the third peak is significantly different from the other three. When T is increased from 1.7 K to 20 K, only the third resistance peak is completely washed out while the others still remain visible. A remarkable change is seen when T is increased to 35 K, where the second- and the third resistance peaks join together. Hence, we have to label a subband index to each resistance peak or valley carefully.

For the present 50 nm-wide quantum wire, as described before, it is expected that the Fermi level lies between the second and the third subband. Hence, the number of resistance peaks in magnetic depopulation spectra can not exceed two. This prediction contradicts clearly with our experiment. One plausible explanation for the observed results is that each Landau subband is split into a pair of spin-resolved subbands and that each resistance peak except for that at the lowest field around 0.6 T originates from the magnetic depopulation effect of a spin-split subband. Following this model, the second- and the third resistance peaks are tentatively ascribed to the depopulation of the subband with the same Landau index but with different spin polarization.

Based on this assumption, we plot the inverse of B at which the magnetoresistance reaches its minimum as a function of the filling factor ν (see Fig. 6.8). As shown in Fig. 6.10, the relation between ν and B^{-1} is linear in the region of high magnetic field $B^{-1} < 0.35$ T^{-1} ($\nu < 3$). At a low field, where $\nu = 4$, B^{-1} becomes much higher than that of a linear relation. This deviation indicates the formation of a hybrid state of one-dimensional subbands and magnetic levels, which convinces the effect of the lateral confinement potential.

From the slope of ν vs B^{-1} in the limit of high B, we can determine the equivalent two dimensional electron density $N_{2D} (= eB\nu/2\pi\hbar)$ and found to be 2.0×10^{11} cm^{-2}, where $\hbar$ is the reduced Plank constant and e the elementary charge, respectively. In order to estimate the wire width W, we use a semi-classical approximation: when the diameter of the cyclotron orbit $2l_c = 2\sqrt{\hbar(2N+1)/eB}$ is smaller than W, the motion of electron is similar to that in a 2D system. At $\nu=3$, where ν-B^{-1} starts to depart from the linear relation, $2l_c$ is calculated to be 51 nm using $N=1$ and $B^{-1}=0.35$ T^{-1}. Note that we distinguish the Landau index N from the filling factor ν. This simple estimation agrees well with the geometrical width (50 nm) of the quantum wires, which is also convinced
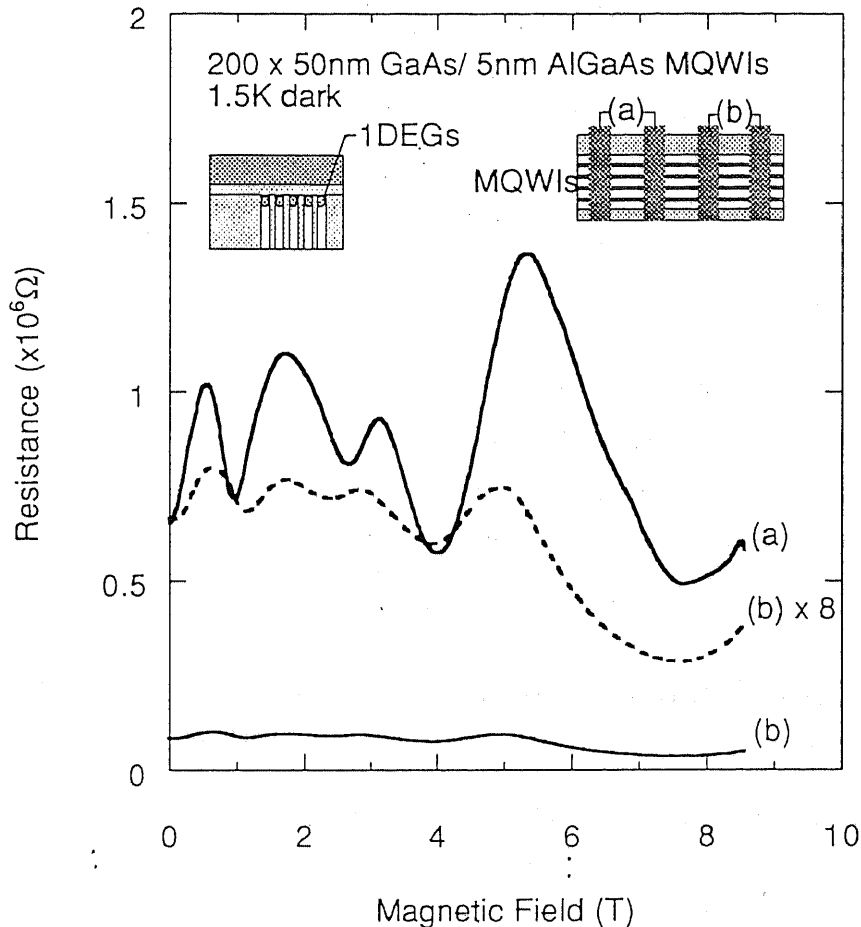
Figure 6.11: Two-terminal magnetoresistances of two edge quantum wire array formed on the sample 6D.

by the cross-sectional scanning electron micrograph.

We also characterized all the other quantum wires which were formed in series on the same cleavage plane, and show the data in Fig. 6.11. We found that their magnetoresistances show their peaks and valleys at almost the same fields B, while the oscillation amplitudes are quite different from each other. This indicates that the electron density or other properties of the quantum wire are quite uniform and unchanged within the 5 mm-long edge of the sample. We found also that at a given temperature, the zero-field resistances of these wires vary from sample to sample by a factor of $\sim$30 at maximum (40 k$\Omega \sim$ 1.5 MΩ at 1.7 K), though their length is almost the same. We speculate that such a large variation of zero field resistance is caused by the differences of the number of conducting wires and / or the transmission coefficient of each quantum wire. Hence, it is

difficult to estimate the electron mobility directly.

Now, let us discuss the low-field magnetoresistance and the origin of a distinct resistance peak at ∼0.6T. Since the number of populated subbands can not exceed two, this particular peak can not be ascribed to the depopulation of a 1D subband. One may speculate that this low field peak originate from such mechanisms as the universal conductance fluctuation (UCF)and / or the boundary scattering. [142]. However, neither seems to fit with our experiment. The boundary of our wires is defined by heterointerfaces of a multiple quantum well structures prepared by the first growth. Hence, the boundary should be quite smooth with its roughness being 1 ML (0.28 nm). In addition, the onset of such roughness scattering should appear at higher magnetic fields, since the cyclotron diameter of the lowest Landau level $2l_c$ is 70 nm at 0.6 T and does not fit exactly with the geometrical wire width. The contribution of UCF should be also small as the number of lateral modes in our wires is reduced to two. Similarly, one should note that a usual negative magnetoresistance coming from the destruction of weak-localization is not seen in our wires. This may be linked with the novel resistance peak at 0.6 T.

6.3.3 Temperature Dependence of Two-Terminal Resistance of Edge Quantum Wires

Note also in Fig. 6.8, that the zero-field resistance shows a strong temperature dependence. In Fig. 6.12, we plot the zero-field resistance R of three QWIs (normalized by each value at 1.7K) as functions of temperature T. It is clear that the resistance R increases drastically as T is lowered below 10 K, in contrast to a 2D system, where both R and the mobility μ converge to constant values. This means that either the resistance of quantum wires or that of ohmic contacts increases for $T < 10$ K. We argue for the following reasons that this unique temperature dependence of resistance originates mainly from the wire resistance rather than from the contact resistance. Firstly, one should note that the reduction of temperature has resulted in not only the increase of zero field resistance $R(B = 0)$ but also the enhancement of oscillatory magnetoresistance, as mentioned earlier. Such a feature is difficult to be ascribed to the series contact resistance, which normally depends very little or monotonically on magnetic fields. Furthermore, we point out that the observed T vs R relation in Fig. 6.12 can be well expressed in the form of $R \propto T^{-\gamma}$, as shown by solid lines. In fact, Ogata and Fukuyama have theoretically shown that $R \propto T^{-\gamma}$ type dependence is expected to appear in QWI system when electron-electron interaction becomes important[74]. To clarify the origin of this unique temperature dependence, however, a further work is certainly needed. For example, thermal activations of localized electronic states in quantum wires may reduce the wire resistance at high temperatures,
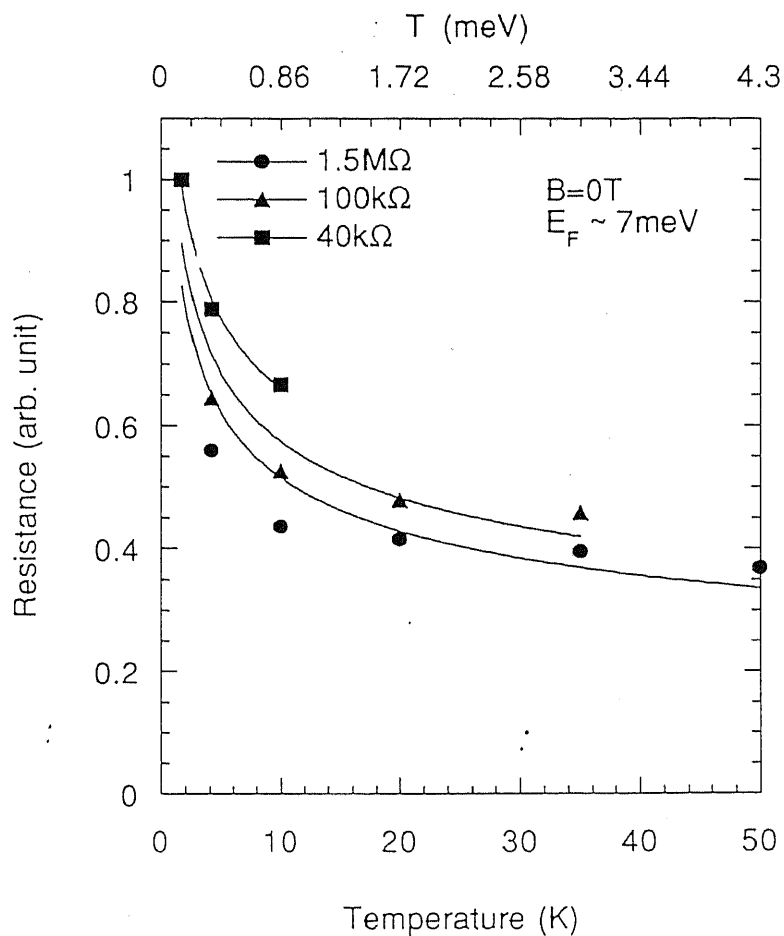
Figure 6.12: The normalized resistances of three quantum wires (a), (b), and (c) yielded on the sample 6D at zero magnetic field are plotted as functions of the temperature. Solid symbols indicate the experimental data, and the solid lines are curve fittings in the form of $\propto T'^{-\gamma}$.

and also may increase the number of conducting wires. We plan to investigate the wire resistance as a function of wire length and also prepare samples with better ohmic contacts by employing a novel scheme described in Ref. [137].

6.3.4 Discussions

Finally, we examine possible contributions of conducting paths other than the wire channel. For example, a sheet of two dimensional electron gas may be formed at the heterointerface between the overgrown AlGaAs layer and the cleaved plane of the 100 μm-thick semi-insulating GaAs substrate, if the concentration of compensating impurities in the GaAs substrate is low. We can rule out this possibility for this sample since all the transport data observed in our experiment are totally different from properties of 2D electrons. However, once the sample was illuminated with a light-emitting diode (LED), the resistance was drastically reduced and unexpectedly the Shubnikov-de-Haas oscillation became that of a normal 2DEG. [143] The magnetoresistance of the sample 6D measured after illumination with a LED is shown in Fig. 6.13. The reason of this crossover from 1D to 2D is still not clear. [143] On this issue, we made further experiments to check the contribution of the parallel conduction at the heterointerface between semi-insulating substrate and the overgrown AlGaAs, which is shown in the next section.

The parallel conduction through the overgrown n-AlGaAs layer should be negligible, since electrons in those doped layers are either trapped or strongly scattered by impurities and can not give rise to a very large magneto-oscillations. Lastly, if 5nm of AlGaAs barriers in the multi-QW structures have macroscopic holes or defects which effectively increase the well width, the cyclotron motion of electrons over the region of 100nm may be allowed and can give rise to more peaks in magnetoresistances. However, such large conducting holes which break 5nm-thick AlGaAs are not very realistic.

6.4 Results of Experiments on 20 nm-wide Multiple Edge Quantum Wires

Finally, we note the experimental results on 20 nm-wide multiple edge QWI's also fabricated by the present cleaved-edge overgrowth technique.

The sequence of the first growth (R1740, see Table 6.1) was as follows: a 10 nm GaAs, 10 periods of 10 monolayer (ML) AlAs / 10 ML GaAs superlattice buffer, 200 periods of 22 nm AlGaAs / 3 nm GaAs superlattice barrier, 250 periods of 20 nm GaAs / 10 nm AlGaAs MQW wave-guide, and 300 periods of 22 nm AlGaAs / 3 nm GaAs superlattice barrier. Thus the total thickness of the channel region amounts to 5 μm (= 250 $\times$ 20 nm). As
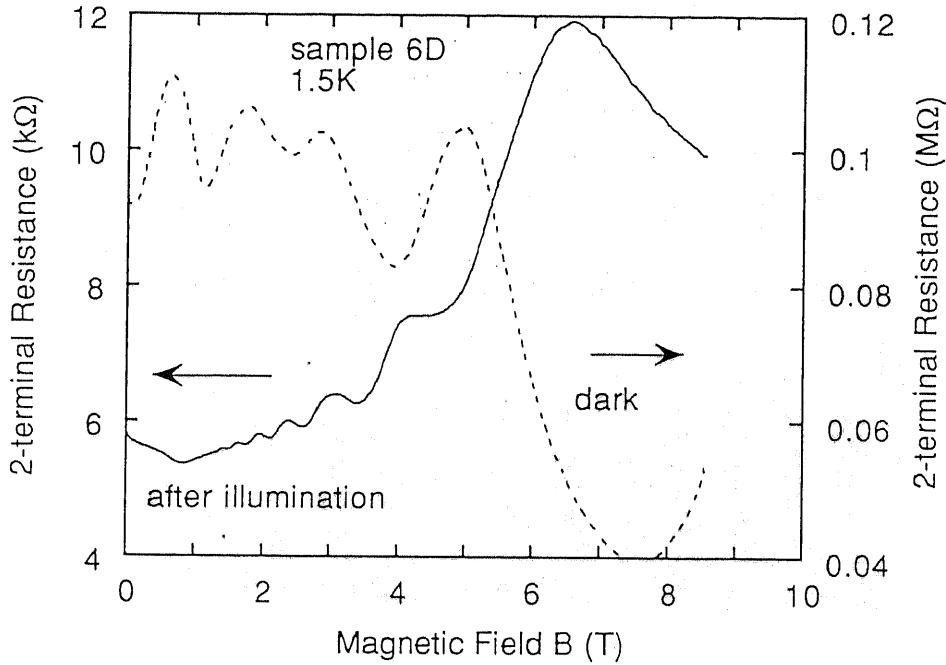
Figure 6.13: The two-terminal magnetoresistances of sample 6D in dark (dotted line) and after illumination with a light emitting diode (solid line).

shown in Fig. 6.14, the formation of the QWI structure was confirmed by scanning electron microscopy. When the same structure as the sample 6D (a 10 nm undoped $Al_{0.3}Ga_{0.7}As$, an 80 nm n-$Al_{0.3}Ga_{0.7}As$, and a 10 nm undoped GaAs) was overgrown on this MQW, however, no sample was conductive at low temperature. Therefore, we speculated that any electron could not accumulate at the heterointerface because the spacer layer was too thick. Taking the increase of the quantized energy levels by the lateral confinement potential into account, we next grew modulation-doping structure with a thinner (5 nm) undoped AlGaAs spacer. In this case, all the samples were conductive even in dark at low temperature, but their magnetoresistance oscillation turned out to be 2D-like.

In order to check the path of the current, we formed ohmic contacts on both sides of the edges, yielding four multiple QWI's as shown in Fig. 6.15: two of five ohmic contacts were formed on the MQW side, and the other three were on the substrate. Since the alloyed InSn was soldered by hand, the ohmic contacts on MQW side should touch the substrate region to some extent. In Fig. 6.16, the measured magnetoresistance was plotted as functions of magnetic fields B. One should note that the magnetoresistances (indicated by closed triangles in Fig. 6.16) between the ohmic contacts formed on the substrate side were smaller than that of the MQW side (displayed by closed circles), showing Shubnikov-

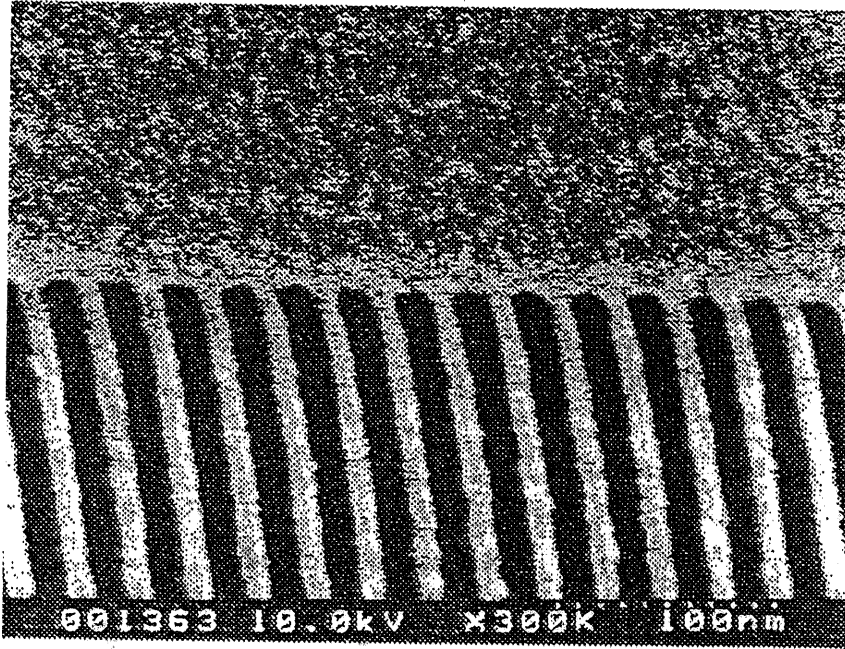Figure 6.14: Scanning electron micrograph of the cross-section of 20 nm-wide multiple edge quantum wires.
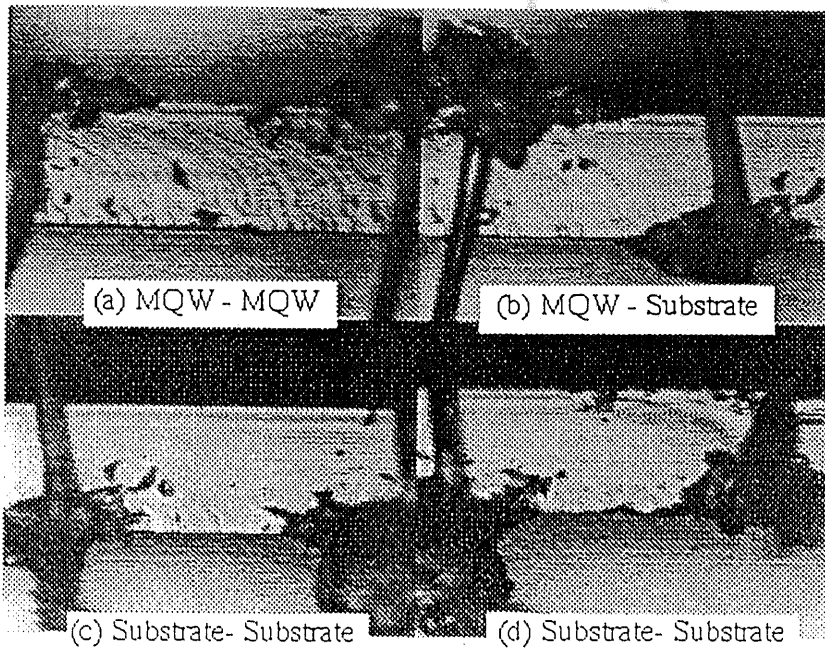
Figure 6.15: Top views of the arrangement of ohmic contacts for sample 6E. Two of five ohmic contacts were formed on the MQW, while the rests were not contacting to it.
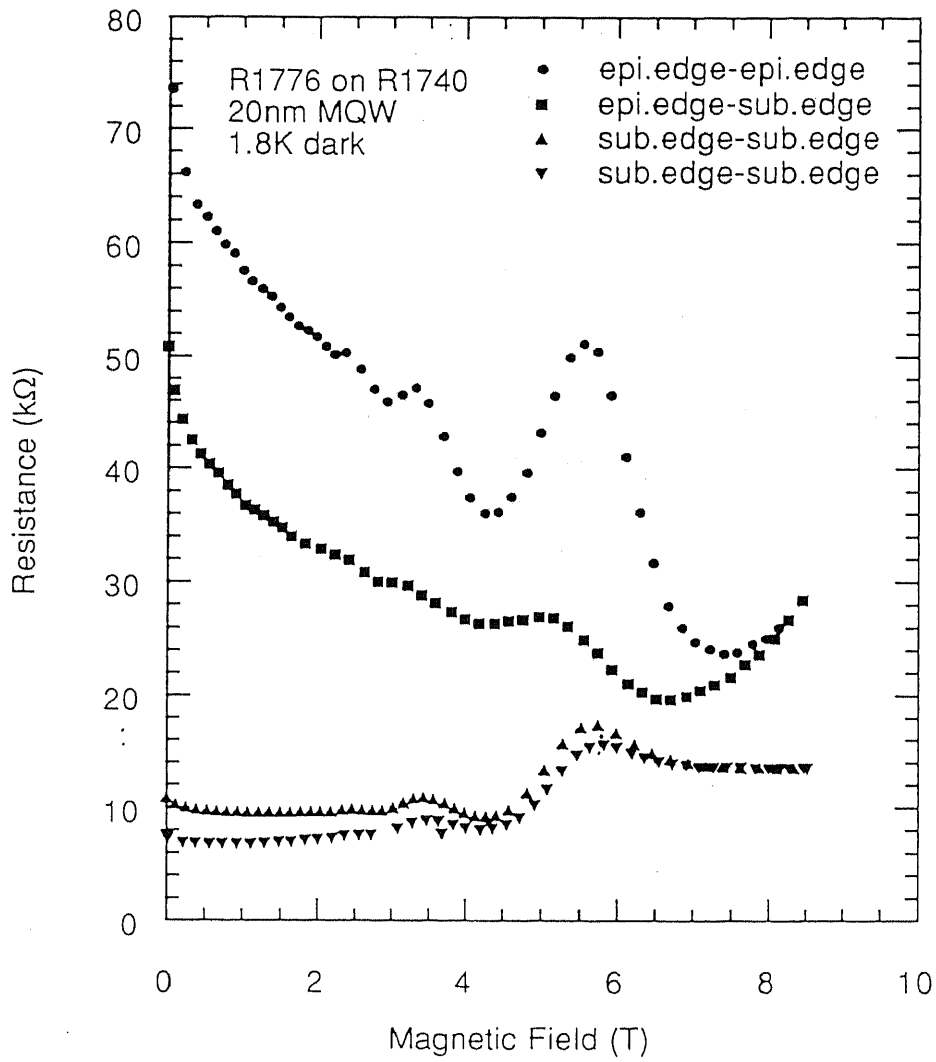
Figure 6.16: Two-terminal magnetoresistances for sample 6E at 1.8K, dark, are plotted as function of a magnetic field.

de-Haas oscillation as $B > 3$ T. From these results, we must admit that electrons can accumulate at the heterointerface of the cleaved surface on semi-insulating GaAs substrate and overgrown AlGaAs when the spacer layer thickness is thin enough. In order to eliminate the contribution of this parallel conduction, one should remove the overgrown n-AlGaAs on the substrate. Thus the processing such as photolithography on the overgrown edge surfaces seems necessary for the studies of electron transport in these configurations.

6.5 Summary

In this chapter, I reported the fabrication of a 50 nm-wide GaAs / AlGaAs edge quantum wire by *in-situ* cleavage and overgrowth technique, and demonstrated a clear magnetoresistance oscillation. Features of the oscillation are interpreted as evidence for the formation of 1D subbands and as indications for the presence of additional subband splitting. In the present work, however, a crucial problem remains unsolved: Parallel conduction, which was observed when the spacer layer between the cleaved surface of the semi-insulating substrate and the overgrown n-AlGaAs is thin as well as when the sample was illuminated with a light-emitting diode at lower temperatures.

Chapter 7

Conclusions

In this thesis, we have systematically studied the electron transport in double quantum well (DQW) and quantum wire (QWI) structures to clarify the unique properties of these low-dimensional electron systems as well as to explore possible applications of such quantum mechanical effects as resonant tunneling to future electronic devices.

In the present work, we devised novel DQW structures in which ionized impurities were intentionally introduced in one of two QW's in order to make large difference between the intrinsic mobilities of them, and grew them by molecular beam epitaxy (MBE). Field effect transistor (FET) structures were fabricated using these wafers, where gigantic negative transconductance and mobility-modulation operation can be achieved by the gate-controlled resonant coupling of electron wave functions.

In Chapter 2, we investigated the features of resonant coupling in those DQW structures. A theoretical model for magnetoresistance in multi-subband systems was presented and compared with the results of magnetotransport experiments. For a heavily-doped DQW, it was found from non-vanishing magnetoresistance at resonance that the disorder of the potential exceeding the tunnel coupling energy should lead to a breakdown of uniform resonant coupling.

In Chapter 3, effects of an in-plane magnetic field on the resonant coupling in the DQW's have been investigated. It was demonstrated that a magnetic field applied parallel to the DQW plane causes mixing of the symmetric and antisymmetric states and reduces them to an isolated state localized in each QW, resulting in quenching of a resonantly-enhanced resistance peak. We also observed anisotropic dependence of the in-plane magnetoresistance on the mutual directions between the channel and the magnetic field. A simple calculation based on a single-particle wave functions has given a qualitative explanation for the observations.

In Chapter 4, the quantized Hall effect in weakly-coupled DQW structures has been investigated by using a novel Hall bar geometry in which each of ohmic electrodes can be

controlled whether it probes both the top and the bottom 2DEG's (in "parallel" mode) or only the bottom one (with the top 2DEG in "floating" situation) by a selective depletion technique. It is emphasized that the resonant tunneling between weakly-coupled two 2DEG's is substantially suppressed under the conditions where the Fermi energy lies in the localized state for the probed bottom 2DEG. Complicated behaviors were also observed in the magnetoresistance or the Hall resistance for the "floating" case, but remain unsolved.

In Chapter 5, we proposed a novel double quantum well field effect transistor, in which a periodic potential is introduced in one of two QW's, and analyzed the electronic properties in such double-layered planar superlattices (PSL's). We carried out numerical calculations for the conduction-band structures and demonstrated the gate-controllability of the effective mass of electrons as a promising scheme to realize a switching device based on a quantum mechanical effect.

In Chapter 6, our progress in the fabrication of QWI structures by cleaved edge overgrowth (CEO) is described from the technical point of view. Successful growth of high-quality GaAs / AlGaAs heterostructures on a (110) substrate has been achieved by improving the growth conditions in MBE. 50 nm-wide edge quantum wires (EQWI's) were fabricated by CEO on a cleaved surfaces of multiple quantum wells (MQW's), which are utilized as a waveguide along the edge. We characterized their magnetotransport properties and observed a prominent magnetoresistance oscillation, which exhibit clearly the features of the formation of 1D subbands confined within each 50 nm-wide QW.

Finally, we hope the present study will contribute to the comprehensive understandings of the electron transport in coupled low dimensional electron system and underlying physics.

Bibliography

[1] L. Esaki and R. Tsu, *IBM J. Res. Dev.* **14**, 61 (1970)

[2] See for a review: H. Sakaki, in *III-V Semiconductor Materials and Devices*, edited by R. J. Malik, (Elsevier Science Publishers, 1989)

[3] L. L. Chang, L. Esaki, And R. Tsu, *Appl. Phys. Lett* **24**, 593 (1974)

[4] T. C. L. G. Sollner, W. D. Goodhue, P. E. Tannenwald, C. D. Parker, and D. D. Peck, *Appl. Phys. Lett.* **43**, 588 (1983)

[5] S. Luryi, *Appl. Phys. Lett.* **47**, 490 (1985)

[6] S. Luryi, *Superlattice and Microstructures* **5**, 375 (1989)

[7] K. Maezawa, and T. Mizutani, *Jpn. J. Appl. Phys.* **32**, L42 (1993);

[8] T. C. L. G. Sollner, E. R. Brown, W. D. Goodhue, and H. Q. Le, *Appl. Phys. Lett.* **50**, 332 (1986)

[9] J. P. Ziel, R. Dingle, R. C. Miller, W. Wiegmann, and W. A. Nordland, Jr., *Appl. Phys. Lett.* **26**, 463 (1975); W. T. Tsang, *Appl. Phys. Lett.* **39**, 786 (1981)

[10] R. Dingle, H. L. Störmer, A. C. Gossard, and W. Wiegmann, *Appl. Phys. Lett* **33**, 665 (1978)

[11] T. Mimura, S. Hiyamizu, T. Fujii, and K. Nanbu, *Jpn. J. Appl. Phys.* **19**, L225 (1980)

[12] K. von Klitzing, G. Dorda, and M. Pepper, *Phys. Rev. Lett* **45**, 494 (1980)

[13] D. C. Tsui, H. L. Stormer, and A. C. Gossard, *Phys. Rev. Lett.* **48**, 1559 (1982)

[14] See for a review: *The Quantum Hall Effect*, edited by R. E. Prange, and S. M. Girvin (Springer, New York, 1987)

[15] H. Sakaki, *Jpn. J. Appl. Phys.* **19**, L735 (1980)

[16] Y. Arakawa, and H. Sakaki, *Appl. Phys. Lett.* **40**, 939 (1982)

[17] H. Sakaki, K. Wagatsuma, J. Hamasaki, and S. Saito, *Thin Solid Films* **36**, 497 (1976)

[18] H. Sakaki, *Jpn. J. Appl. Phys.* **28**, L314 (1989)

[19] A. Lorke, and P. M. Petroff, *Solid-State Electron.* **37**, 0000 (1994); B. Etienne, F. Laruelle, J. Bloch, L. Sfaxi, and F. Lelarge, *J. Cryst. Growth* **150**, 336 (1995);

[20] See for a review: H. van Houten, C. W. J. Beenakker, and A. A. M. Staring, in *Single Charging Tunneling*, edited by H. Garbert, J. M. Martinis, and M. H. Devoret (Plenum, New York, 1991)

[21] L. J. Geerlings, V. F. Anderegg, P. A. M. Holweg, J. E. Mooij, H. Pothier, D. Esteve, C. Urbina, and M. H. Devoret *Phys. Rev. Lett.* **64**, 2691 (1990)

[22] K. Yano, T. Ishii, T. Hashimoto, T. Kobayashi, F. Murai, and K. Seki, *IEEE Electron Devices* **41**, 1628 (1994)

[23] L. L. Chang, H. Sakaki, C. A. Chang, and L. Esaki, *Phys. Rev. Lett.* **20**, 1489 (1977)

[24] E. E. Mendez, F. Agullo-Ruea, and J. M. Hong, *Phys. Rev. Lett.* **60** 2426

[25] K. Leo, J. Shah, T. C. Damen, A. Schulze, T. Meiner, S. Schmitt-Rink, P. Thomas, E. O. Göbel, S. L. Chuang, M. S. C. Luo, W. Schäfer, K. Köhler, and P. Ganser, *IEEE Quantum Electron.* **28**, 2498 (1992)

[26] L. Y. Liu, E. E. Mendez, and H. Meiner, *Appl. Phys. Lett.* **60**, 2971 (1992)

[27] S. Datta, M. R. Melloch, S. Bandyopadhyay, and M. S. Lundstrom, *Appl. Phys. Lett.* **48**, 487 (1986)

[28] M. Okuda, K. Fujii, and A. Shimizu, *Appl. Phys. Lett.* **57**, 2231 (1990)

[29] A. Shimizu, *Phys. Rev. A* **43**, 3819 (1991)

[30] M. Okuda, K. Fujii, S. Miyazawa, and A. Shimizu, *Phys. Rev. B* **00**, 0000 (0000)

[31] H. Sakaki, *Jpn. J. Appl. Phys.* **21**, L381 (1982)

[32] H. Hirakawa, H. Sakaki, and J. Yoshino, *Phys. Rev. Lett.* **54**, 1279 (1985)

[33] A. Kurobe, J. E. Frost, D. A. Ritchie, G. A. C. Jones, and M. Pepper, *Appl. Phys. Lett.* **60**, 3268 (1992)

[34] B. Vinter and A. Tardella, *Appl. Phys. Lett.* **87**, 410 (1987)

[35] A. Palevski, F. Beltram, F. Cappaso, L. Pfeiffer, and K. W. West, *Phys. Rev. Lett.* **65**, 1929 (1990)

[36] Y. Ohno, M. Tsuchiya, and H. Sakaki, *Electron. Lett.* **29**, 375 (1993)

[37] Y. Ohno, M. Tsuchiya, and H. Sakaki, *Appl. Phys. Lett.* **62**, 1952 (1993)

[38] M. Tsuchiya, T. Noda, H. Kano, and H. Sakaki, *Inst. Phys. Conf. Ser.* **112**, 339 (1990)

[39] A. Palevski, S. Luryi, P. L. Gammel, F. Capasso, L. N. Pfeiffer, and K. W. West, *Superlattices and Microstructures* **11**, 269 (1992)

[40] J. Smolinar, W. Demmerle, G. Berthold, E. Gronik, and G. Weimann, *Phys. Rev. Lett.* **63**, 2116 (1989)

[41] P. M. Solomon, P. J. Price, D. J. Frank, and D. C. La Tulipe, *Phys. Rev. Lett* **63**, 2508 (1989); B. Laikhtman, and P. M. Solomon, *Phys. Rev. B* **41**, 9921 (1990)

[42] J. P. Eisenstein, L. N. Pfeiffer, and K. W. West, *Appl. Phys. Lett.* **57**, 2324 (1990)

[43] J. P. Eisenstein, L. N. Pfeiffer, and K. W. West, *Appl. Phys. Lett.* **58**, 1497 (1991)

[44] J. P. Eisenstein, T. J. Gramila, L. N. Pfeiffer, and K. W. West, *Phys. Rev. B* **44**, 6511 (1991)

[45] J. P. Eisenstein, L. N. Pfeiffer, and K. W. West, *Phys. Rev. Lett.* **68**, 674 (1992)

[46] J. P. Eisenstein, L. N. Pfeiffer, and K. W. West, *Phys. Rev. Lett.* **69**, 3804 (1992)

[47] J. P. Eisenstein, L. N. Pfeiffer, and K. W. West, *Surf. Sci.* **305**, 393 (1994)

[48] Y. Katayama, D. C. Tsui, H. C. Manoharan, and M. Shayegan, Preprint (unpublished)

[49] K. M. Brown, N. Turner, J. T. Nicholls, E. H. Linfield, M. Pepper, D. A. Ritchie, and G. A. C. Jones, *Phys. Rev. B* **50**, 15 465 (1994)

[50] E. E. Mendez, L. Esaki, and W. I. Wang, *Phys. Rev. B* **33**, 2893 (1986)

[51] T. Chakraborty, and P. Pietiläinen, *Phys. Rev. Lett* **59**, 2784 (1987)

[52] D. Yoshioka, A. H. MacDonald, and S. M. Girvin, *Phys. Rev. B* **39**, 1932 (1989)

[53] H. A. Fertig, *Phys. Rev. B* **40**, 1087 (1989)

[54] L. Brey, *Phys. Rev. Lett.* **65**, 903 (1990)

[55] S. He, X. C. Xie, S. Das Sarma, and F. C. Zhang, *Phys. Rev. B* **43**, 9339 (1991)

[56] S. He, S. Das Sarma, and X. C. Xie, *Phys. Rev. B* **47**, 4349 (1993)

[57] J. P. Eisenstein, G. S. Boebinger, L. N. Pfeiffer, K. W. West, and S. He, *Phys. Rev. Lett.* **68**, 1383 (1992)

[58] Y. W.Suen, L. W. Engel, M. B. Santos, M. Shaygan, and D. C. Tsui, *Phys. Rev. Lett* **68**, 1379 (1992)

[59] M. A. Paalanen, R. L. Willet, P. B. Littlewood, R. R. Ruel, K. W. West, L. N. Pfeiffer, and D. J. Bishop, *Phys. Rev. B* **45**, 11 342 (1992)

[60] G. S. Boebinger, H. W. Jiang, L. N. Pfeiffer, and K. W. West, *Phys. Rev. Lett.* **64**, 1793 (1990)

[61] G. S. Boebinger, L. N. Pfeiffer, and K. W. West, *Phys. Rev. B* **45**, 11 391 (1992)

[62] A. H. MacDonald, P. M. Platzman, and G. S. Boebinger, *Phys. Rev. Lett.* **65**, 775 (1990)

[63] S. Q. Murphy, J. P. Eisenstein, G. S. Boebinger, L. N. Pfeiffer, and K. W. West, *Phys. Rev. Lett* **72**, 728 (1994)

[64] G. S. Boebinger, S. Q. Murphy, J. P. Eisenstein, L. N. Pfeiffer, K. W. West, and S. He, *Surf. Sci.* **305**, 8 (1994)

[65] R. C. Ashoori, J. A. Lebens, N. P. Bigelow, and R. H. Silsbee, *Phys. Rev. Lett.* **64**, 681 (1990)

[66] Z. F. Ezawa, and A. Iwazaki, *Phys. Rev. Lett* **70**, 3119 (1993); Z. F. Ezawa, and A. Iwazaki, *Int. J. Mod. Phys.* **preprint**

[67] T. Kimura, K. Kuroki, and H. Aoki, *Phys. Rev. B* **49**, 16 852 (1994)

[68] R. Landauer, *IBM J. Res. Dev.* **1**, 223 (1957); R. Landauer, *Philos. Mag.* **21**, 863 (1970); M. Büttiker, *Phys. Rev. Lett.* **57**, 1761 (1986)

[69] B. J. van Wees, H. van Houten, C. W. J. Beenakker, J. G. Williamson, L. P. Kouwenhoven, D. van der Marel, and C. T. Foxon, *Phys. Rev. Lett.* **60**, 848 (1988)

[70] B. J. van Wees, L. P. Kouwenhoven, H. van Houten, C. W. J. Beenakker, J. E. Mooij, C. T. Foxon, and J. J. Harris *Phys. Rev. B* **38**, 3625 (1988)

[71] J. Sólyom, *Adv. Phys.* **28**, 201 (1979); F. D. M. Haldane, *J. Phys. C* **14**, 2585 (1981)

[72] C. L. Kane, and M. P. A. Fisher, *Phys. Rev. Lett.* **68**, 1220 (1992)

[73] H. Fukuyama, H. Kohno, and R. Shirasaki, *J. Phys. Soc. Jpn.* **62**, 1109 (1993)

[74] M. Ogata, and H. Fukuyama, *Phys. Rev. Lett* **73**, 468 (1994)

[75] see for a review: *Transport Phenomena in Mesoscopic Systems*, edited by H. Fukuyama, and T. Ando (Springer Verlag, Berlin, 1991)

[76] T. Honda, S. Tarucha, T. Saku, and Y. Tokura, *Jpn. J. Appl. Phys.* **preprint**; S. Tarucha, T. Honda, and T. Saku, in *the Proceedings of ICPS-22*, 1807, Vancouver, Canada, August 1994

[77] L. N. Pfeiffer, K. W. West, H. L. Stormer, J. P. Eisenstein, K. W. Baldwin, D. Gershoni, and J. Spector, *Appl. Phys. Lett.* **56**, 1697 (1990)

[78] Y. Nakamura, M. Tsuchiya, J. Motohisa, H. Noge, S. Koshiba, and H. Sakaki, *Solid State Electron.* **37**, 571 (1994)

[79] T. Shitara, M. Tornow, A. Kurtenbach, D. Weiss, K. Eberl, and K. v. Klitzing, *Appl. Phys. Lett.* **66**, 2385 (1995)

[80] A. Yariv, C. Lndsey, and U. Sivan, *J. Appl. Phys.* **58**, 3669 (1985)

[81] K. Inoue, H. Sakaki, J. Yoshino, and T. Hotta, *J. Appl. Phys.* **58**, 4277 (1985)

[82] P. P. Ruden, and Z. Wu, *Appl. Phys. Lett.* **59**, 2165 (1991)

[83] Y. Katayama, D. C. Tsui, H. C. Manoharan, and M. Shayegan, *Surf. Sci.* **305**, 405 (1994)

[84] T. Ando, A. B. Fowler, and F. Stern, *Rev. Mod. Phys.* **54**, 437 (1982)

[85] E. D. Siggia, and P. C. Kwok, *Phys. Rev. B* **2**, 1024 (1970); S. Mori, and T. Ando, *Phys. Rev. B* **19**, 6433 (1979)

[86] W. A. Beck, J. R. Anderson, *J. Appl. Phys.* **62**, 541 (1987)

[87] M. J. Kane, N. Apsley, D. A. Anderson, L. L. Taylor, and T. Kerr, *J. Phys. C: Solid State Phys.* **18**, 5629 (1985)

[88] H. H. Wieder, *Appl. Phys. Lett.* **25**, 206 (1974)

[89] S. Hikami, A. I. Larkin, and Y. Nagaoka, *Prog. Theor. Phys.* **63**, 707 (1980)

[90] K. Inoue, H. Sakaki, and J. Yoshino, *Jpn. J. Appl. Phys.* **23**, L767 (1984)

[91] K. Hirakawa, and H. Sakaki, *Phys. Rev. B* **33**, 8291 (1986)

[92] F. T. Vasko, *Phys. Rev. B* **47**, 2410 (1993)

[93] F. T. Vasko, *Pis'ma Zh. Eksp. Teor. Fiz.* **56**, 7 (1992) [*JETP Lett.* **56**, 4 (1992)]

[94] A. Kurobe, I. M. Castleton, E. H. Linfield, M. P. Grimshaw, K. M. Brown, D. A. Ritchie, M. Pepper, and G. A. C. Jones, *Phys. Rev. B* **50**, 8024 (1994)

[95] P. T. Coleridge, R. Stoner, and R. Fletcher, *Phys. Rev. B* **39**, 1120 (1989)

[96] B. R. Snell, K. S. Chan, F. W. Sheard, L. Eaves, G. A. Toombs, D. K. Maude, J. C. Portal, S. J. Bass, P. Claxton, G. Hill, and M. A. Pate, *Phys. Rev. Lett.* **59**, 2806 (1987)

[97] J. A. Lebens, R. H. Silsbee, and S. L. Wright, *Phys. Rev. B* **37** 10 308 (1988)

[98] T. M. Fromhold, M. L. Leadbeater, L. Eaves, T. J. Foster, P. C. Main, and F. W. Sheard, *Surf. Sci* **305**, 0000 (1994)

[99] S. B. Amor, K. P. Martin, J. J. L. Rascol, J. Higgins, A. Torabi, H. M. Harris, and C. J. Summers, *Appl. Phys. Lett.* **53**, 2540 (1988)

[100] L. Eaves, R. K. Hayden, M. L. Leadbeater, D. K. Maude, E. C. Valadares, M. Henini, E. W. Sheard, O. H. Hughes, J. C. Portal, and L. Cury, *Surf. Sci.* **263**, 199 (1992)

[101] G. S. Boebinger, A. Passner, L. N. Pfeiffer, and K. W. West, *Phys. Rev. B* **43**, 12 673 (1991)

[102] J. A. Simmons, S. K. Lyo, J. F. Klem, M. E. Sherwin, and J. R. Wendt, *Phys. Rev. B* **47**, 15 741 (1993)

[103] S. K. Lyo, *Phys. Rev. B* **50**, 4965 (1994)

[104] J. A. Simmons, S. K. Lyo, N. E. Harff, and J. K. Klem, *Phys. Rev. Lett.* **73**, 2256 (1994)

[105] Y. Berk, A. Kamenev, A. Palevski, L. N. Pfeiffer, and K. W. West, *Phys. Rev. B* **50**, 15 420 (1994)

[106] Y. Berk, A. Kamenev, A. Palevski, L. N. Pfeiffer, and K. W. West, *Phys. Rev. B* **51**, 2604 (1995)

[107] A. Kurobe, I. M. Castleton, E. H. Linfield, M. P. Grimshaw, K. M. Brown, D. A. Ritchie, M. Pepper, and G. A. C. Jones, *Phys. Rev. B* **50**, 4889 (1994)

[108] A. Kurobe, I. M. Castleton, E. H. Linfield, M. P. Grimshaw, K. M. Brown, D. A. Ritchie, M. Pepper, and G. A. C. Jones, in *Abstracts of the Meeting of the Physical Society of Japan*, 27a-X-4, Osaka, September 1995 (in Japanese)

[109] Y. Ohno, H. Sakaki, and M. Tsuchiya, *Phys. Rev. B* **49**, 11 492 (1994)

[110] O. Raichev, and F. T. Vasko, private communication

[111] F. T. Vasko, *Phys. Rev. B* **52**, 0000 (1995)

[112] E. H. Linfield, G. A. C. Jones, D. A. Ritchie, and J. H. Thompson, *Semicond. Sci. Technol.* **8**, 415 (1993)

[113] N. K. Patel, E. H. Linfield, K. M. Brown, M. P. Grimshaw, D. A. Ritchie, G. A. C. Jones, and M. Pepper, *Appl. Phys. Lett.* **64**, 3018 (1994)

[114] N. K. Patel, J. H. Burroughes, M. J. Tribble, E. H. Linfield, A. C. Churchill, D. A. Ritchie, and G. A. C. Jones, *Appl. Phys. Lett.* **65**, 851 (1994)

[115] L. N. Pfeiffer, E. F. Schubert, and K. W. West, *Appl. Phys. Lett.* **58**, 2258 (1991)

[116] S. M. Sze, Physics of Semiconductor Devices John Wiley & Sons, Inc., 1981

[117] T. Ohtsuki, B. Kramer, and Y. Ono, *J. Phys. Soc. Jpn.* **62**, 224 (1993)

[118] A. M. Chang, *solid State Commun.* **74**, 871 (1990)

[119] C. W. J. Beenakker, *Phys. Rev. Lett* **64**, 216 (1990)

[120] B. I. Halperin, *Phys. Rev. B* **25**, 2185 (1982)

[121] M. Büttiker, *Phys. Rev. B* **38**, 9375 (1988)

[122] D. B. Chklovskii, B. I. Shklovskii, and L. I. Glazman, *Phys. Rev. B* **46**, 4026 (1992)

[123] R. J. F. van Haren, F. A. P. Blom, and J. H. Wolter, *Phys. Rev. Lett* **74**, 1198 (1995)

[124] R. J. Haug, *Semicond. Sci. Techinol.* **8**, 131 (1993)

[125] S. Komiyama, H. Hirai, M. Ohsawa, Y. Matsuda, S. Sasa, and T. Fujii, *Phys. Rev. B* **45**, 11 085 (1992); N. B. Zhitenev, R. J. Haug, K. v. Klitzing, and K. Eberl, *Phys. Rev. B* **51**, 17 820 (1995)

[126] K. Ismail, D. A. Antoniadis, and H. I. Smith, *Appl. Phys. Lett.* **55**, 589 (1989)

[127] M. Tanaka, and H. Sakaki, *Appl. Phys. Lett* **54**, 1326 (1989); J. Motohisa, M. Tanaka, and H. Sakaki, *Appl. Phys. Lett.* **55**, 1214 (1989)

[128] H. Sakaki, *Surf. Sci.* **267**, 623 (1992)

[129] H. L. Stormer, L. N. Pfeiffer, K. W. West, and K. W. Baldwin, in Nanostructures and Mesoscopic Systems, ed. W. P. Kirk and M. A. Reed, Academic Press inc. 1992

[130] Y. C. Chang, L. L. Chang, and L. Esaki, *Appl. Phys. Lett.* **47**, 1324 (1985)

[131] A. R. Goñi, L. N. Pfeiffer, K. W. West, A. Pinczuk, H. U. Baranger, and H. L. Stormer, *Appl. Phys. Lett.* **61**, 1956 (1992)

[132] W. Wegscheider, L. N. Pfeiffer, M. M. Dignam, A. Pinczuk, K. W. West, S. L. McCall, and R. Hull, *Phys. Rev. Lett* **71**, 4071 (1993)

[133] T. Someya, H. Akiyama, and H. Sakaki, *Appl. Phys. Lett* **66**, 3672 (1995); T. Someya, H. Akiyama, and H. Sakaki, *Phys. Rev. Lett.* **74**, 3664 (1995)

[134] H. L. Stormer, L. N. Pfeiffer, K. W. Baldwin, K. W. West, and J. Spector, *Appl. Phys. Lett* **58**, 726 (1991)

[135] A. Zaslavsky, D. C. Tsui, M. Santos,and M. Shaygan, *Appl. Phsy. Lett.* **58**, 1440 (1991)

[136] M. M. Dignam, R. C. Ashoori, H. L. Stormer, L. N. Pfeiffer, K. W. Baldwin, and K. W. West, *Phys. Rev. B* **49** 2269 (1994)

[137] W. Wegsheider, W. Kang, L. N. Pfeiffer, K. W. West, H. L. Stormer, and K. W. Baldwin, *Solid-State Electron.* **37**, 547 (1994)

[138] J. Motohisa, and H. Sakaki, *Appl. Phys. Lett.* **63**, 1786 (1993)

[139] J. Zhou, Y. Huang, Y. Li, and W. Y. Jia, *J. Cryst. Growth* **81**, 221 (1987)

[140] M. C. Holland, A. H. Kean, and C. R. Stanley, *J. Cryst. Growth* **150**, 455 (1995)

[141] K.-F. Berggren, G. Roos, and H. van Houten, *Phys. Rev. B* **37**, 10 118 (1988)

[142] T. J. Thornton, M. L. Roukes, A. Scherer, and B. P. Van de Garrg, *Phys. Rev. Lett* **63**, 2128 (1989)

[143] J. Motohisa, in *thesis*, University of Tokyo (1993)

Publication List

1. Publication List

1. Y. Ohno, M. Tsuchiya, and H. Sakaki, *"New functional field-effect transistor based on wavefunction modulation in δ-doped double quantum wells"*, Electron. Lett. **29**, 375 (1993)

2. Y. Ohno, M. Tsuchiya, and H. Sakaki, *"Gigantic negative transconductance in a double-quantum well structure via gate-controlled resonant coupling"*, Appl. Phys. Lett. **62**, 1952 (1993)

3. Y. Ohno, M. Tsuchiya, T.Matsusue, T. Noda, and H. Sakaki, *"Non-uniform resonant coupling effect on 2D electron transport in δ-doped double quantum well structures"*, Surf. Sci. **305**, 322 (1994)

4. Y. Ohno, H. Sakaki, and M. Tsuchiya, *"Quenching of resonance-induced resistance in double quantum wells in the presence of in-plane magnetic fields"*, Phys. Rev. B **49**, 11492 (1994)

5. Y. Ohno, Y. Nakamura, M. Foley, T. Someya, T. Noda, and H. Sakaki, *"Magnetoresistance oscillations in 50nm-wide GaAs/AlGaAs multiple edge quantum wires"*, Phys. Rev. B **52**, 11619 (1995)

6. Y. Ohno, and H. Sakaki, *"Gate-controlled modulation of eletronic states and conductance in coupled quantum wells having an in-plane periodic potential"*, to be published in Solid State Electron.

7. Y. Ohno, and H. Sakaki, *"Suppression of resonant tunneling in a coupled quantum well in the quantum Hall regime"*, to be published in Surf. Sci.

8. Y. Ohno, M. Foley, and H. Sakaki, *"Magnetotransport properties of tunnel-coupled two dimensional electron gases"*, to be submitted to Phys. Rev. Lett.

2. Presentations (International)

1. Y. Ohno, M. Tsuchiya, T. Matsusue, T. Noda, and H. Sakaki, *"Non-uniform resonant coupling effect on 2D electron transport in δ-doped double quantum well structures"*, The 10th International Conference on Electronic Properties in Two Dimensional Systems, Newport, RI, June 1993

2. Y. Ohno, M. Tsuchiya, and H. Sakaki, *"A novel quantum effect FET with resonantly modulated transfer characteristics"*, The 51st Annual Device Research Conference, Santa Barbara, CA, June 1993

3. <u>Y. Ohno</u>, Y. Nakamura, M. Foley, T. Someya, T. Noda, and H. Sakaki, *"Observation of large oscillations in magnetoresistances of 50nm-wide GaAs/AlGaAs multiple edge quantum wires"*, The International Workshop on Mesoscopic Physics and Electronics, Tokyo, Japan, March 1995

4. <u>Y. Ohno</u>, and H. Sakaki, *"Gate-controlled modulation of eletronic states and conductance in coupled quantum wells having an in-plane periodic potential"*, The 7th International conference on Modulated Semiconductor Structures, Madrid, Spain, July 1995

5. <u>Y. Ohno</u>, and H. Sakaki, *"Effects of a floating channel on magnetotransport properties of two dimensional electron gases in a resonantly coupled double quantum well structure"*, The 11th International Conference on Electronic Properties in Two Dimensional Systems, Nottingham, UK, August 1995

6. <u>Y. Ohno</u>, M. Foley, and H. Sakaki, *"Magnetotransport of two dimensional electron gases in a novel tunnel-coupled double quantum well system"*, 23rd International Conference on the Physics of Semiconductors, Berlin, Germany, July 1996 (submitted)